Norwegian School of Economics
Bergen, Fall 2022

Climate Risk Assessment for Tramp Shipping Pre-Fixture Calculations

Marie Log Staveland and Sia Benedikte Strømsnes

Supervisor: Gabriel Moises Fuentes Lezcano

Master Thesis, Economics and Business Administration

Major: Business Analytics

NORWEGIAN SCHOOL OF ECONOMICS

Acknowledgements

First and foremost, we would like to express our sincere gratitude to our supervisor, Gabriel Mosises Fuentes, for excellent guidance, constructive feedback, and valuable insights throughout the process of completing this thesis.

We are also grateful to Dataloy for granting us access to their database and providing us with data on the shortest distance of our chosen routes. We would like to thank Copernicus Marine Service for crucial third-party weather data, which greatly contributed to our findings. Additionally, we would like to thank Signal Ocean Group for their assistance in estimating port costs and Clarkson's Shipping Intelligence service for their information on voyages, including data on crucial ports, freight rates, and fuel prices.

We would also like to thank Western Bulk for their noon data, which allowed us to predict fuel consumption. Finally, we would like to express our gratitude to the Norwegian Shipowner's Association for their generous grant for this thesis.

Norwegian School of Economics

Bergen, December 2022

Marie Log Staveland

Sia Benedikte Strømsnes

Abstract

In this thesis, we conduct a climate risk assessment for tramp shipping pre-fixture calculations using business analytics. We analyze the effects weather-related events have on various shipping routes. Data from different sources are used to identify potential risks and evaluate routing options as mitigation strategies. To predict the fuel consumption of the routes, we used machine learning, in which the random forest regression proved to be the best-fitting model. Furthermore, the thesis describes how we used the ray trace algorithm and the haversine formula to connect the weather data to the routes of study. The output was then used to generate weather routing distributions for further analysis of how the weather would affect the decision about which route to choose when seasonal changes occur. Moreover, we used simulation to calculate the Time Charter Equivalent (TCE) for different routes and scenarios. Afterward, the TCE formula was used to calculate the final results. Our findings suggest that shipowners can reduce voyage costs by choosing routes less affected by extreme weather. Therefore, we recommend using machine learning models to predict fuel consumption, consider seasonal variations and their effect on fuel expenditure, and take a stochastic approach to TCE by using distributions. Hence, shipowners will be able to take a data-driven decision when deciding on the best route, in order to increase the likelihood of higher profits.

Keywords – Tramp Shipping, Time Charter Equivalent, Weather Routing, Distributions, Stochastic Approach, Simulation, Machine Learning, Random Forest, Decision-Making

Contents

List of Figures

List of Tables

1 Introduction

The decision to use pre-fixed calculations when acquiring voyage-chartered vessels entails uncertainty, which makes it difficult for shipowners to ensure guaranteed profit for a voyage. One of the most significant sources of this uncertainty is the weather, affecting fuel consumption and, therefore also, the fuel costs (Norlund and Gribkovskaia, 2017). According to Rehmatulla and Smith (2015), fuel costs can account for up to 70 percent of a vessel's voyage cost. Hence, the weather is an essential factor to assess in detail.

When deciding and assessing the best voyage option for a voyage-chartered vessel, the current industry standard compares alternatives with Time Charter Equivalent (TCE) calculations (Hayes, 2021). The TCE contains information about revenue and expenses related to the voyage, divided by the duration of the trip. Thus, TCE constitutes an effective measure for comparison. However, for practical purposes, the TCE calculation of uncertain fuel consumption is based on historical information or buffered through rules of thumb (Ballou et al., 2008). In both cases, the default is to derive a single value based on a deterministic rule. For instance, it is common among practitioners to assume a 10 to 15 percent weather margin for any TCE calculation (Szelangiewicz and Żelazny, 2016; Magnussen, 2017).

Despite the rule of thumb being standard practice, it may fall short when the weather turns out to be worse than expected during the voyage. A competitive advantage may also be lost when the margin overshoots the calculations on seasonally calm weather periods. To overcome this issue, in this thesis, we propose a method to generate a distribution of TCEs and bring a new perspective on how to decide on an efficient voyage based on different scenarios to reduce risk and optimize profit. We have obtained actual climate data from 2006 through 2019, which will be the foundation of our method and derived results. The routes start at the Cape of Good Hope (a geographically suitable rendezvous area) and, from there, sail to different regions based on where the offer of Supramax vessels [1] are likely to be.

Our thesis will provide valuable insight in how to reduce risk by deciding which route

[1] Supramax vessels are a type of cargo ship that are designed to carry dry cargo, such as coal, iron ore, and grain. They are typically between 50,000 and 60,000 deadweight tons and can navigate through shallow waters, and smaller ports (Menon, 2021)

to choose in different scenarios and evaluating TCE based on wind and wave climate variables. Using a machine learning model, we can connect fuel consumption to weather data and create a distribution for fuel consumption. Then, by performing a simulation utilizing the fuel consumption distribution to calculate TCE, we will understand how voyage costs are affected by seasons and climate.

This thesis proposes three contributions. Firstly, a method to generate distributions of TCE with climate information as input. A distribution of TCEs will convey more information than a single TCE value, thus an important tool to assess risk. Secondly, based on climate seasonality, we compare routes for a Supramax vessel trading to crucial ports. Finally, we conduct a business-oriented analysis on the case of a vessel open for cargo at the Cape of Good Hope.

In the next section, we will conduct a literature review of relevant topics related to the weather margin, fuel consumption, voyage costs, and risks. Afterwards, we will present the theoretical framework before we describe our methodology for this thesis. In addition, we will analyze different case studies for three pre-determined routes. The scenarios we will explore are:

1. high fuel price and the corresponding freight rate,
2. average fuel rate and the corresponding freight rate, and
3. low fuel price and the corresponding freight rate.

Furthermore, we will present our results and findings before we finally come to a conclusion and list our recommendations.

2 Literature Review

2.1 Voyage Risks

The shipping industry is not without exceptions regarding risks for the parties involved. Variables with uncertain outcomes largely contribute to fluctuations in the net cash flow of shipowners and charterers (Kavussanos et al., 2021, p. 328). Therefore, although efficiency, profit-maximizing, and cost-minimizing are crucial within the shipping business, they must not be at the expense of avoidable risks, such as weather-related fuel consumption.

Although shipping is considered the most fuel- and cost-efficient means of transportation, there has been an increase in the regulatory pressure for a greener and more sustainable approach to the maritime industry (Stratiotis, 2018). With volatile fuel prices, it is more important than ever to minimize voyage costs without increasing risk (Zis et al., 2020). As the bunker costs can exceed 50 percent of the carrier's charges when the sailing speed and the fuel prices are high, significant economic drivers are in place (Alizadeh and Nomikos, 2009; Rehmatulla and Smith, 2015; Ronen, 2011). However, poor weather can elevate the probability of physical injuries and material damage. Such factors have resulted in two primary objectives when planning a voyage: minimization of fuel consumption and the real risk of the journey while considering time-varying sea and weather (Veneti et al., 2017).

Previous research shows many initiatives in which weather routing has been in focus. Such voyage optimization considers currents and weather forecasts when planning the route while mitigating risks. To avoid weather-related hazards and unnecessary delays, this process, more than ever, integrates voyage planning with safety-, cost-, and emission management. The literature covers many route optimization methods, but the most common are isochrone methods, dynamic programming, calculus, pathfinding algorithms, artificial intelligence, and machine learning (Zis et al., 2020). Several sources claim that weather routing can make up 2 to 5 percent in fuel savings, highlighting the importance of weather assessment in a voyage (Armstrong, 2013; Dtn, 2021). Furthermore, because of economies of scale, a slight reduction in these costs can save millions of dollars (Zis et al., 2020).

2.2 Voyage Costs

Voyage costs include fuel, port fees, and canal fees. However, bunker fuel typically accounts for nearly 75 percent of the total voyage costs, making it the most critical factor to evaluate when trying to minimize the expenses (Rehmatulla and Smith, 2015). Weather can have a significant impact on voyage costs, especially fuel costs. Lindstad et al. (2013) have concluded that varying speed as a function of sea conditions and freight market can save significant costs connected to voyages. They found that the operation's economical speed was considerably lower than the design speed.

2.3 Fuel Consumption

Fuel cost highly depends on weather and the speed of a vessel. The literature states that fuel consumption will also reduce if a ship reduces its speed. Taskar and Andersen (2020) investigated the benefit of speed reduction in different weather conditions and simulated vessels in various weather while operating at different speeds. They found that reducing the speed to save fuel is effective in calm waters. However, Taskar and Andersen (2020) states that lower speeds do not result in lower fuel consumption in cases with added resistance, like weather-related obstacles. Hence, they concluded that fuel consumption in rough weather on the voyage is independent of speed.

Roh (2013) presents another perspective on fuel consumption and how it is affected by the weather. He studied different measures to reduce fuel consumption by finding alternative economical routes for a vessel. In this paper, he derived the minimized fuel consumption by acquiring sea state information. Furthermore, the results state that shipowners should consider longer voyages than the shortest route if the weather dictates that it is more beneficial in the light of cost-minimization. Sea state represents the waves and wind, and Roh (2013) proves that choosing a slightly longer route is more advantageous if the weather is worse on the short distance.

2.4 Weather Margin

As the weather significantly impacts the variable costs of a voyage, it is standard practice to account for this by including a weather margin in the freight rate. Although it has been

common to use 10 to 15 percent for many years, people have researched the possibility of more accurate measures. For example, Nilsson and Nilsson (2021) developed, in their master's thesis, a machine-learning algorithm using Extra Trees to predict fuel consumption. They further used this model to find seasonal variations in fuel consumption. The results also show that the standard deviation for the weather margins was twice as high during the winter compared to the summer, indicating a higher chance of bad weather. Seasonal variations with their model showed seasonal variation in fuel consumption of 6.4 percent for the Supramax vessel on their specified case route (Nilsson and Nilsson, 2021).

In Magnussen's (2017) paper, she used the powering prediction method to investigate the usage of weather margins. She concludes that it would be misleading to use a predetermined percentage as a base on specific routes. For instance, results showed that the path between Georgetown and Cape Town had a weather margin of 19.81 percent. In addition, she found that the Powering Prediction Model could be underestimating the actual margin. This thesis did not include the possibility of extreme weather, which could impact the final result (Magnussen, 2017).

By investigating the sea margin for container ships and bulk carriers during various routes, Szelangiewicz and Żelazny (2016) discovered that the service speed is easier to maintain for container ships when accounting for the weather. Therefore, they calculated the sea margin assuming the expected service speed remained the same for each route. The method depended on vessel type, size, and statistical weather parameters. This method estimated a sea margin of approximately 27.5 percent and 33.8 percent, which is considerably higher than the rule of thumb (Szelangiewicz and Żelazny, 2016).

3 Theory

3.1 Time Charter Equivalent

When using dry cargo vessels, it is standard to use fixed contracts known as charter parties, where two of the most common are the voyage charter and the time charter. A time charter party is a contract where the shipowner lends the ship to a charterer for a period of time. The shipowner gets paid regularly from this agreement, whereas the charterer generates its revenue through freight (Plomaritou and Papadopoulos, 2017, pp. 1-4). However, the operating costs are split between the charterer, who pays for voyage expenses, and the shipowner, who is responsible for the operational costs (Panayides, 2018, pp. 65-66). A voyage charter party states that the shipowner is responsible for all operating and voyage expenses. Negotiating these contracts happens when the vessel is used for one journey from one port to another (Panayides, 2018, p. 66). In our study, we focus on the latter, as a risk assessment for pre-fixture calculations is more relevant in the case of the shipowner's engagement in a voyage charter. The risk of the fuel consumption uncertainty derives into a fuel consumption risk and will nonetheless amount to an essential factor for the owner's cost.

When comparing charter contracts for time charters and voyage charters, it would be possible to calculate the daily hire a vessel will obtain on a voyage trip using the Time Charter Equivalent (Panayides, 2018, p. 204). The TCE formula is, as shown in Equation 3.1, the voyage revenues minus voyage expenses divided by the total voyage duration in days. The voyage expenses are variable and consist of costs related to the canal, bunker, and ports (Hayes, 2021).

$$TCE = \frac{Voyage\ Revenues - Voyage\ Costs}{Roundtrip\ Voyage\ Duration\ in\ Days} \tag{3.1}$$

As stated in *Principles of Chartering* (Panayides, 2018), the voyage costs are variable, and the bunker costs amount to a significant part of these. The total bunker costs depend on the ship's engine consumption, speed, travel distance, and encountered deviations. When calculating the time to get from one port to another, the weather should be taken into account since facing bad weather can reduce speed and change routes (pp. 209-210).

3.2 Simulation in the Shipping Industry

Within the shipping industry, simulation is used to improve strategies and find optimal voyage routes. In addition, it is an efficient tool for making decisions and assessing risk. Furthermore, because simulation enables analysts to compress time and space, problems can easily be solved while still being dynamic (Marklund and Laguna, 2018, pp. 257-259).

A simulation is a tool commonly used by shipping managers to optimize profit. Performing a simulation can result in improved strategy and can for instance, be used to assess how different revenue management methods are performed in different scenarios within shipping (Zurheide and Fischer, 2014). Seeing as the weather is difficult to predict, it is common to use simulations for a stochastic approach. For instance, it can be performed a stochastic discrete simulation to find the safest route for a voyage based on data of wave height (Kosmas and Vlachos, 2012).

A stochastic approach simulates processes accommodating for randomness (Marklund and Laguna, 2018, p. 202). A process has elements of randomness when the input variables contain uncertainties, and performing a simulation could contribute to a more accurate result. Because of this, a stochastic approach repeats this process multiple times, taking into consideration the uncertain input data, generating multiple output values (Marklund and Laguna, 2018, p. 262). In other words, probability distributions are used to generate a new output for each repetition of the process (Softwaresim, 2022).

The probability distributions of the uncertain input variables are often unknown. Simulating the process with an incorrect distribution will lead to a misleading result, even though the system has a correct input. By retrieving samples from the actual data, an empirical distribution may be the best fit according to Barton and Schruben (2001). On the other hand, empirical distributions cannot generate variates outside the observed data (Shanker and Kelton, 1991).

3.3 Random Forest

The preferred machine learning model for our thesis is the Random Forest Algorithm, as it is easy to implement and provides high accuracy. Furthermore, it efficiently deals with many input variables without overfitting the model (Biau, 2010). The Random Forest

Regression Model is an ensemble model based on the fundamentals of decision trees.

According to Cutler et al. (2012), Random Forest is based on a top-down approach known as binary recursive partitioning. The trees partition the predictor space by using a sequence of binary splits on variables. The terminal nodes, the ones that do not split, constitute the entire predictor space. Furthermore, each node that is not terminal splits into two descendent nodes, one going to the left and the other to the right, based on the values of one of the independent variables in the model. Where the predictor variable is continuous, the partition is determined by a split point (pp. 159-161). This concept is illustrated in Figure 3.1.

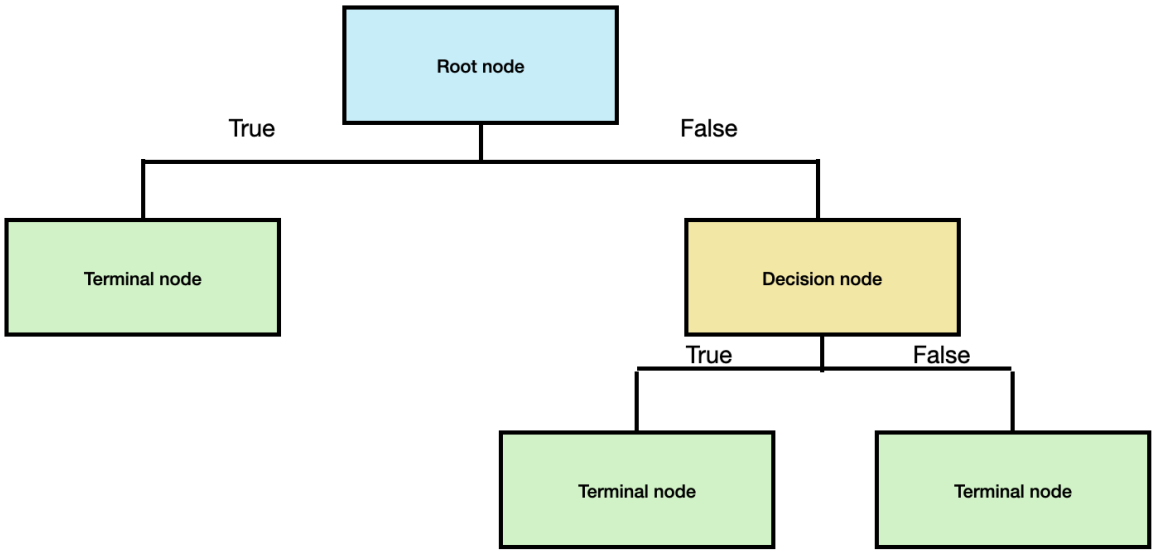

Figure 3.1: Binary recursive partitioning

Furthermore, Cutler et al. (2012) states that a categorical predictor variable x_i retrieves values from a limited set of categories $S_i = s_{i,1}, \ldots, s_{i,m}$, where each split directs a subset to the left and the remaining categories to the right. The specific split used is determined by some criterion; usually, the mean squared residual at the node for regression problems (pp. 159-161).

$$Q = \frac{1}{n} \sum_{i=1}^{n} (y_i - \bar{y})^2 \tag{3.2}$$

Where $\bar{y} = \frac{1}{n} \sum_{i=1}^{n} (y_i - \bar{y})^2$ is the predicted value at the node. Hence, the criterion

measures the "goodness of fit" for which large values imply a poor fit. (Cutler et al., 2012, p. 160).

The approach for deciding the best split for continuous predictor variables entails sorting the values of the predictor and evaluating splits between every unique pair of sequential values. It is typical to use the interval's midpoint, but other interval values might be sufficient for the cause. (Cutler et al., 2012, 158-161).

The partitioning continuously recurses until the stopping criterion is met, and this is common when the unsplit nodes contain fewer than a fixed number of cases. Consequently, this results in terminal nodes, and the predicted value can be retrieved from all the terminal nodes by averaging the response in the case of regression problems (Cutler et al., 2012, pp. 159-161).

Algorithm 1: Binary Recursive Partitioning

Let $\mathcal{D} = \{(x_1, y_1), \ldots, (x_N, y_N)\}$ denote the training data, with $x_i = \left(x_{i,1}, \ldots x_{i,p}\right)^T$.

1. Start with all observations $(x_1, y_1), \ldots, (x_N, y_N)$ in a single node.
2. Repeat the following steps recursively for each unsplit node until the stopping criterion is met:
    a. Find the best binary split among all binary splits on all p predictors.
    b. Split the node into two descendant nodes using the best split
3. For prediction at x, pass x down the tree until it lands in a terminal node. Let k denote the terminal node, and let $y_{k_1}, \ldots, y_{k_n}$ denote the response values of the training data in node k predicted values of the response variable are given by

- $\hat{h}(x) = \bar{y}_k = \frac{1}{n}\sum_{i=1}^{n} y_{k_i}$ for regression
- $\hat{h}(x) = \arg\max_y \sum_{i=1}^{n} I(y_{k_i} = y)$ for classification, where $I\left(y_{k_i} = y\right) = 1$ if $y_{k_i} = y$ and 0 otherwise. (Cutler et al., 2012)

Figure 3.2: Algorithm for Binary Recursive Partitioning (Cutler et al., 2012, p. 161)

As previously mentioned by Cutler et al. (2012), Random Forest uses trees $h_j(X, \Theta_j)$ as base learners. For training data $D = (x_1, y_1), \ldots, (x_N, y_N)$, where $x_i = (x_{i,1}, \ldots, x_{i,p})^T$ denotes the p predictors and y_i denotes the response, then the fitted tree is denoted $\hat{h}_j(x, \theta_j, D)$. The formula above was the original formulation of Breiman's definition.

However, Random Forest does have a component θ_j that implicitly adds randomness (Cutler et al., 2012, 163-164). As the model only uses a random selection of m predictors for all the splits in a tree, the machine learning model decorrelates the tree. As a result, the variance is reduced, which also increases the model's accuracy (James et al., 2021, p. 343).

Algorithm 2: Random Forest

Let $\mathcal{D} = \{(x_1, y_1), \ldots, (x_N, y_N)\}$ denote the training data, with $x_i = \left(x_{i,1}, \ldots, x_{i,p}\right)^T$. For $j =$ 1 to J:

1. Take a bootstrap sample $\mathcal{D}_j$ of size N from $\mathcal{D}$
2. Using the bootstrap sample $\mathcal{D}_j$ as the training data, fit a tree using binary recursive partitioning
    a. Start with all observations in a single node
    b. Repeat the following steps recursively for each unsplit node until the stopping criterion is met:
        i. Select m predictors at random from the p available predictors
        ii. Find the best binary split among all binary splits on the m predictors from step i.
        iii. Split the node into two descendant nodes using the split from step ii-

To make a prediction at a new point x,

- $\hat{f}(x) = \frac{1}{J}\sum_{j=1}^{J} \hat{h}_j(x)$ for regression
- $\hat{f}(x) = \arg\max_{y} \sum_{j=1}^{J} I\left(\hat{h}_j(x) = y\right)$ for classification

Where $\hat{h}_j(x)$ is the prediction of the response variable at x using jth tree (Algorithm 1).

(Cutler et al., 2012).

Figure 3.3: Algorithm for the Random Forest Regression Model (Cutler et al., 2012, p. 164)

3.4 Weather and Seasonality

In the North Atlantic Ocean, winter ranges from December until the end of February, whereas the summer starts in June and lasts until the end of August (Semedo et al., 2008). As a result, the higher latitudes are subject to multiple extratropical storms during winter.

In addition, the North Atlantic Ocean also has an official hurricane season, spanning from June 1 until November 30 (Kossin, 2008).

According to Elsner et al. (1999, p. 67), tropical cyclones will develop near the equator, between 20 degrees north and south latitude, when the ocean is warmest. If the wind speed is below 33 knots, it is called a tropical depression, and a wind speed reaching between 35 and 62 knots is called a tropical storm. Above this value, the storm is considered a hurricane or a severe tropical cyclone which the event is called in the Indian Ocean (Emanuel, 2003). The North Atlantic Ocean has multiple occurrences of tropical cyclones, with many reaching the speed criteria of a hurricane (Elsner et al., 1999, pp. 67-69).

Since the South Atlantic Ocean is in the southern hemisphere, the seasons are different compared to the North Atlantic Ocean, where summer is from December to February and winter is from June to August. Spring is from September to November, whereas fall ranges from March to May (Ramos et al., 2021). Subtropical cyclones can occur in the South Atlantic Ocean, most of which take place during summer, while fall has the most intense storms (Gozzo et al., 2014).

Figure 3.4 is a map displaying the storm tracks of extratropical storms. Furthermore, it indicates that the storms are centered in the high latitudes and are more intensive during the winter because of the high-temperature variance (Bengtsson et al., 2009). In Figure 3.4, the storm tracks are close to the poles and are a consequence of the cold air from the poles mixing with the warmer air moving toward the poles. Therefore, these winds have a temperature difference and can develop a front when they meet. This front would be stronger during the winter because there would be an even more significant temperature difference (Bengtsson et al., 2009; Catto et al., 2012).

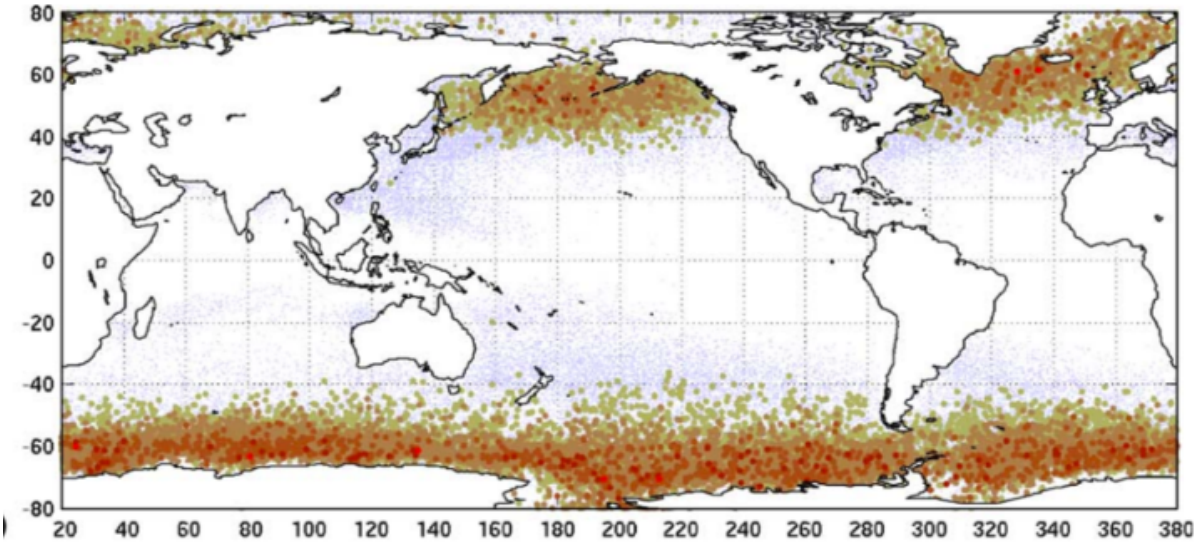

Figure 3.4: Map over extratropical storms occured at sea (Bengtsson et al., 2009)

In the Indian Ocean, the winter season lasts from December until the end of February (Latif et al., 1999). The monsoon season is from June till the end of September, and the post-monsoon season is present in October and November (Krishna, 2009).

Ranking the world oceans by the number of storms, the Indian Ocean appears to be second, slightly behind the Pacific Ocean (Zehnder, 2022). The area is seasonally affected by tropical cyclones and monsoons, both the southwest and the northeast monsoon, due to the extreme seasonal changes in temperature over Asia (Phillips et al., 2021; Emanuel, 2003). The southwest monsoon occurs during the boreal summer months, while the northeast monsoon develops during winter (Phillips et al., 2021). Therefore, two criteria must be met for a monsoon to exist. Firstly, it is a requirement that the summers are wet, whereas the winters are dry in the northern hemisphere. The other criterion is reversing the direction of the prevailing winds (Roux, 2022).

3.5 Ray Tracing

Ray tracing is our preferred method for merging the shipping routes and the relevant weather information. While creating high-realism photos, the algorithm requires much computational power. Research has, as a result, proposed ways of speeding up the process by using additional acceleration data structures such as grids, bounding volume hierarchies,

and KD-trees (Cosenza, 2008).

The new traversal algorithm is fast, straightforward, and extensively used to traverse a ray between a start and an endpoint (Amanatides and Woo, 1987). However, to correctly calculate the traversed grid, one must account for all the grids passed by the ray. Another traversing method is the Bresenham 2D line rastering algorithm, which only includes some grids, as seen in Figure 3.5 (Cosenza, 2008).

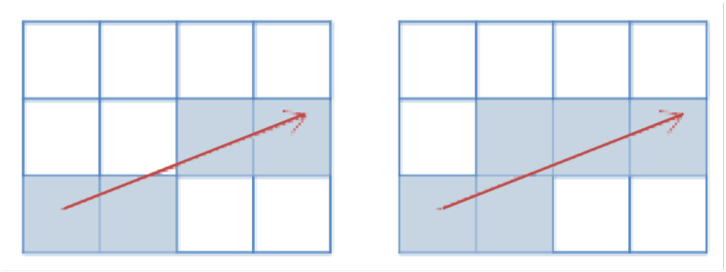

Figure 3.5: Bresenham 2D Line Rastering Algorithm vs. the New Traversal Algorithm (Cosenza, 2008)

The first step when using grids in the ray tracing method is to divide the surface, for instance, the ocean, into uniform voxel spaces (Cosenza, 2008). The next phase uses the new traversal algorithm to find two input variables, X and Y, representing the ray origin grid. Furthermore, *stepX* and *stepY* take on the values 1 or -1, based on the decrementation or incrementation of X and Y as they pass the grid barriers (Amanatides and Woo, 1987).

In addition, we must perform some calculations to find the distance a ray uses on each grid. Here, a variable t represents the ray crossing the first vertical grid barrier, and we store the value in $tMaxX$. Likewise, the value of the first crossing of a horizontal grid barrier is $tMaxY$ (Amanatides and Woo, 1987). The result from the ray trace is the return of all voxels traversed by the ray.

$$f(t) = \overrightarrow{o} + t \cdot \overrightarrow{d} \tag{3.3}$$

Equation 3.3 from Cosenza (2008) is the parametric representation of a ray where the variable $\overrightarrow{o}$ represents the ray's origin and $\overrightarrow{d}$ where the ray is heading. Because the ray traverse voxels along the way, an interval is made as an association with the ray. Regarding

the output, it only considers intersections within this interval $[t_{min}, t_{max})$ usually $[0, +\infty)$ (Cosenza, 2008).

4 Methodology

4.1 Data Acquisition

4.1.1 Weather Data

Vessels can face hazardous extreme weather conditions at sea, in which strong winds and phenomenal waves are particularly relevant (Sienkiewicz et al., 2020). However, such events are difficult to forecast due to significant fluctuations and seasonal variations (Szelangiewicz and Żelazny, 2016). Therefore, our thesis focuses on weather risk and how this affects fuel consumption and TCE, in which we chose wind and waves as our weather variables.

We retrieved relevant data on waves, swell[2], and wind from the Copernicus Marine Service (2022). The gathered information included data from coordinates across the oceans at different time intervals. We used the collected material to understand how fuel consumption is affected by the seasonal climate relevant to each chosen route.

Wind data is registered every six hours in grids of $0,25^o$ x $0,25^o$, while wave data is documented every three hours in grids of $0,2^o$ x $0,2^o$ (Copernicus Marine Service, 2019, 2021). The datasets from Copernicus have three dimensions: time, longitude, and latitude. Furthermore, it includes observations for each grid in the respective time intervals. To better understand how wind and waves affect fuel consumption and TCE, we used eastward and northward wind, wave height, wave direction, swell height, and swell direction as input variables.

4.1.2 Case Study Routes

In addition to weather data, we generated the shortest path for three routes using an Application Programming Interface kindly provided by Dataloy. For the case study, we assume a shipowner has to choose one voyage to assign a vessel located in the Cape of Good Hope. The shipowner can choose whether to lift cargo from Houston in the USA to

[2]Swells are usually longer waves that travel across the ocean surface, and they are not created by local winds. Hence, the generated wind waves are transitioned into swells when they do not propagate more energy (Zhang and Li, 2017).

Rotterdam in the Netherlands, Samarinda in Indonesia to Pipavav in India, or Richards Bay in South Africa, to Mundra in India.

Our motivation for the selected routes is supported by 1) them being common routes for the Supramax vessel for coal and petroleum coke transport and 2) the voyages covering different geographical areas. More importantly, as Figure 4.1 shows, the vessel must sail through areas where we would expect seasonal climate events.

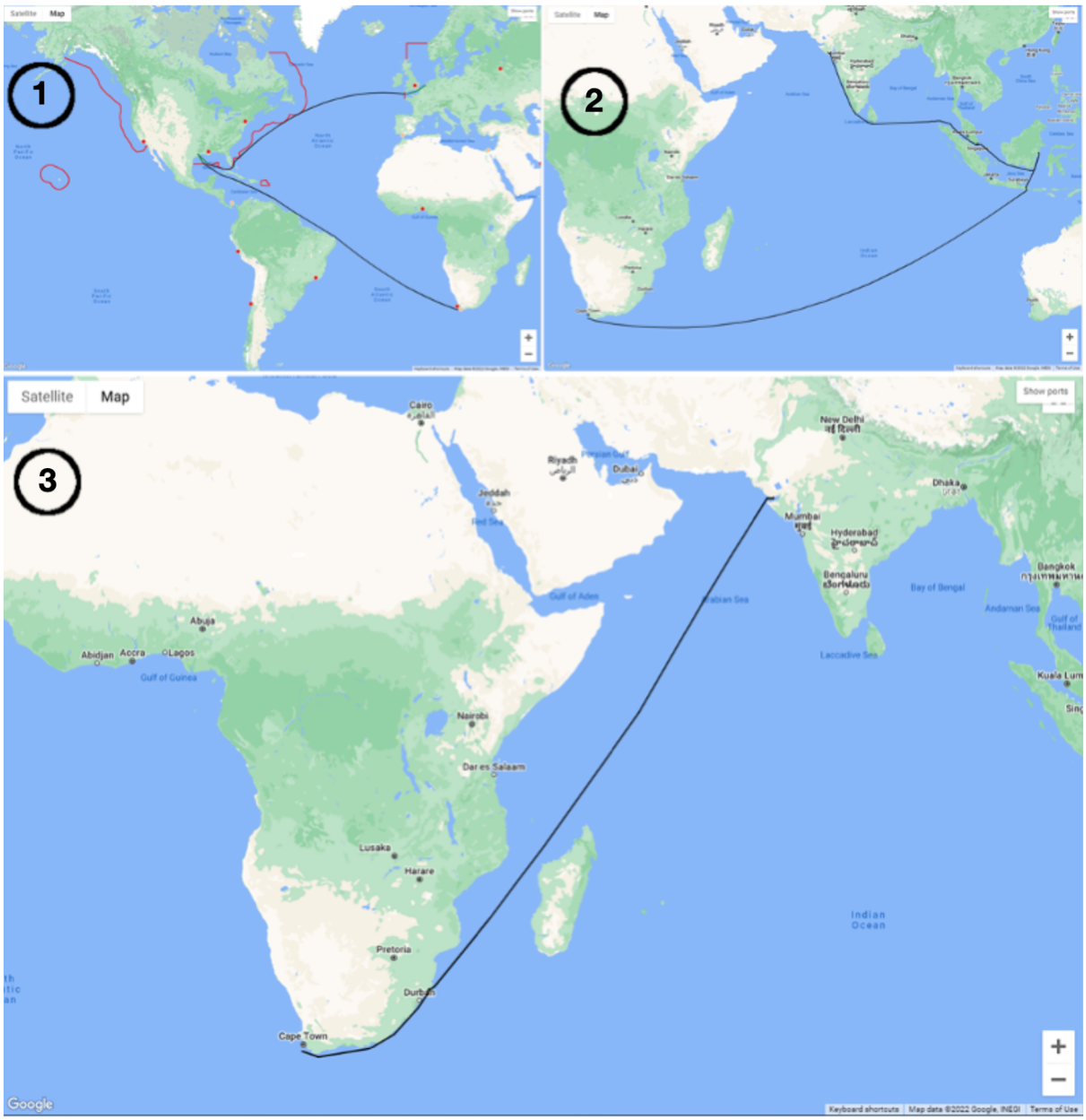

Figure 4.1: The shortest route from Cape of Good Hope to 1) Houston to Rotterdam; 2) Samarinda to Pipavav; 3) Richards Bay to Mundra

4.2 Machine Learning

To connect the weather data to fuel consumption, we used machine learning. To find the best-fitting model, we based our findings on a sample derived from noon data provided by Western Bulk and weather data we collected from the Copernicus Marine Service (2022). The noon data contains information about two different designs of Supramax vessels; Dolphin 64 and Dolphin 38 Green.

In this process, we used Python with its machine learning library Scikit-Learn. We followed standard machine learning procedures, including data pre-processing, training of the data, and an evaluation of the model.

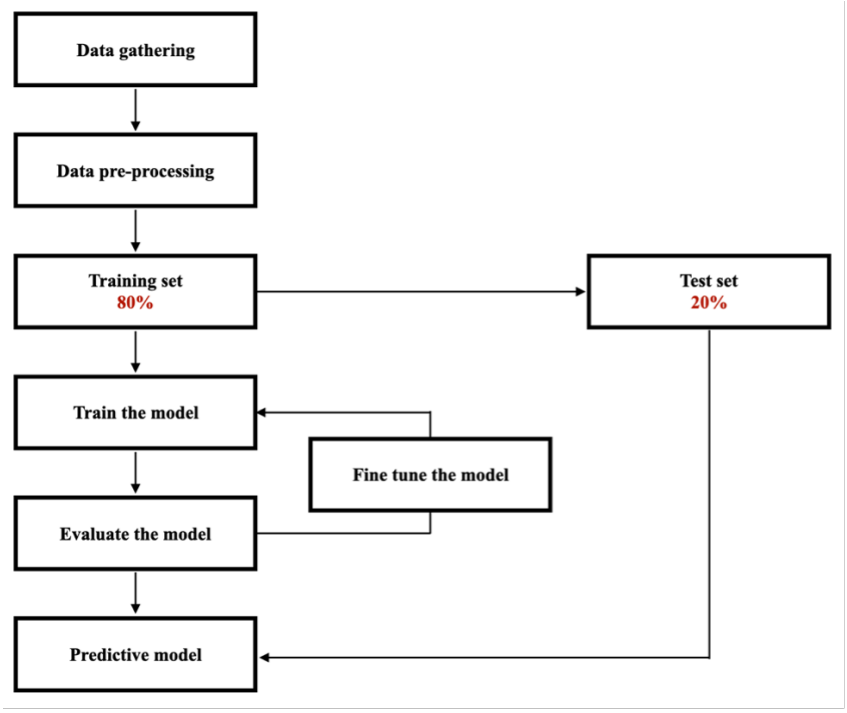

Figure 4.2: Machine learning workflow

In the pre-processing phase, we made binary values for two categorical features; "Design" and "load." However, since we are working with a regression model, we cannot have any categorical values, as the model will not interpret them. Therefore, we decided to make the reference value 1 and the alternative 0. Thus, the ship design Dophin 64 was replaced with 1, and the more fuel-efficient model, Dolphin 38 Green, was substituted with 0. In the case of the "load" feature, 1 represents laden, whereas 0 stands for ballast.

Considering the weather data from Copernicus Marine Service (2019, 2021) is observed

every 3 and 6 hours, and the noon reports register the vessel's location every 24 hours, we had to find vessel coordinates between the reported locations. We used the Application Programming Interface provided by Dataloy (2022) to interpolate the noon reports. Using this interface, we found the shortest distance between the noon report locations to generate waypoints. Generating waypoint coordinates between the noon report locations made it possible to find the weather data affecting the vessels' fuel consumption.

Furthermore, we had to decide what to do with the missing values. In our case, we chose to impute them to have sufficient data. Again, since most of the data missing were apparent wind direction and apparent wind speed for dates after 2019, we were afraid that if we removed all the rows, other vital information would get lost. There are several imputing methods like mean, median, or mode, but we chose to use the KNN method as it looks for characteristics and takes the average of the five closest neighbors. The reason for using the KNN method is that it better preserves the variability and value (Troyanskaya et al., 2001). Moreover, we had to round the number to the closest integer for categorical features ranging from 1-8, as these should not take on decimal values.

Before training our model, we also had to deal with the categorical features. As these variables range from 1-8, the values are treated as ordinal, meaning they have a specific order. Hence, the higher the value, the more it is weighted. However, this is irrelevant to our case, as each number has the same gap interval. To handle this issue, we used one-hot encoding, which means that each value is transformed into a feature with binary values stating whether the observation is true or false.

At the end of the pre-processing phase, we had to deal with outliers. When we explored the dataset, we found significant outliers, which can give a wrongful picture of the data. The deviations will also affect the model's performance. There are several methods to deal with them, but we chose to use the interquartile method, in which we removed all the outliers that were more than three standard deviations from the mean, see Figure 4.3. This makes the machine learning model more robust and accurate (Singh and Haider, 2022).

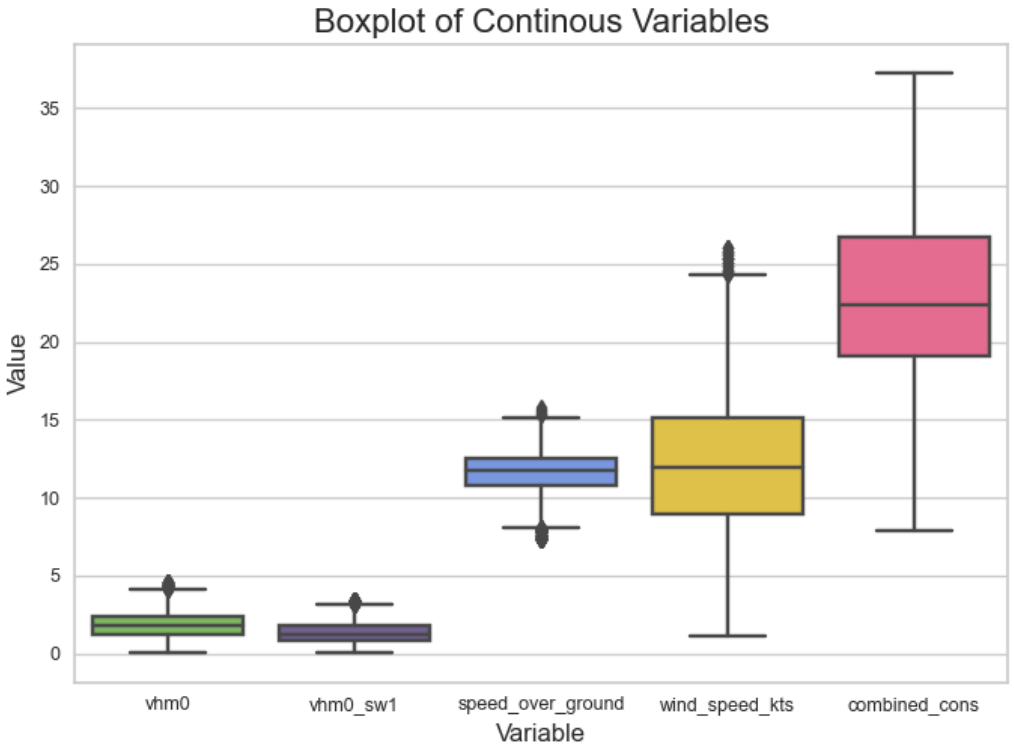

Figure 4.3: Boxplot of continuous variables, showing the removed outliers

When all the steps in the pre-processing phase were completed, we could start the model training. Firstly, the dataset was split into a training and a test set. We used the split ratio of 80 percent as the training set and 20 percent as the test set. There are many common splits in the literature, but we used the 80/20 split as we wanted an extensive training set but tried to avoid overfitting. This split is also said to give the best validity (Gholamy et al., 2018). We then used random generator 42 to be able to replicate the model later on, if necessary, as well as to avoid seasonal patterns.

To conclude on the winning model, we tested several supervised machine learning models to benchmark the performance. These models included Linear Regression, Decision Tree, Random Forest, Support Vector Regression, Lasso Regression, Ridge Regression, Gradient Boosting, and Gaussian Process Regression. Based on what model we trained, we used either the original training data or a scaled one. Linear- and distance-based models depend on scaled data to avoid misrepresented results (Pulagam, 2020). These models included Linear Regression, Lasso Regression, Ridge Regression, KNN, and Support Vector

Regression.

In the evaluation of the model, we used several metrics such as Mean Squared Error (MSE), Mean Root Squared Error (MRSE), Mean Absolute Percentage Error (MAPE), Mean Absolute Error (MAE), and the coefficient of determination (R2). The choice of performance measures is based on Nilsson and Nilsson's (2021) paper, as we wanted to compare our results.

4.3 Generating Weather Routing Distributions

The generated shortest path for the three case routes provides realistic voyages. In addition, the resulting dataset gives us multiple coordinates, the latitude, and the longitudes a vessel has to pass through on each course.

We are using the Ray Tracing Algorithm to connect weather data to the routes of study, see Figure 4.4. The algorithm extracts the grids that cross paths with the routes to collect weather information directly impacting the voyage. We use the grids from the weather dataset to generate the weather routing distributions and analyze how it will affect the decision of which route to choose when seasonal changes occur.

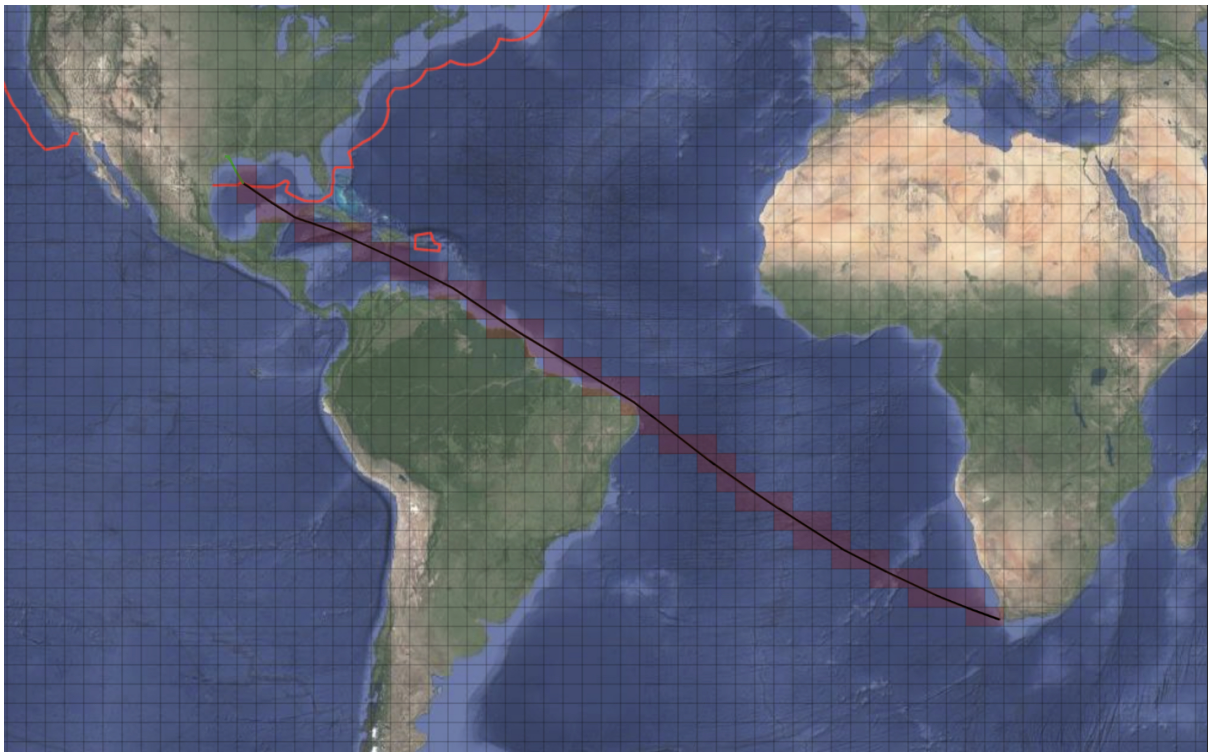

Figure 4.4: Ray tracing on a route to display the concept

Connecting weather to the routes has to be completed twice, one for each weather variable due to different time intervals. For waves, we can make waypoints for the voyage every 3 hours and obtain weather information related to the corresponding coordinates, whereas, for wind, a waypoint can first be created after 6 hours.

Connecting the weather variables to both legs, (rendezvous to the loading port, then to discharging port), the first step is to perform an interpolation between the routing points for each of the three routes. This method provides a set of waypoints which are the coordinates of where the vessel will end up every 3 hours. The interpolation is accomplished using a fixed speed over ground of 12.5 knots and the Haversine Function to find the vessel's location at the three-hour mark.

In our thesis, we used the Haversine method to calculate the distance between two positions. This formula is an integral equation within the navigation field, as it is possible to find the arc distance between two points on a sphere based on longitude and latitude parameters. The concept of Haversine dates back to 1805 under the table entitled "logarithmic versed sines" (Brummelen, 2021, p.268). Furthermore, the Haversine equation searches for a triangle's side and angle relationship in a spherical plane, also known as the Law of Haversine (Ikasari et al., 2021).

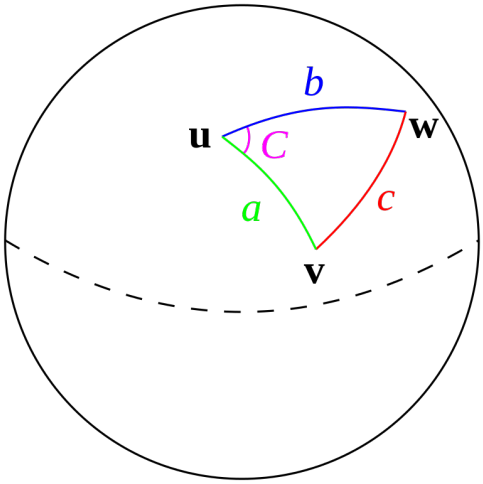

Figure 4.5: The Spherical Triangle (Hartanto et al., 2017)

The Haversine formula aims to describe all equations related to the Earth by eliminating the factors that cause the slightly elliptical form (Ikasari et al., 2021). In the sphere, the triangular shape on the surface connects the points u, v, and w, as seen in Figure 4.5.

The algorithm establishes a direct distance between the points, creating a, b, and c. The Haversine formula is presented as follows (Korn and Korn, 2000, pp. 892-893):

$$hav(\frac{d}{r}) = hav(\theta_2 - \theta_1) + cos(\theta_1) \cdot cos(\theta_2) \cdot hav(\lambda_2 - \lambda_1) \tag{4.1}$$

In Equation 4.1, d represents the distance between the two points, r is the radius of the sphere, θ_1 and θ_2 is the latitude of points 1 and 2 in radians, and λ_1 and λ_2 stands for the longitude of points 1 and 2 in radians, respectively.

Furthermore, the left side of the equation, $\frac{d}{r}$, is the central angle. Therefore, to solve for the variable, d, we will have to apply the inverse Haversine, or use the arcsine, shown in Formula 4.2 (Gade, 2010).

$$d = 2rarcsin\sqrt{sin^2(\frac{\theta_2 - \theta_1}{2}) + cos(\theta_1) \cdot cos(\theta_2) \cdot sin^2(\frac{\lambda_2 - \lambda_1}{2})} \tag{4.2}$$

From our routes and weather data interaction, we derive variables for apparent swell, wind, and wave direction. The explicit directions of these parameters, presented in Figure 4.6, are related to the vessels heading from waypoint t to waypoint $t + 1$. Here, we assigned values from 1 to 8 depending on which direction the weather encounters the ship. Nilsson and Nilsson (2021) states in their paper that "speed over ground" is the most influential predictor for fuel consumption. Given this information, we have included this variable in our analysis.

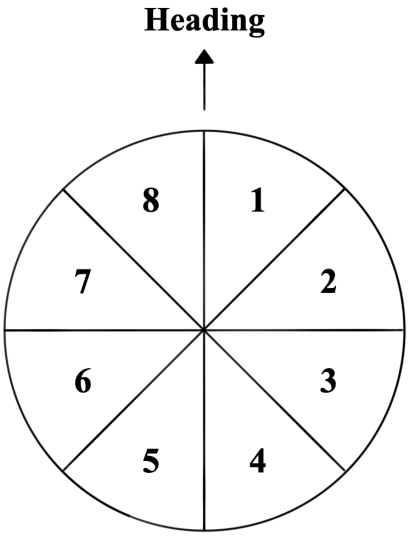

Figure 4.6: Apparent wind, wave, or swell direction based on the vessel's heading

Originally the retrieved data from Copernicus Marine Service (2019) listed wind in the form of northward wind and westward wind in meters per second. Equation 4.3 and Equation 4.4 below show how the northward (v) and the westward (u) wind are calculated. In continuance with the calculations of fuel consumption, these variables must be transformed into wind speed in knots. The conversion is estimated with Equation 4.5, multiplied by 1.94384449, representing the value of one meter per second in knots (Johansson and Bolin, 2019). Finally, Equation 4.6 represents the calculation of wind direction.

$$u = V_s \cdot sin(V_d \cdot \frac{\pi}{180}) \tag{4.3}$$

$$v = -V_s \cdot cos(V_d \cdot \frac{\pi}{180}) \tag{4.4}$$

$$V_s = \sqrt{u^2 + v^2} \tag{4.5}$$

$$V_d = mod((270.0 - arctan(v, u) \cdot \frac{\pi}{180}), \frac{\pi}{180}) \tag{4.6}$$

Since both interpolated files have the same route information, equal starting dates, and

time values, it is possible to merge them. This resulted in a dataset displaying all waypoints for the three routes, with voyages starting every day from 2006 to the end of 2019.

Next, we imputed the missing numbers for wind speed and apparent wind direction by using the average value and mode. Thereafter, the missing numbers were calculated based on the monthly weather for each separate route. Furthermore, we had to make adjustments corresponding to the dataset from the machine learning model to predict fuel consumption. Thus, we added values for the "load" variable, representing a ballast vessel for the first leg and a loaded vessel for the second leg to the discharging port.

The routes will encounter different seasons depending on geographical location. To avoid confusion, we will refer to December, January, and February (DJF) as one period, March, April, and May (MAM) as the second, June, July, and August (JJA) as the third, and September, October, and November (SON) as the fourth. Since a voyage starts every day for 14 years, many will cross pre-defined periods. Therefore, we sorted the trips based on which period the voyage spent the majority of the days in.

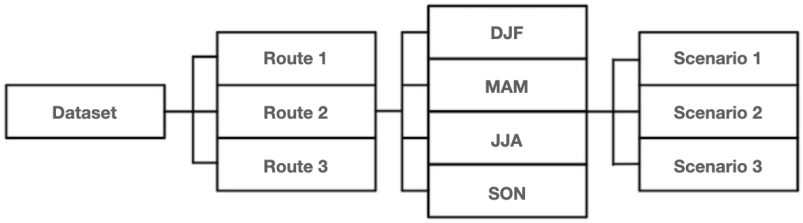

Figure 4.7: Routes, periods, and scenarios

Furthermore, we had to make adjustments corresponding to the dataset from the machine learning model to predict fuel consumption. First, we removed unnecessary columns and adapted the dataset to only one observation per day for each voyage, as the training set was based on noon reports. Furthermore, we used the ship design Dolphin 64 for all observations and a fixed speed over ground of 12.5 knots. Afterward, we removed the outliers and added dummy variables identical to the training set. Joblib[3] was then used to predict fuel consumption based on our input variables. Moreover, we found the total fuel consumption for each voyage, creating distributions for each of the routes for each period, which was further used for the TCE calculations.

[3]Joblib is a Python library that stores the data for later use and ensures reproducibility (Joblib, 2021).

4.4 Estimating TCE Distributions

Next, we simulated fuel consumption as a part of the TCE calculation. This is because simulation is a rational risk analysis and decision-making tool (Marklund and Laguna, 2018, pp. 257-259). Considering the case study, we calculated the TCE for each scenario for the respective routes and periods. The purpose was to get one TCE simulation for each scenario, resulting in different distributions.

The simulation calculates TCE using the uncertain input variable, fuel consumption, as well as the fixed inputs trip duration, port costs, bunker fuel prices, and freight rate. Then, the simulation will repeat the process of calculating the TCE, generating a final distribution. As shown in Table 4.1, the freight rate and other costs vary based on the three scenarios; low bunker price, mean bunker price, and high bunker price. See Table A.1 and Table A.2 in the Appendix for information about the routes and port costs.

We ran simulations on all the routes, resulting in a Time Charter Equivalent distribution for each period and scenario. We used the TCE formula from Equation 3.1 in Section 3. For example, the route from Cape of Good Hope to Samarinda to Pipavav in the high bunker price scenario will be calculated with the following formula:

$$TCE = \frac{\frac{11.40\$}{tonne} \cdot 50,000\ tons - (\frac{549.21\$}{tonne} \cdot FC) - (13,309\$ + 56,289\$)}{31.28\ days + 4\ days\ at\ port} \tag{4.7}$$

Table 4.1: Bunker price and freight rate based on scenarios

Number listed in $/tons [4]	Cape of Good Hope Houston - Rotterdam		Cape of Good Hope Samarinda - Pipavav		Cape of Good Hope Richards Bay - Mundra	
	Bunker price	Freight rate	Bunker price	Freight rate	Bunker price	Freight rate
Low bunker scenario	HSFO: 379.33 ULSFO: 457.85	18.00	HSFO: 379.33	9.00	HSFO: 379.33	12
Mean bunker scenario	HSFO: 479.00 ULSFO: 571.00	13.25	HSFO: 479.00	9.20	HSFO: 479.00	15
High bunker scenario	HSFO: 549.21 ULSFO: 636.18	21.25	HSFO: 549.21	11.40	HSFO: 549.21	15.25

[4]Low bunker scenario numbers are from 2019-01-02, mean bunker scenario is from 2019-07-12, and high bunker scenario from 2018-10-24 (Clarksons Shipping Intelligence Network, 2022).

5 Assumptions

This thesis is based on several assumptions that are important to consider when interpreting the results. These assumptions include days at ports, fixed input variables, and the perspective of cost-minimizing.

The assumption of days at port refers to how the vessel spends two days at each port on the different routes. In total, this adds four days to each of the routes, in which two days go to the loading ports and two days are spent at the discharging ports. Accordingly, the productivity at each of the ports also remains the same. Although four days in the real world are realistic, it might deviate slightly, resulting in a marginally inaccurate number of days on a voyage for the TCE calculations.

Furthermore, we assume that some of our input variables are fixed in order to simplify the analysis and focus on the effects of the other variables, which are more of interest in this thesis. When predicting fuel consumption, we are studying a particular vessel, Dolphin 64, and we keep the speed over ground constant as we are more interested in how the weather variables affect the total consumption.

Lastly, the thesis is based on the assumption that the optimal route is solely based on an evaluation from a cost perspective where the best decision always will be the route with the least costs rather than considering other factors. Hence, the analysis does not take into account that some of the routes might increase the risk to the people onboard the vessel, the vessel itself, or environmental impacts such as the marine fauna.

It is important to keep the assumptions above in mind when interpreting the results of this thesis and consider potential limitations or biases that could be a result of these premises.

6 Results

6.1 Descriptive Statistics

6.1.1 The North Atlantic Ocean

To better understand the climate data, we created maps displaying the wave height and wind speed in the different areas of study. The height and speed are color-coded, in which dark blue represents calm weather, whereas yellow indicates high activity. These values are averaged across time. For example, if we look at the North Atlantic Ocean, there are seasonal wave height and wind speed patterns. The area around the Caribbean is reasonably still regardless of season, but the regions further north, are more prone to weather events related to the periods.

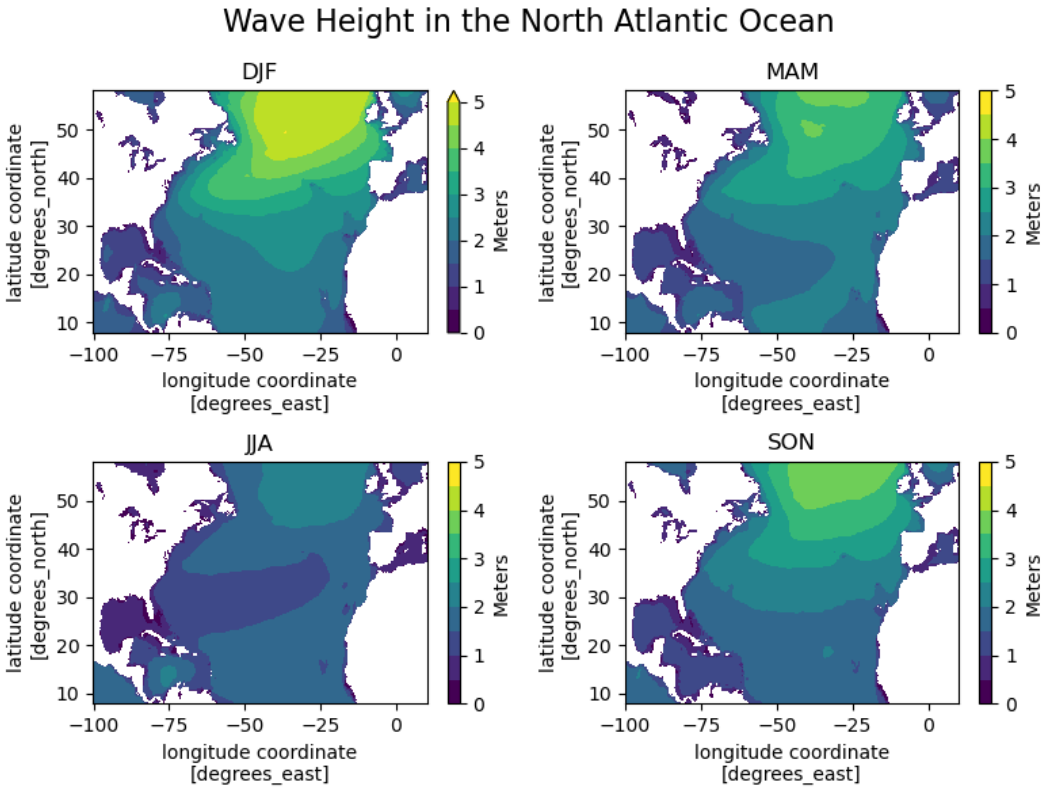

Figure 6.1: Mean wave height in the North Atlantic Ocean

The winter in the North Atlantic Ocean constitutes the months of December, January, and February. These months are more affected by extreme weather events than other seasons. Further, this is in line with the findings of area-specific weather during the winter,

where many extratropical storms occur on the East Coast of North America (Bengtsson et al., 2009). The area is susceptible to these storms due to the westerlies that create a high-pressure belt. These phenomena can be seen in Figure 6.1 and Figure 6.2.

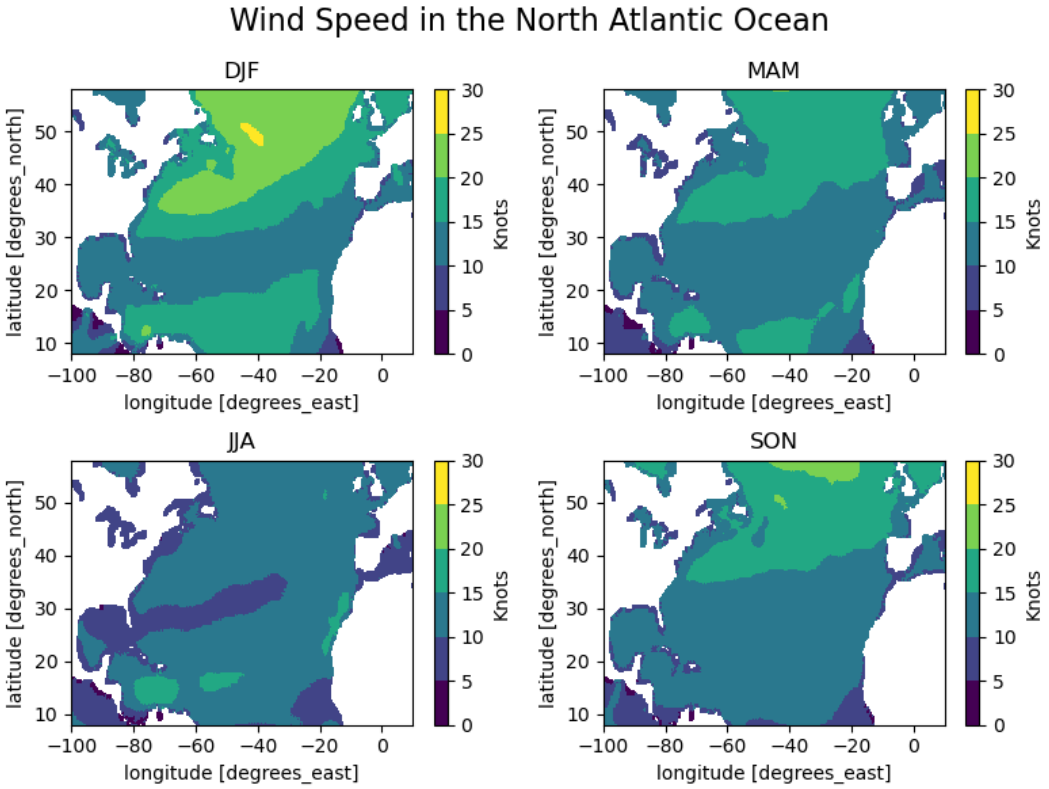

Figure 6.2: Mean wind speed in knots in the North Atlantic Ocean

If we look at Table 6.1, we see that the wave height has an average of 2.76 meters during DJF, which is considerably more than the months of JJA. These months equate to summer in the North Atlantic. Furthermore, this aligns with our wind speed findings in Table 6.2. The standard deviations are consistent with what to expect and do not deviate significantly from the means. Moreover, it presents a peak of 127.96 knots in the winter, but JJA closely follows it with a maximum of 126.22 knots. This indicates that although DJF usually is more exposed to severe weather, the summer might have more volatile weather events. Even though the weather seems reasonably reliable, which can be seen through the 95 percent quantile, there are some extreme weather-related incidents.

Table 6.1: Summary statistics of the North Atlantic Ocean - Wave height

Period	Mean	Standard Deviation	Max	Min	95% Quantile
DJF	2.76	1.56	17.78	0.00	5.84
MAM	2.15	1.58	14.91	0.00	4.40
JJA	1.54	0.69	14.32	0.00	2.69
SON	2.10	1.20	15.25	0.00	4.44

Table 6.2: Summary statistics of the North Atlantic Ocean - Wind speed

Period	Mean	Standard Deviation	Max	Min	95% Quantile
DJF	16.28	7.56	127.96	0.00	30.11
MAM	14.03	6.57	110.14	0.00	27.99
JJA	11.50	5.25	126.22	0.00	20.06
SON	13.50	6.73	116.01	0.00	25.75

6.1.2 The South Atlantic Ocean

The westerlies also affect the South Atlantic Ocean, as this zone is located on both hemispheres (Lee et al., 2019). Due to this phenomenon, the ocean will experience high-pressure fronts making it prone to extratropical storms during the winter months: June, July, and August (JJA). This can be observed from the higher waves and more wind activity in the southern parts. However, the areas near the equator are very tranquil during all seasons. Compared to the North Atlantic, DJF is the calmest month in the South Atlantic Ocean, as we can see from Figure 6.3 and Figure 6.4.

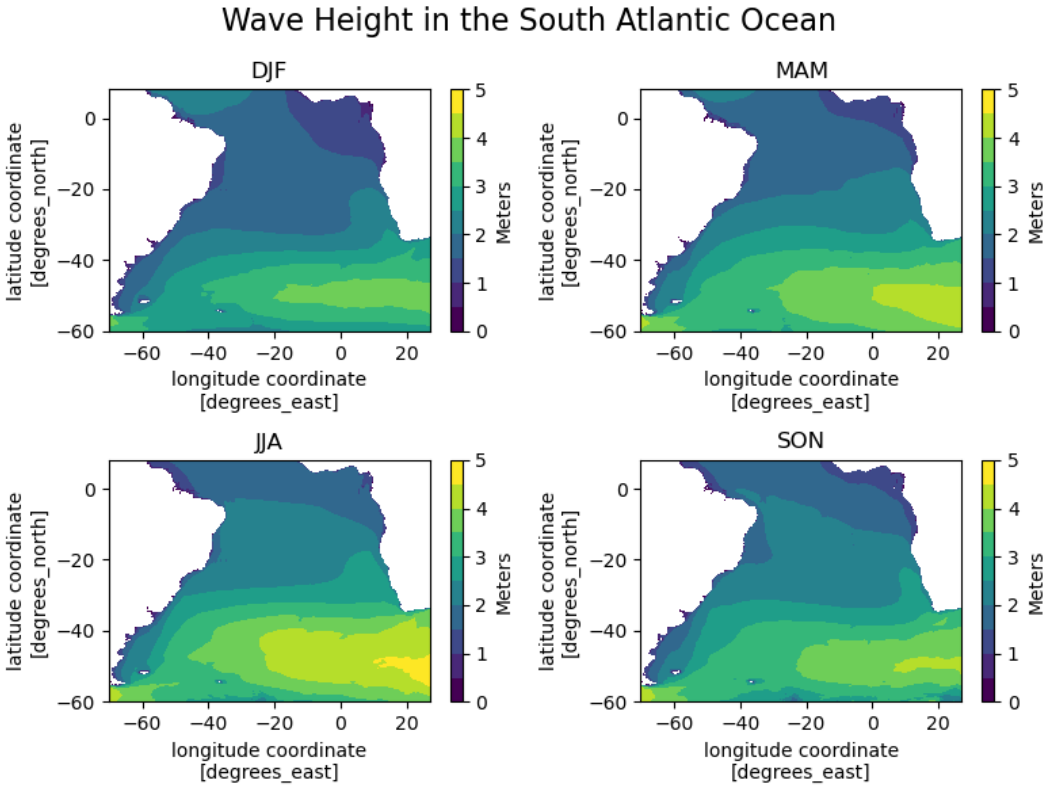

Figure 6.3: Mean wave height in the South Atlantic Ocean

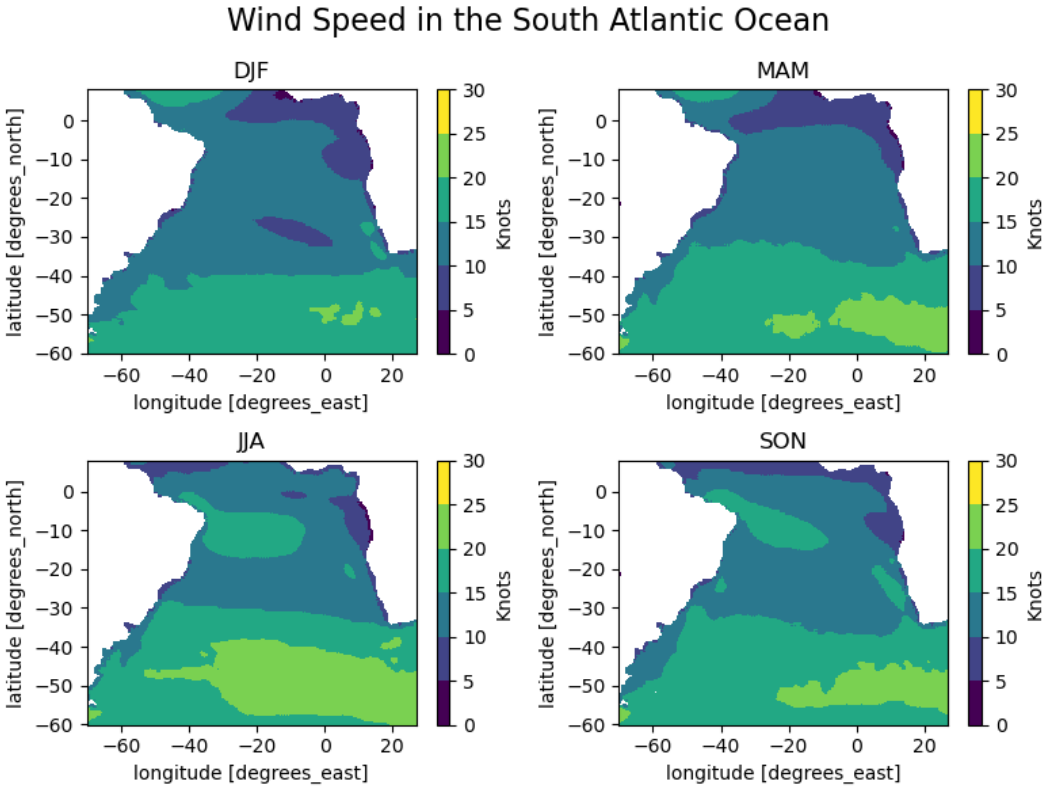

Figure 6.4: Mean wind speed in knots in the South Atlantic Ocean

Table 6.3 and Table 6.4 indicate a few seasonal wind speed and wave height variations by looking at the mean values. The standard deviations, on the other hand, are relatively high for all the periods in wave height, and they are fairly similar for wind speed. The summary statistics show that SON has the highest wave observation of 15.36 meters and a maximum wind speed of 116.29 knots. This implies that the South Atlantic Ocean is occasionally subject to extreme weather events in normally quiet months.

Table 6.3: Summary statistics of the South Atlantic Ocean - Wave height

Period	Mean	Standard Deviation	Max	Min	95% Quantile
DJF	2.31	1.07	13.72	0.00	4.41
MAM	2.63	1.22	14.83	0.00	5.63
JJA	2.90	1.36	14.61	0.00	5.58
SON	2.58	1.18	15.36	0.00	4.93

Table 6.4: Summary statistics of the South Atlantic Ocean - Wind speed

Period	Mean	Standard Deviation	Max	Min	95% Quantile
DJF	13.82	6.23	94.07	0.00	25.22
MAM	14.79	6.86	123.98	0.00	27.36
JJA	16.23	7.32	96.73	0.00	29.64
SON	15.21	6.68	116.29	0.00	27.40

6.1.3 The Indian Ocean

As seen in Figure 6.5 and Figure 6.6, the Indian Ocean has a different pattern as they do not operate with the same seasons as the Atlantic Ocean. We see that the weather activity is relatively low in the winter months, DJF, and the summer, which equates to MAM. However, during the monsoon season, JJA, there are generally high waves and more substantial wind speeds due to the westerlies and the monsoons. This weather also affects SON as September is commonly defined as a part of the monsoon season.

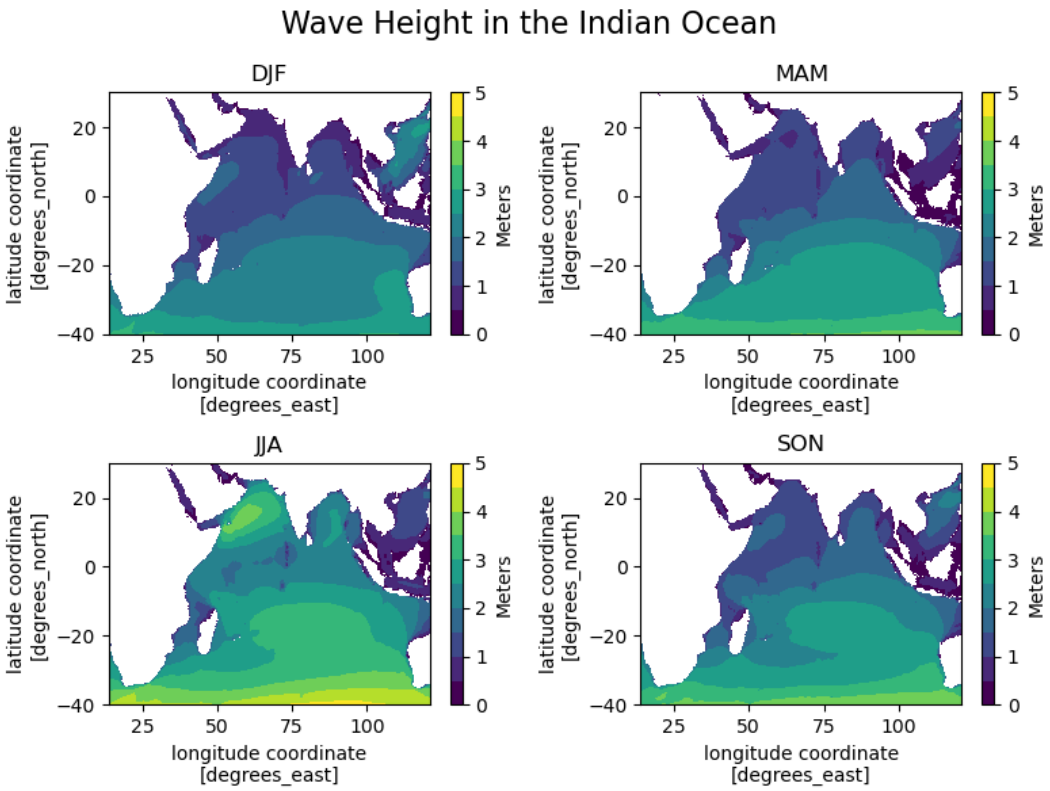

Figure 6.5: Mean wave height in the Indian Ocean

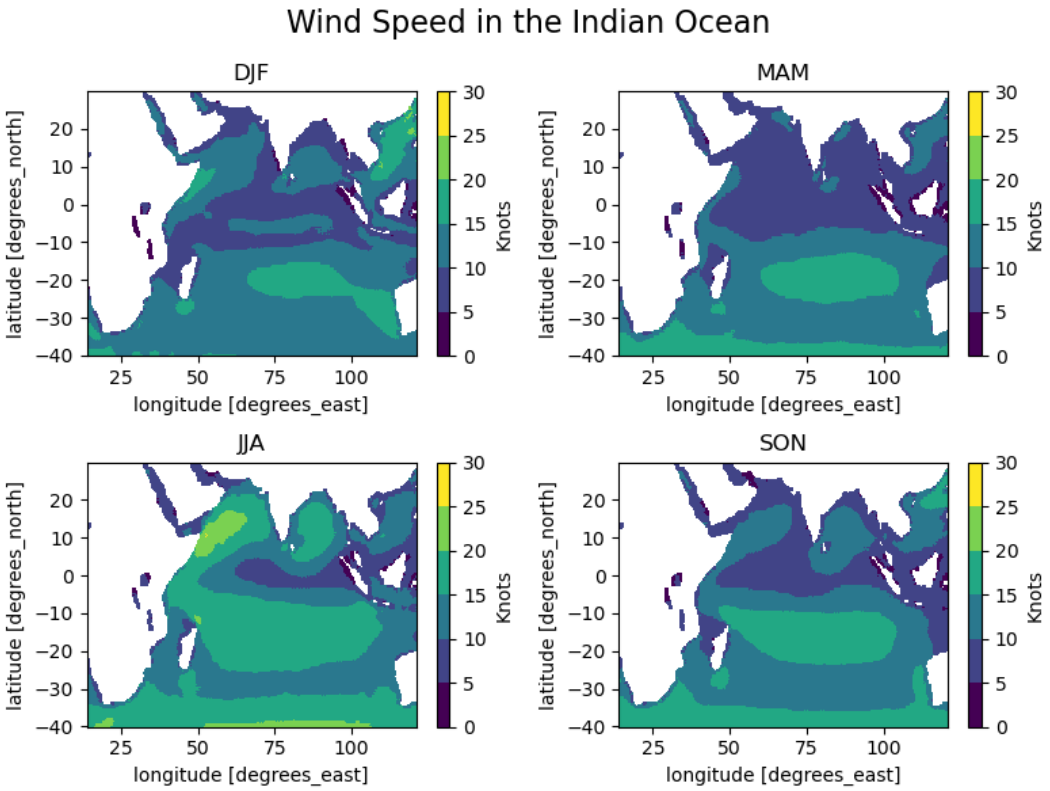

Figure 6.6: Mean wind speed in knots in the Indian Ocean

Regarding the standard deviation, Table 6.5 shows that it is not increasing proportionally. However, the disproportionality between the wave height and the associated standard deviation indicates that the monsoon season is generally prone to higher waves on average. In addition, Table 6.6 shows that the mean wind speed is substantially stronger during the monsoon season, which averages 14.17 knots. However, MAM is more susceptible to fluctuations as the maximum wave height is approximately 16 meters, which is remarkably higher than the maximum in the other periods.

Table 6.5: Summary statistics of the Indian Ocean - Wave height

Period	Mean	Standard Deviation	Max	Min	95% Quantile
DJF	1.83	0.88	13.74	0.00	3.37
MAM	1.98	1.09	16.01	0.00	3.86
JJA	2.62	1.21	13.52	0.00	4.72
SON	2.12	1.09	13.42	0.00	4.05

Table 6.6: Summary statistics of the Indian Ocean - Wind speed

Period	Mean	Standard Deviation	Max	Min	95% Quantile
DJF	11.60	5.51	109.30	0.00	20.93
MAM	11.18	5.98	117.38	0.00	21.53
JJA	14.17	6.29	122.55	0.00	24.42
SON	11.84	5.85	114.43	0.00	21.53

6.1.4 Route 1: Cape of Good Hope - Houston - Rotterdam

Figure 6.7 shows the wind speed and direction found on the routes for each corresponding period. The wind speed is grouped into 13 categories based on the Beaufort Scale, where 0 indicates calm wind, whereas 12 implies a hurricane as the wind surpasses 65 knots (Perlewitz, 1936).

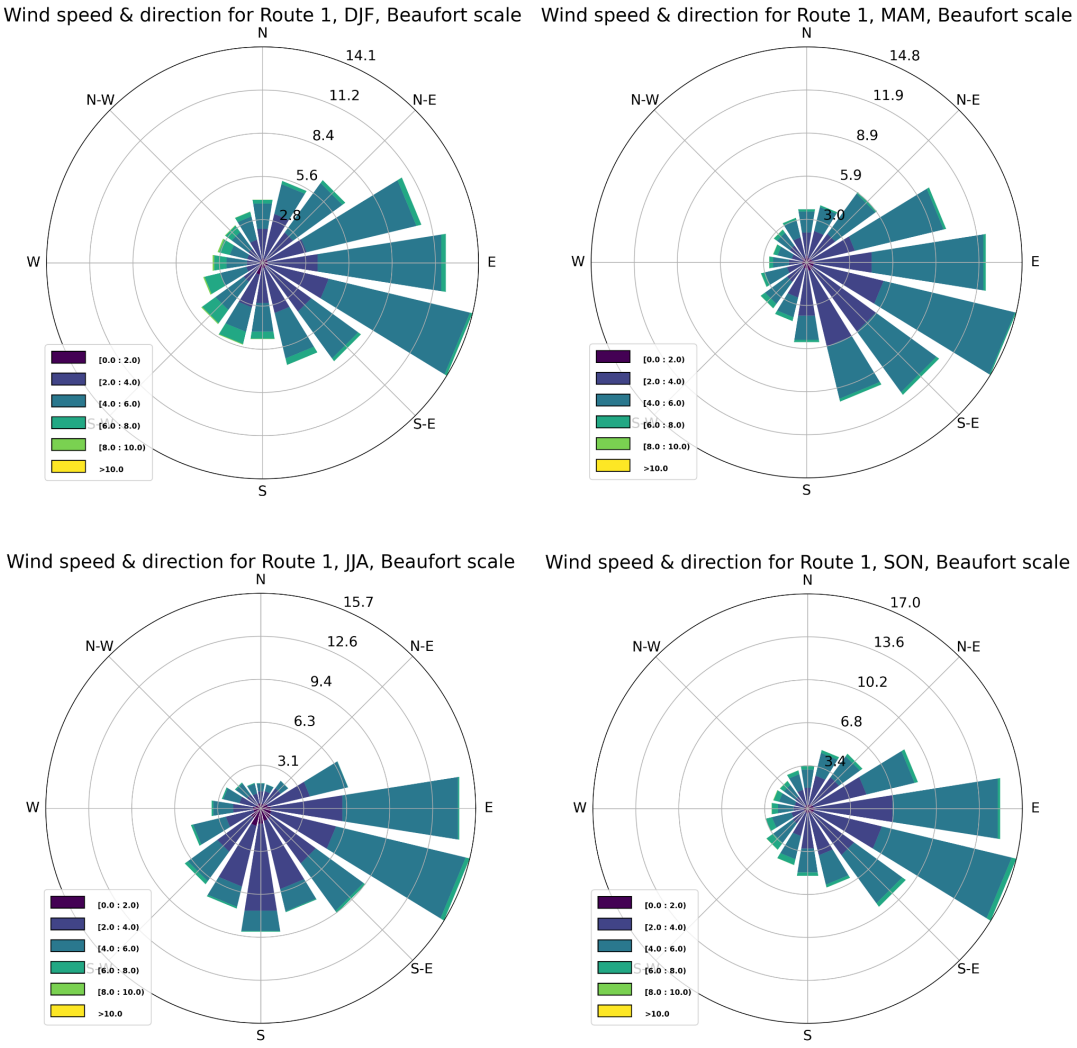

Figure 6.7: Wind speed and direction for Route 1, Beaufort Scale

By using this scale, we can see that the wind mainly came from the east in December, January, and February. The wind speed was categorized as 4 and 5, which equates to the range between 14 and 17 knots. However, we see instances where the wind speed is defined as a tropical depression (Perlewitz, 1936; Emanuel, 2003). For MAM, there are fewer events that can be identified as tropical depressions, as we see calmer winds. For the months of JJA, the wind rose plots indicate even calmer winds. Furthermore, the period SON seems to be more susceptible to higher wind speeds compared to JJA, which could indicate a hurricane season.

6.1.5 Route 2: Cape of Good Hope - Samarinda - Pipavav

For DJF in route 2, Figure 6.8 show that the winds are quite calm most of the time. However, there are some instances where the wind speed reaches category 6 to 8 on the Beaufort Scale, which means that there is a tropical depression (Perlewitz, 1936; Emanuel, 2003). The wind speed is greatly reduced for the period MAM, although there are some occurrences of tropical depressions. Furthermore, we see the winds coming from the southeast and east. In the period JJA, which is the monsoon season, there is a higher quantity of wind in the Beaufort Scale category 6 to 8. We see that the intensity has increased, even though severe tropical storms rarely occur. During SON there are also some instances of higher wind speed, but the average winds seems to be relatively calm.

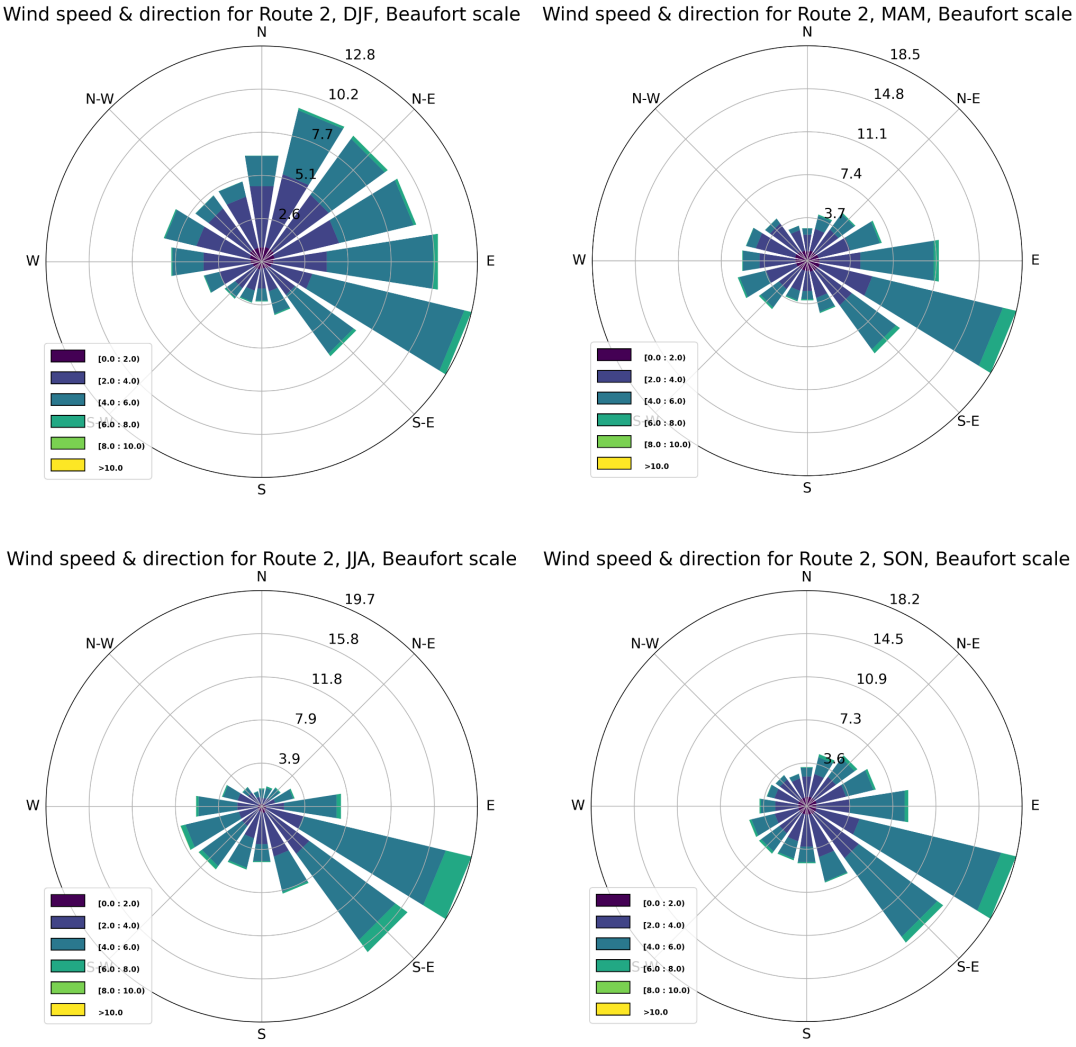

Figure 6.8: Wind speed and direction for Route 2, Beaufort Scale

6.1.6 Route 3: Cape of Good Hope - Richards Bay - Mundra

The period DJF for route 3 in Figure 6.9 has very few cases of wind speed reaching the same capacity as the two other routes. The wind speed for the route to Mundra is mostly between 4 and 6. JJA is the period with the highest number of observations reaching tropical depressions between categories 6 and 8. The rose plot shows that SON is facing calmer winds, although stronger winds occur.

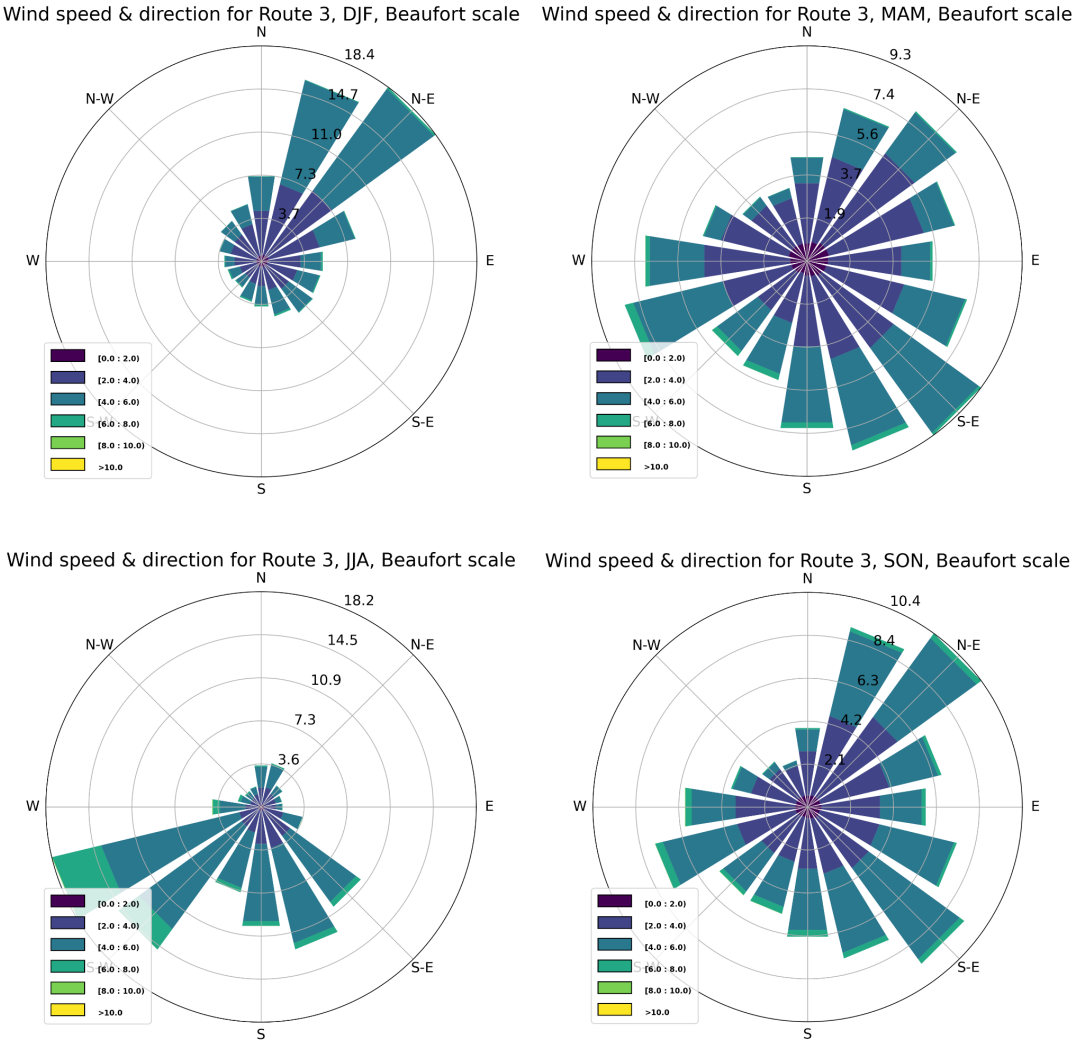

Figure 6.9: Wind speed and direction for Route 3, Beaufort Scale

6.2 Machine Learning

6.2.1 Model Selection and Prediction Accuracy

As presented by Nilsson and Nilsson (2021), the best-fitted machine learning model is evaluated based on a series of performance metrics. It is much debated in the literature what measures give the best evaluation. Hence, we chose to take several into account, coefficient of determination (R^2), Mean Absolute Percentage Error (MAPE), Mean Absolute Error (MAE), Mean Squared Error (MSE), and Root Squared Error (RMSE). These measures aim to give an overview of how well the models perform. Therefore, we can compare all the models against each other.

We tested several machine learning models, including Linear Regression, Decision Tree Regression, Random Forest, Support Vector Regression, Extra Trees, Lasso, Ridge, Gaussian Process, and Gradient Boosting. We fitted the training set and tested it against the test set for all of these models. We used the same dataset with "fuel consumption" as a response variable to get a consistent evaluation when training all the different regression models.

Table 6.7: Summary of performance metrics from the machine learning models

Model	R^2 (in %)	MAPE (in %)	MAE	MSE	RMSE
Linear Regression	60.08	11.13	2.49	9.71	3.12
Decision Tree Regression	36.26	13.73	2.97	15.50	3.94
Random Forest Regression	63.96	10.25	2.26	8.76	2.96
Support Vector Regression	63.08	10.58	2.32	8.98	3.00
Extra Trees Regression	62.70	10.37	2.29	9.07	3.01
Lasso Regression	23.14	16.17	3.63	18.69	4.32
Ridge Regression	60.08	11.33	2.49	9.71	3.12
Gaussian Process	-40.96	35.77	4.3	34.27	5.85
Gradient Boosting	63.65	10.51	2.32	8.84	2.97

Table 6.7 shows that the model giving the best coefficient of determination is the Random Forest Regression, followed by Gradient Boosting, Support Vector Regression, and Extra

Trees. This measure tells us how much the different variables can explain the outcome. In this case, the random forest regression has an explanatory power of 63.96 percent. This tells us that the model can correctly predict approximately 64 percent of the time. Furthermore, this percentage does not indicate that the model is overfitted, as we cannot expect a perfect fit. Although this measure implies which model performs best, we will examine the model's errors.

The RMSE is one of the most commonly used performance metrics within machine learning. This is also the error term the Nilsson and Nilsson's (2021) used in their thesis. Table 5.7 also shows that the regression with the lowest RMSE is the Random Forest with only 2.96, slightly less than Gradient Boosting, which has a RMSE of 3.97. Furthermore, this sufficiently matches the other performance metrics, as the model provides the lowest MSE, MAE, and MAPE values. As a result, we conclude that the random forest regression is the best-performing model for predicting fuel consumption based on our chosen variables. However, many of the compared regression models perform almost equally well.

To better understand the Random Forest Regression model, Figure 6.10 shows an extract of the whole forest. As we can see, the root node states that if the design is less than 0.5, then we continue to the decedent node on the left, whereas if the design is above 0.5, we will go to the right. This tells us that the first split is related to the ship design, which in our sample consists of either the fuel-efficient Dolphin 38 Green or the baseline model, which is Dolphin 64. Furthermore, we see that both alternative decedent nodes set out statements concerning the speed over the ground. For each node, we get information about the statement, squared error, the sample size, and the value equal to fuel consumption. Although this is only an extract of a much bigger forest, it efficiently illustrates the model, meaning we can see how the features and their importance navigate the observation through the forest before it ends up with the predicted fuel consumption. For example, Figure 6.10 indicates that a vessel of type Dolphin 38 Green with speed over ground above 12.175 has a fuel consumption of 20.16. In contrast, a ship of the type Dolphin 64 with speed over ground above 11.675 has a predicted fuel consumption of 22.509. If we had broken down the tree further, the outcome would have turned out slightly different. However, the Random Forest Algorithm used this recursive binary partitioning method to predict fuel consumption.

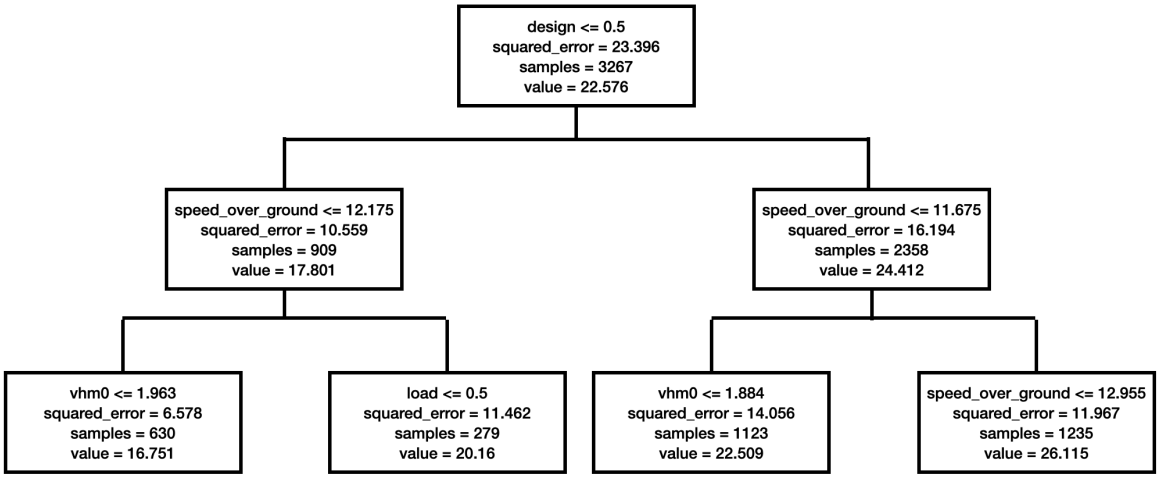

Figure 6.10: Random Forest Model

The Random Forest model explains approximately 64 percent of the variance of the response variable, and the average prediction error was about 10.25 percent, equating to 2.26 tons of fuel. Furthermore, the errors from the model are illustrated in Figure 6.11, where we can see that the most significant fuel consumption was about 37 tons, whereas the model predicted around 22 tons. Hence, the error was 14 tons. If we look at the plot showing the predicted values vs. the residuals, there are clear indications that most errors lie between 7 and -7 tons.

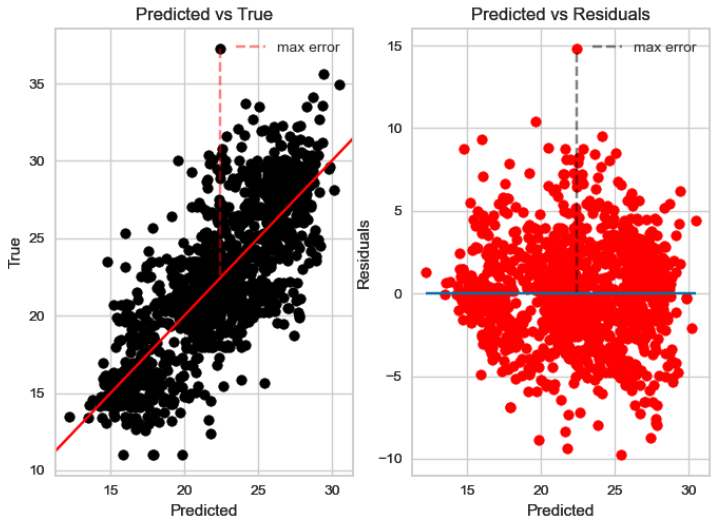

Figure 6.11: Plot of the errors

6.2.2 Feature Importances

For machine learning models, it is evident to understand what factors have the most influence on the model's performance. To comprehend the different variables' impact on the prediction, we found the importance of the various features in our Random Forest model. As seen in Figure 6.12, the "design" variable affects the prediction outcome the most. This makes sense as the model accounts for two designs: the normal one, Dolphin 64, and the other, a more fuel-efficient model, known as Dolphin 38 Green. Considering we are predicting fuel consumption, it seems fair that this is the single most important feature.

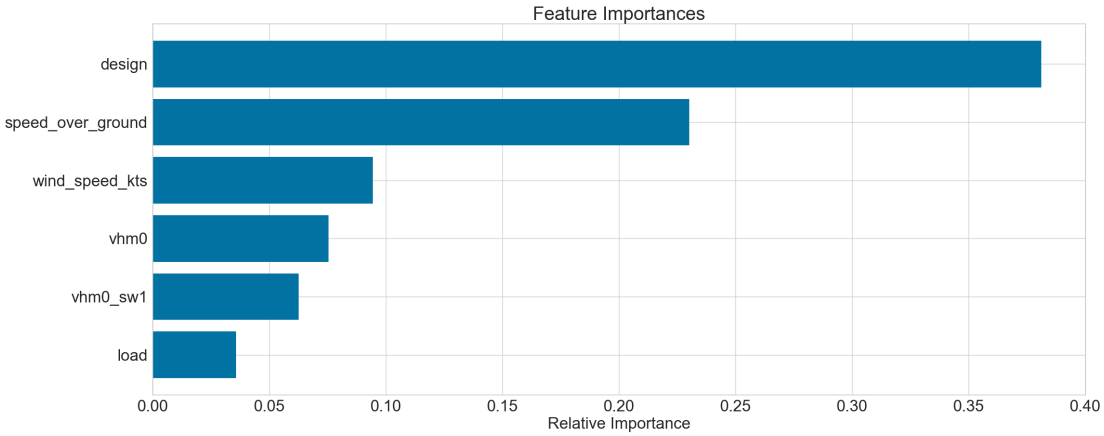

Figure 6.12: Graph of the top six feature importances

Furthermore, the horizontal barplot shows that "speed_over_ground" constitutes the second most important feature. This makes sense as the literature states that higher speeds increase fuel consumption. Moreover, it supports our findings that speed heavily influences consumption (Taskar and Andersen, 2020; Roh, 2013). In addition, Figure 6.12 states that the "wind_speed_kts" has approximately a 9 percent influence on the prediction.

6.3 Weather Routing Distributions - Fuel Consumption

6.3.1 Period December, January, and February

To compare the voyage's fuel consumption on the different routes, we made histograms of the utilization for each course for the divided periods. The following plots show how many tons of fuel a vessel consumed on average per voyage day. Considering the fuel consumption was predicted based on weather information, the difference can be explained by these climate seasonality observations captured in the descriptive statistics.

Starting with the three months of DJF, Figure 6.13 displays that the third route, to Mundra, consumes the least amount of fuel per day on its voyages. The plot was made using the random forest regression model to find the distribution of total voyage fuel consumption before dividing the result by the duration in days. A large portion of the route's fuel consumption is between 15 and 17 tons per day, making it a narrow distribution, which indicates a concentrated mode. Route 1, crossing the Atlantic Ocean, has a greater fluctuation in fuel consumption, displaying a left skewed distribution. This means that the average is lower than both the median and the mode. This route has a frequency, or a mode, of approximately 16 to 17 tons per day. Hence, resulting in the highest predicted fuel consumption of the three routes.

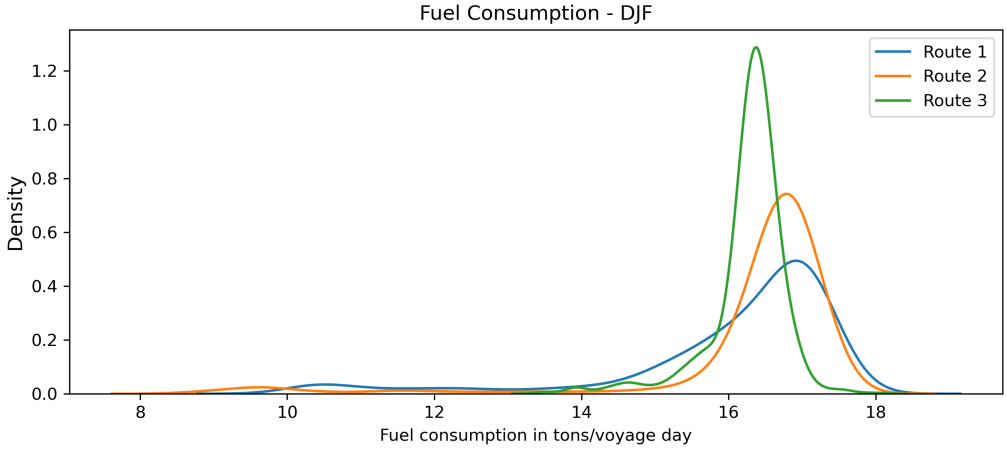

Figure 6.13: Total fuel consumption distributions on average per voyage day for the period DJF

The weather variables can explain the first route's variations and lower concentration

in fuel consumption. Considering the speed over ground in our thesis is fixed at 12.5 knots, the vessel has to use more fuel to uphold this speed. This is due to speed over ground decreasing when there is increased resistance caused by wind, waves, and currents (Almklov, 2022). As mentioned in the analysis, the North Atlantic Ocean for these months is affected by high waves, which can be observed in the maps presenting the wave height. These results align with the multiple extratropical storms occurring north in the ocean during this period. In addition, the wind speed in this period will also contribute to vessel resistance, as the mean wind speed ranges from 15 to 30 knots in large areas of the North Atlantic Ocean.

As for the South Atlantic Ocean, the values displayed on the maps show a considerably calmer sea, which corresponds to summer in the southern hemisphere. In this period, most of the area has waves that average in height from 2 to 3 meters. The wind speed is mostly between 10 to 15 knots.

The wind rose plots holding information on weather from locations in the route, corresponding to the information extracted from the weather data. For example, if the shipowner decides on route 1 in the months of DJF, the vessel may encounter wind with a speed corresponding to a tropical depression, which could refer to route coordinates north in the North Atlantic Ocean. Conversely, based on the maps and statistics, the section of calm wind could reflect the summer season in the South Atlantic Ocean.

The second route from Cape of Good Hope to Samarinda to Pipavav has a high fuel consumption per day, with a mode value of approximately 17 tons. In addition, the distribution is also left skewed indicating the median of the distribution is at a lower value than the mode. During the months of DJF, it is winter season in the Indian Ocean, and the maps indicate that the ocean is calm at this time of the year. The further north in the ocean, the lower the waves get. The maps demonstrate that the crossing from Cape of Good Hope to Samarinda in Indonesia has a mean wave height of approximately 2.5 meters. This route faces lower waves on average than the first route to Rotterdam. The wind is also weak for the period, with a mean below 15 knots.

Comparing the weather data to the wind rose plots for the route and the fuel consumption distribution, we see that the descriptive statistics contribute in explaining the result. The wind speed on the intended course has instances of values in the category 4 to 6 on the

Beaufort scale, although most of the wind is calm.

For the last route, from Cape of Good Hope to Richards Bay to Mundra, the fuel consumption is distributed with a mode at just above 16 tons on average per voyage day. From South Africa to Mundra, the vessel travels near the coast of East Africa and into the Arabic Sea. The maps of the mean wave height and wind speed in the Indian Ocean show that the ocean is very calm in these areas during the southern hemisphere's winter season. As a result, the waves reach only 1 to 1.5 meters on average or lower for most of the route. Furthermore, the wind speed averages between 5 and 15 knots, which illustrates considerably calm weather.

The dominating wind speed observed in Figure 6.9 of the wind rose plot is in the category 4 to 6 on the Beaufort scale, which implies balanced weather. This contributes to the explanation of why the average total voyage fuel consumption distribution has a concentrated mode.

6.3.2 Period March, April, and May

Next are the daily total voyage fuel consumption distributions for MAM. Figure 6.14 shows how the third route, on average, consumes the least amount of fuel. Likewise, the distributions for route 1 and route 3 are similar. However, route 1 is positioned slightly more to the right on the x-axis, indicating higher fuel consumption distribution values. Route 2, on the other hand, consumes more fuel on average.

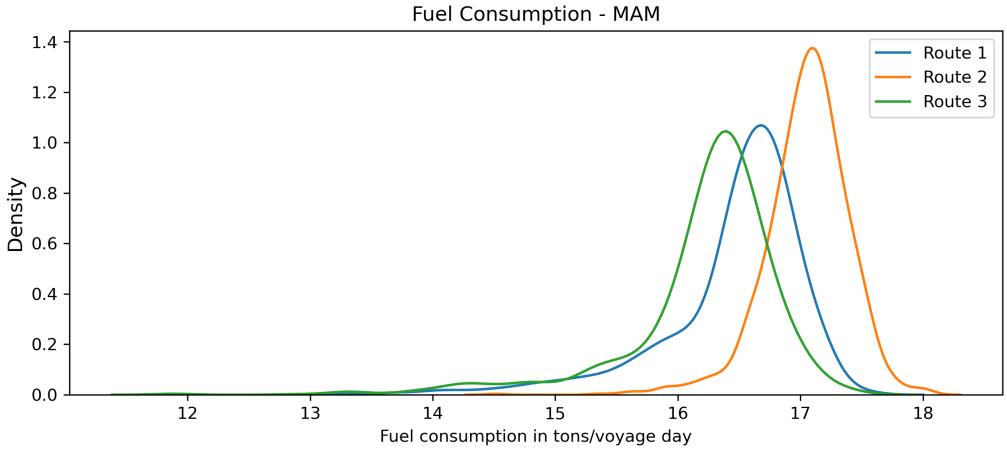

Figure 6.14: Total fuel consumption distributions on average per voyage day for the period MAM

For the first route to Rotterdam, the vessel travels across the South Atlantic Ocean during fall, MAM, and spring when crossing the North Atlantic Ocean because of the different season's definitions. The maps in Figure 6.1 and Figure 6.2 show that the North Atlantic Ocean is calmer in MAM than during the months of DJF, with a mean wind speed of between 10 to 20 knots. However, there are still considerably large waves further north, reaching approximately 4 meters. Nevertheless, the waves have been slightly increased for the South Atlantic Ocean. This is because waves are rising in height further north than before.

As for the wind rose plots in Figure 6.7, we can see that the wind speed encountered on the route has decreased considerably. This is because the months of MAM in the North Atlantic are less inclined to strong winter storms (Frame et al., 2017). In addition, the tropics are not inclined to have the ideal temperature for the creation of tropical storms (Shepherd, 2017).

Compared to the months of DJF, the fuel consumption has decreased slightly per day for a voyage. The distribution has become narrower and less right skewed than before. This can be a result of less volatile weather during the MAM months.

As for the second route to Pipavav, more fuel is consumed for the voyages, split into several days. The distribution has a left tail, indicating that the mean is slightly lower than the mode value. Even though the distribution has a longer left tail, there is a higher concentration of fuel consumption around the mode value.

Looking over the maps of the Indian Ocean, the number of higher waves has increased, but the wind speed has reduced in the northern part of the ocean. The southern part of the Indian Ocean has higher waves, gradually decreasing in height further north. The voyage route crosses the Indian Ocean on the way to Samarinda, in an area where the mean wave height is 3.5 meters. As for the wind speed, there are areas with wind reaching a mean of 25 knots, although this is not common.

The wind rose plots of the wind speed and direction in Figure 6.8 reflect the resulting fuel consumption distribution. For this route, the fuel consumption is higher compared to the two other routes, which is reasonable, seeing as this route has a higher number of observations of wind speed in the category 4 to 6.

For the fuel consumption distribution, there are rarely voyages reaching above 18 tons per day. In addition, the left tail has been considerably reduced, and there has become an increased frequency of values around the mode. This might be because of higher waves during MAM.

Route 3 to Mundra also has reduced weather compared to DJF. As seen on the maps, only the first part of the route has higher waves, whereas most of the course, in the Arabic Ocean, has a calm sea with, on average, approximately 1.5 meter high waves. The north part also has a much lower wind speed in knots compared to the months of DJF. The wind speed is, on average, 5 to 10 knots over the ocean near Mundra in India.

The wind rose plot in the period MAM can reflect these observations. Figure 6.9 shows that most of the wind registered has a speed of 3 to 6 on the Beaufort scale, which represent a calm ocean. Only a small percentage of the winds reach a speed, which equates to a tropical depression.

6.3.3 Period June, July, and August

Figure 6.15 displays the voyage fuel consumption distributions for the period JJA in tons on average per voyage day. For this period, route 1 has the lowest fuel consumption distribution values with a mode at approximately 16.5 tons. Route 3 has increased slightly from the previous periods and has a wider distribution, meaning the values are less concentrated. Hence, the fuel consumption varies in a greater degree compared to the other routes. The second route currently has the highest fuel consumption mode value at 17.5 tons on average.

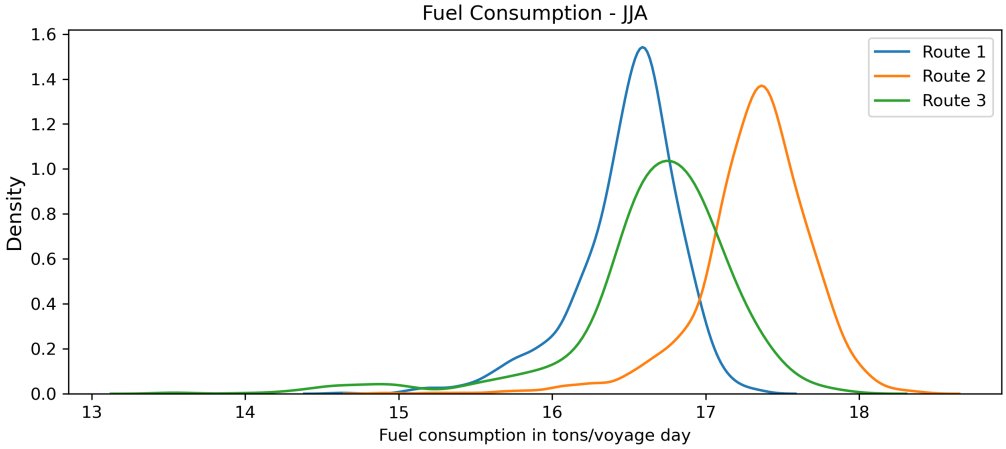

Figure 6.15: Total fuel consumption distributions on average per voyage day for the period JJA

Weather data can back the fuel consumption results of route 1. We can see that the waves have been reduced in height in the North Atlantic, with the map in Figure 6.1 showing most waves being no higher than 2.5 meters. The South Atlantic, on the other hand, has a higher mean wave height. Here, the number of high waves has stretched towards the north, leaving the vessel to travel through areas with higher average wave heights. In Figure 6.3, the map shows waves reaching an average of 4.5 meters up to the tip of Africa, and large amounts are within the 2.5 to 3 meters range. The North Atlantic has an average wind speed of 15 knots, with a good proportion of 5 to 10 knots. The South Atlantic has higher wind speed, but the areas concerning the routes have a mean of 15 to 20 knots.

The maps and the fuel consumption distribution can be proven further with the wind rose plots of the wave height and direction. For this period, there are a lot of waves reaching only up to 2 meters in height. There are, however, instances of waves from 3 to 4 meters.

The JJA period is calmer compared to DJF, however, quite similar to the MAM distribution and observations. As mentioned in the Section 3, it is not the season for extratropical storms in the North Atlantic, and the hurricane season has officially started. Nonetheless, most of these will happen in SON. The wind rose plots show a wave height reduction that remarkably reduces from DJF to MAM but also further to JJA. The period does have extratropical storms in the southern hemisphere, however, since this happens at a higher

latitude, the effects will diminish by the time it reaches the route coordinates.

Route 2, however, has a slightly higher fuel consumption with a mode of around 17.5 tons. The tail is long on the left side, but more voyages reach over 18 tons of consumption per day on average. This increase could be due to the monsoon season.

As we can see from Figure 6.5 and Figure 6.6 in the descriptive statistics, there are higher waves and wind speeds. The southern part of the ocean has the highest waves, which aligns with the data of the South Atlantic Ocean at this time due to the extratropical storms. Waves can reach an average of 5 meters, and large parts of the route will encounter areas with an average wave height of 3.5 to 4 meters. The wind speed has also increased in strength, mostly ranging from 15 to 20 knots. Near Samarinda, however, the ocean is calmer.

The impact of the monsoon season is also recognizable in the wind rose plot in Figure 6.8. Most wind speed encountered during route 2 can be placed within the category 4 and 6. However, there are also more wind reaching the speed of a tropical depression compared the first route, which could explain the more significant fuel consumption distribution.

Comparing the distributions, JJA now has higher waves, especially waves reaching 4 meters and above. Based on this, a voyage during this period would entail added extreme weather, possibly leading to higher fuel consumption.

For the last route to Mundra, the voyage fuel consumption distribution has also increased compared to the previous periods. The weather in JJA has resulted in a wider distribution for the route, and it no longer has the lowest consumption based on three case study routes. In addition, for this route, voyages reach a fuel consumption of approximately 18 tons, which rarely occurs.

The increase in fuel consumption shares the same explanation as route 2. Even though the area from Richards Bay to Mundra is relatively calm, JJA is more prone to higher waves. The wind speed has also increased, now with a mean value of 20 to 25 knots. According to the wind rose plots, the wind speed is mainly within the category 5 and 6, and in addition, has the most observations reaching the category of a tropical depression. The wind rose plots reveal a rougher sea for route 3 compared to route 2.

The observations of higher wind speed has increased significantly compared to the other

periods. The fuel consumption and the analyzed weather data show that the monsoon season is predisposed to the worst weather. This is especially evident due to the wide distribution of fuel consumption, indicating large variations for the fuel consumed during this period, resulting in more extreme values.

6.3.4 Period September, October, and November

Figure 6.16 shows the last period of the year, SON. These months are a part of the hurricane season in the North Atlantic Ocean (Kossin, 2008). From the graph, we see that it is route 2 that has the highest distribution values for fuel consumption on average per day, and route 3 requires the lowest amount of fuel. The first and the third routes are left skewed and have wide distributions. Route 2, though, has a distribution slightly more concentrated around the mode of just above 17 tons per day compared to the months JJA.

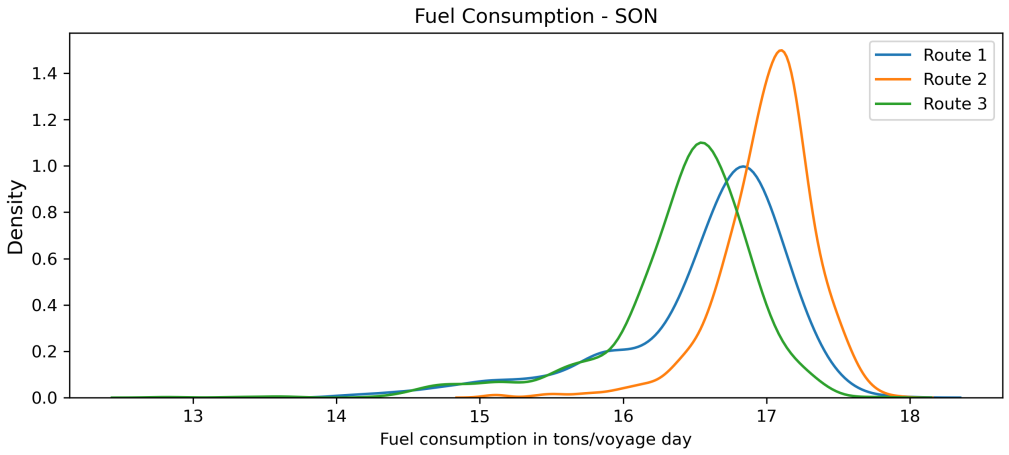

Figure 6.16: Total fuel consumption distributions on average per voyage day for the period SON

The first route, to Rotterdam, has a mode value at around 17 tons per day. This indicates that the fuel consumption is slightly reduced compared to DJF, with a wide distribution. From the part of the descriptive statistics, the map of the North Atlantic Ocean shows that the waves are reemerging. In addition, the wind speed is, on average, between 10 and 15 meters high over most of the North Atlantic, except for the northern part, which has a higher wind speed. The South Atlantic Ocean has spring at this time of the year, and,

according to the maps, the waves are still high with an average height of approximately 3 meters. The wind speed is also relatively strong, usually ranging from 10 to 20 knots.

The wind rose plot shows an increase in the wind speed for this period compared to JJA. Again, more wind are coming from the northwest and west, at the speed defined as a tropical depression. However, we have seen that the intensity will increase during the next period.

For route 2, the fuel consumption distribution has decreased compared to JJA. The mode value is slightly closer to 17 tons than the previous, and the distribution is narrower, meaning more observations is centered around the mode. This is a result of a reduced amount of turbulent weather.

From the descriptive statistics maps, the wave height has decreased across the Indian Ocean. This is because the periods for extratropical storms have passed, resulting in waves having a mean height of 3 to 3.5 meters for parts of the voyage route. In addition, wind speed has decreased in intensity. The wind rose plot in Figure 6.8 shows there have been observations of wind speed above category 6, though these are few. The wind speed met on the route is reduced compared to JJA.

The route to Mundra is the option that consumes the least fuel per voyage, with a mode at approximately 16.5 tons and a mean value lower than this. The distribution has a long left tail, although it is still narrower than the distribution from JJA. The descriptive statistics showing calmer weather helps explain this change in distribution.

The Indian Ocean is calmer during SON, and by looking at the map, we can see that the average wave height is low in the area for route 3. In addition, wind speed is between 10 to 15 knots on average for most parts of the route. This can be observed in the wind rose plot. While the average wave height is low, there are still registered waves over 5 meters, which could result from September originally being defined as part of the monsoon season.

Comparing the descriptive statistics, we can see that JJA is the period with the most volatile weather. This is reflected in the fuel consumption distribution, however, the period SON also shows several high waves compared to the winter and summer.

In Appendix C, the figures display the different fuel consumption distributions compared by routes, using total consumption. In addition, figures comparing the routes' fuel

consumption with periods are also included. These plots provide an average total fuel consumption of 600 tons for route 1 and route 2. Route 3, on the other hand, has an average of 300 tons. This is a result of the route to Mundra having a significantly shorter voyage.

6.4 Time Charter Equivalent Distributions

To analyze which route is the best option for a shipowner to accept for a vessel located in the Cape of Good Hope, it is beneficial to calculate the cumulative distribution of the TCE. This distribution is a decision tool for shipowners, where it is easy to see which option will give the best profit (Güngör and Barlas, 2022). We can compare the three routes for the different periods and case studies using these distributions. The cumulative plots show the likelihood of a shipowner gaining a certain value of TCE by what percentage the number is equal to on the y-axis. Based on this, we will choose the distribution leaning furthest towards the right as the best choice, representing a greater chance of gaining a higher profit. Following, we are able to finally decide which route is the best option for a shipowner.

In addition to these plots, Table D1 in the Appendix shows summary statistics values for each period and route for the first scenario of a low bunker price. In this table, we have included information about the mean and standard deviation of the distributions as well as the minimum and maximum values.

When predicting fuel consumption, we did not consider the effect of cargo weight. This is because the thesis contributes to the explanation of how fuel consumption is affected by weather variables, and adding this extra variable could have influenced the results. On the other hand, not including cargo weight as an input variable when predicting fuel consumption results in an incorrect TCE comparison. Therefore, even though route 3 regularly takes 60,000 tons of cargo, we have chosen to work with a fixed load of 50,000 tons (Clarksons Shipping Intelligence Network, 2022). Appendix D, Figure D.4 show the resulting TCE distribution for route 3 for all periods. In addition, Figure D.5 to Figure D.8 display the cumulative plots comparing the three case study routes when using 60,000 tons of cargo for route 3.

6.4.1 Period December, January, and February

The time charter equivalent distributions are derived from the resulting fuel consumption distributions, and we analyzed the route options for each period and each scenario. Figure 6.17 shows the results for period DJF where route 3 has the distribution with the highest TCE values for scenario 1. This result is reflected in Table D.1, listing the mean value for this route at 19,929.50$. Route 1 is the second best option for the low bunker scenario, as seen in the figure, with the second route achieving the lowest TCE. Every graph in this scenario is slightly right skewed, indicating that the highest frequency has a lower value than the mean. This is a result of missing days for some voyages, corresponding with the low fuel consumption on average per day for some of the routes in this period.

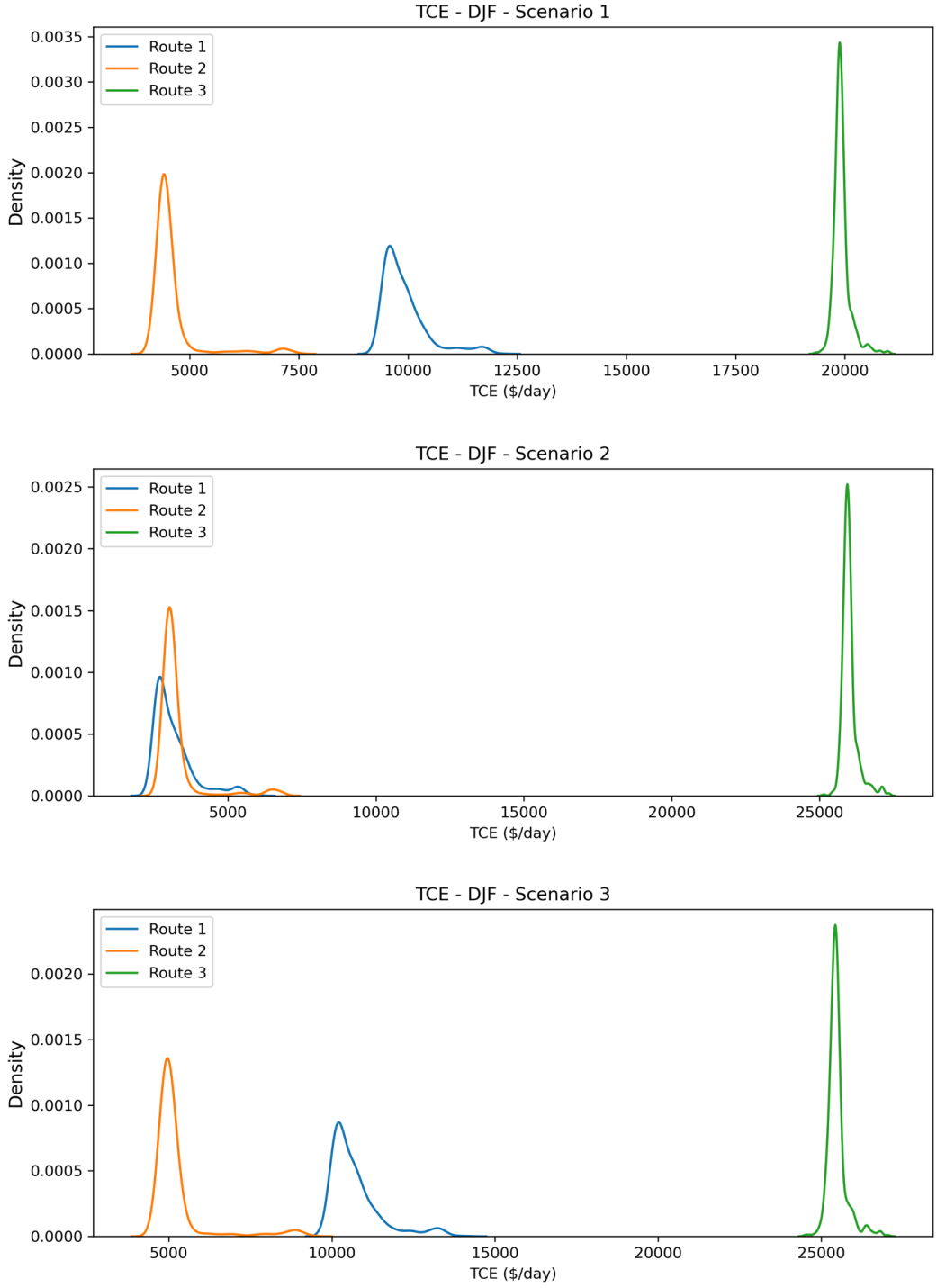

Figure 6.17: TCE distributions for the months December, January, and February, for all three scenarios

For routes 1 and 2, the TCE distributions are different for the second scenario with an average fuel bunker price. Route 1 has a reduced value at the point of the highest frequency, and the third route is even more profitable. Because of a higher bunker price,

the first and second routes have decreased TCE values. This decline is also a result of a corresponding lower freight rate for route 1 along with a barely increasing rate for route 2. For the third route, however, the scenario had a more significant increase in freight rate, resulting in higher TCE. Accordingly, scenario 3, with high bunker prices, leads to an increasing distribution of TCE values for the first and second routes, whereas route 3 has slightly decreased.

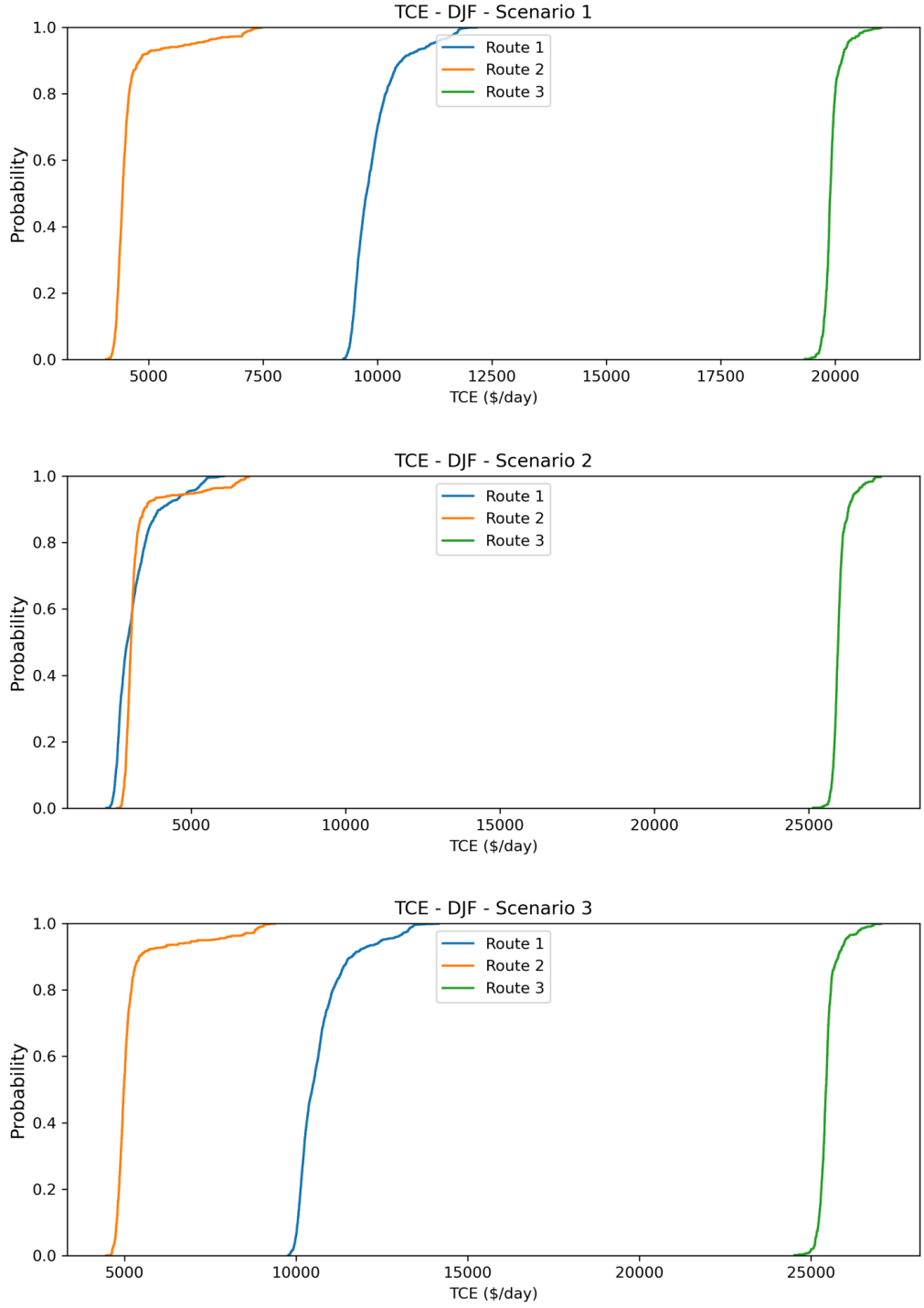

Figure 6.18: Cumulative TCE distributions for the months December, January, and February, for all three scenarios

The cumulative plot in Figure 6.18 shows that the third route is the best option for the shipowner. This is the distribution furthest to the right, meaning it has a greater chance of earning higher profits.

From what we can gather from the results, fuel consumption shows that weather affects the consumption significantly for route 1 to Rotterdam because of the crossing of the North Atlantic Ocean during DJF. Therefore, the fuel consumption distribution for this route is wider than for route 2 and route 3. Comparing the cumulative distributions, the route to Mundra has approximately 80 percent chance of earning a TCE of less than 20,000$, though never less than 19,257.80$, which is the minimum value in Table D1. On the other hand, for route 1, 70 percent of the time, TCE will be less than 10,000$, with the highest possible value of 10,786.50$. As the route to Mundra has the lowest fuel consumption on average and is more profitable, with the best cumulative TCE distribution, it is the best route option during DJF.

6.4.2 Period March, April, and May

Figure 6.19 displays the TCE distribution results for period MAM. Comparing each of the scenarios, route 3 is still the most profitable choice when the bunker price is low. For this scenario, the mean is 19,951.30$, slightly higher than the previous, although the distribution is still right skewed. This result is higher than the distributions for route 1 and 2, which remains approximately the same compared to DJF. The only difference is narrower distributions, which could result from less volatile weather. As seen in Table D1, the minimum TCE value attainable for route 2 is 3,931.97$, with a maximum of 4,853.84$. Along with the plot comparing the routes for scenario 1, we see that the least profitable option is route 2 due to considerably lower values.

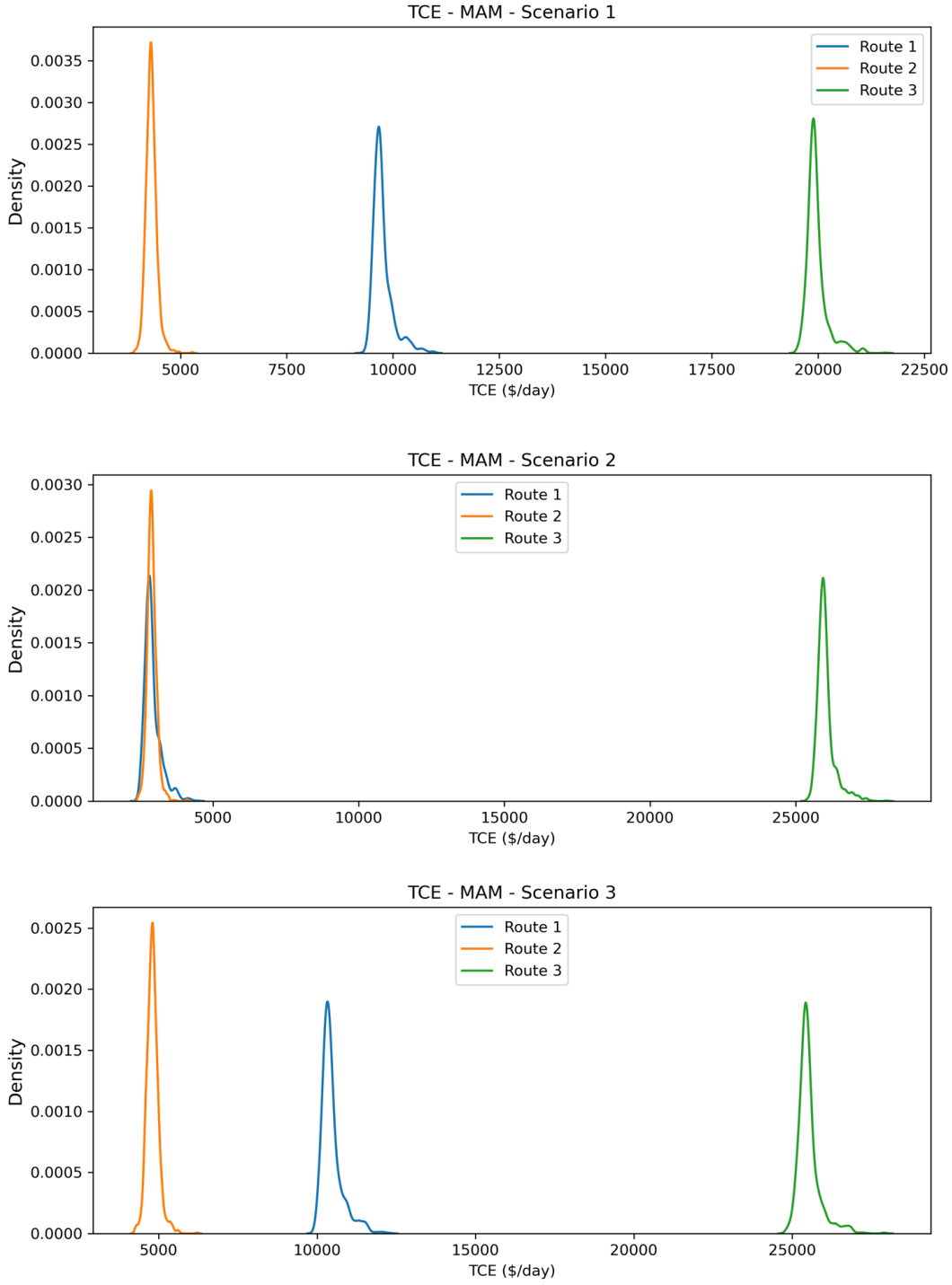

Figure 6.19: TCE distributions for the months March, April, and May, for all three scenarios

For the second scenario, the mean bunker price, Figure 6.19, shows decreased TCE values for the distribution for route 1, with approximately the same values on the x-axis as route 2. These results could be due to the significantly reduced freight rate for route 1 during

the second scenario, which greatly reduces the TCE. On the other hand, route 3 has a considerable increase in freight rate, making the route more profitable even though the bunker prices have increased. Scenario 3 shows increased TCE values for the distribution of route 1 compared to the mean bunker price.

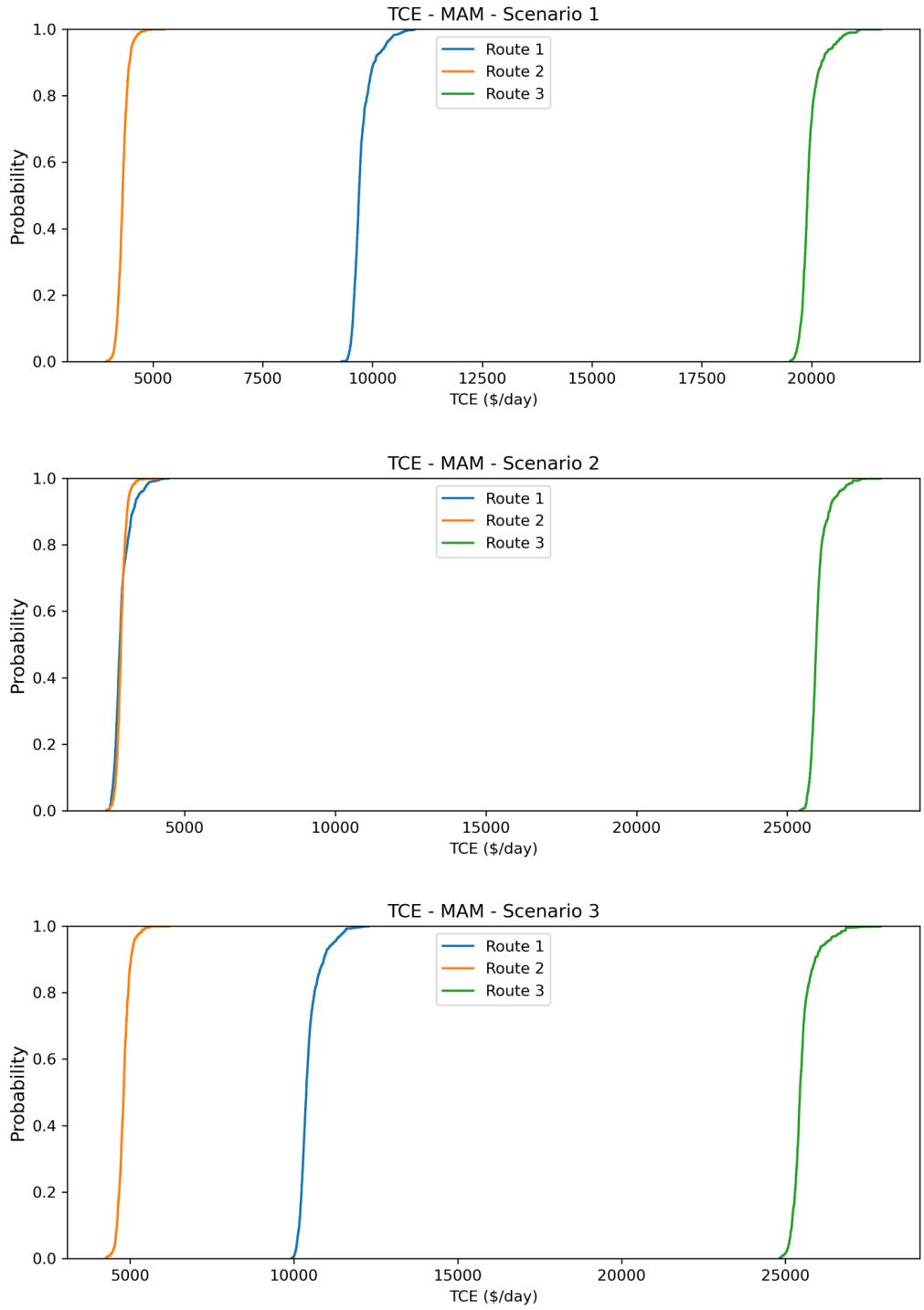

Figure 6.20: Cumulative TCE distributions for the months March, April, and May, for all three scenarios

Considering the weather was calmer during MAM, we have a greater likelihood of gaining a profit around the mean value because of the narrower distributions. The cumulative distributions in Figure 6.20 show the three different scenarios. The distributions are somewhat similar, with the third route being the best option for all scenarios in MAM. The second-best option is the first route, even in the second scenario. As seen in the plot, route 1 crosses the cumulative distribution of route 2, indicating it has broader tails. It is also positioned slightly further to the right and, as a result, has a better probability of earning higher TCE than route 2.

6.4.3 Period June, July, and August

For the period JJA, Figure 6.21 show that the TCE values in the distribution for route 3 have decreased due to the monsoon season causing more weather events in the Indian Ocean. The mean value for this route is, for this period, 19,780.20$. In addition, for scenario 1, the distribution for route 1 has become narrower, now with a mean of 9,735.91$ and a decreased standard deviation at the value of 125.62$.

For the second scenario, route 1 gains higher distribution values compared to route 2, even though the freight rate has significantly decreased. This supports the fact that JJA is the monsoon season in the Indian Ocean, creating worse weather for the route to Samarinda and Pipavav, equating to the summer season in the North Atlantic Ocean. As previously concluded, the North Atlantic had calmer weather during this period. For the third scenario, route 3 has a wider distribution and has slightly decreased values compared to the second scenario. The most frequent observed value is now just above 25,000$.

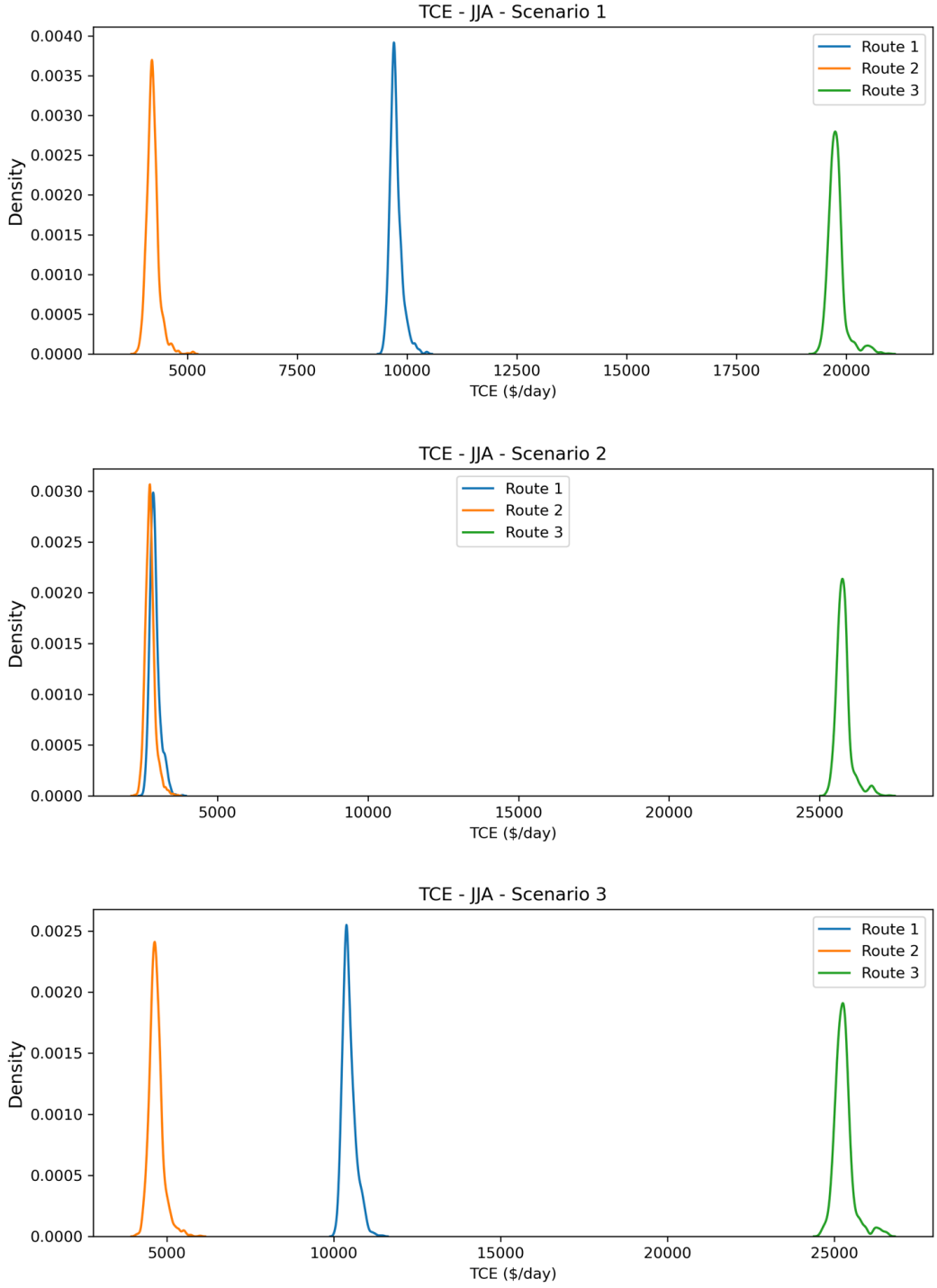

Figure 6.21: TCE distributions for the months June, July, and August, for all three scenarios

The cumulative distributions displayed in Figure 6.22 shows that route 3 to Mundra is still the best option, supporting the resulting TCE distributions. For the first scenario, the third route has over 90% chance of earning below 20,000$, however, it is not likely

to make less than the minimum value of 19,313.7$, which is considerably more than the other routes. For scenario 2, the first route has a higher probability of earning a higher TCE compared to route 2. Nevertheless, even though the first route is positioned more to the right, the cumulative distribution of route 2 is slightly more bent, showing route 2 has the opportunity of earning more than route 1 due to a longer right tail. Even though the opportunity of earning a higher TCE is present, there is still a considerably higher risk of choosing this route than the route crossing the Atlantic Ocean. To conclude, the third route is the best option for a shipowner to choose during JJA, regardless of the different scenarios, despite the increased likelihood of experiencing harsh weather during this period.

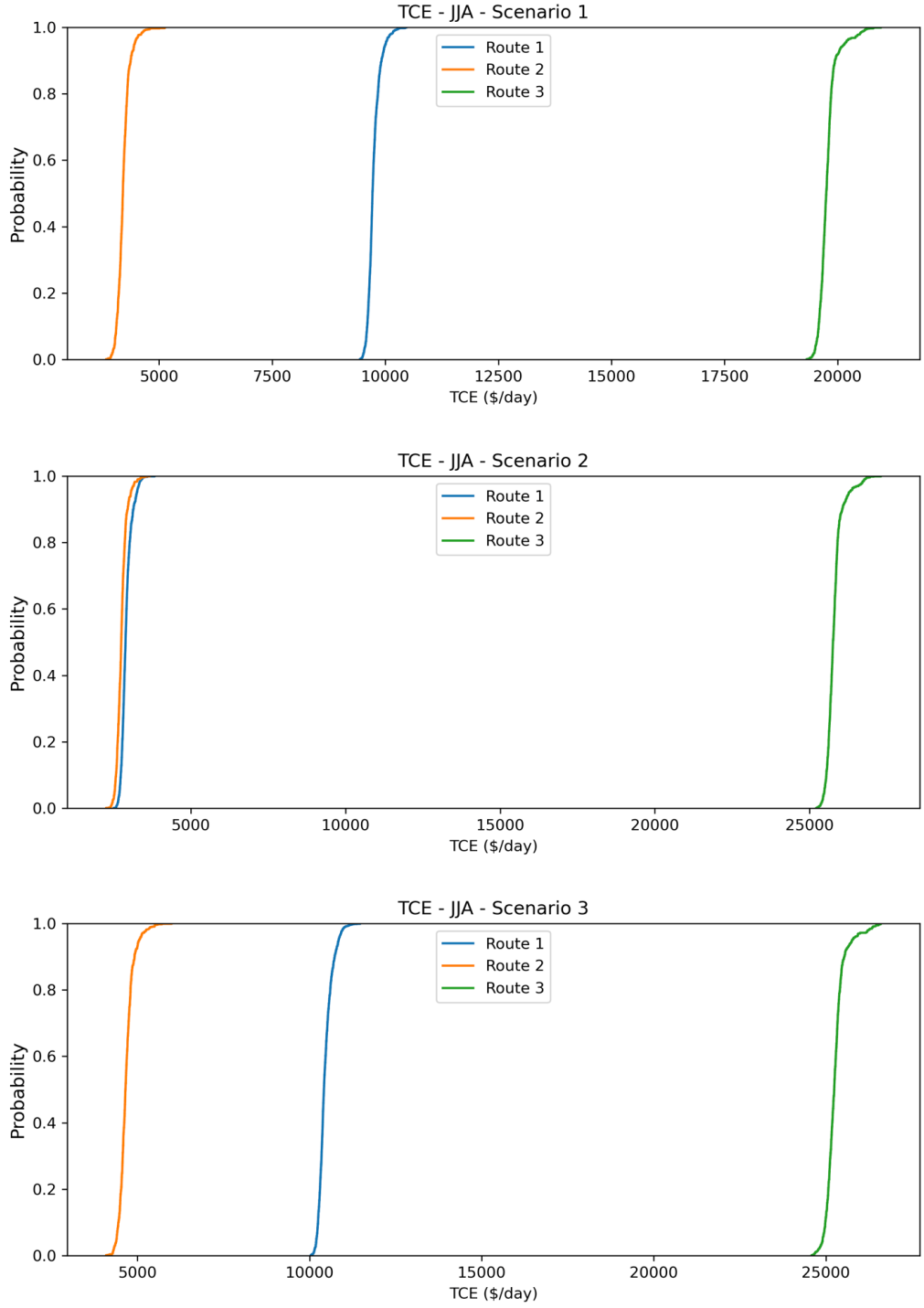

Figure 6.22: Cumulative TCE distributions for the months June, July, and August, for all three scenarios

6.4.4 Period September, October, and November

In Figure 6.23, Route 3 has again the distribution furthest to the right with the highest TCE values. The mean value for this distribution has increased to a value of 19,887.40$

compared to JJA due to the monsoon season passing. The figure also displays a wider distribution for route 1, which can be an effect of the seasonal climate for the period. For this route in SON, the mean value earned is 9,698.56$ per day as observed on the plot in Figure 6.24, resulting in a higher mean value than the most frequent TCE. The distribution for route 2, however, is still quite narrow. For the second scenario, the distribution for route 1 has again decreased values. For the third scenario, of the high bunker prices, every route has increased distribution values due to the freight rates gathered at the time of the bunker price scenario.

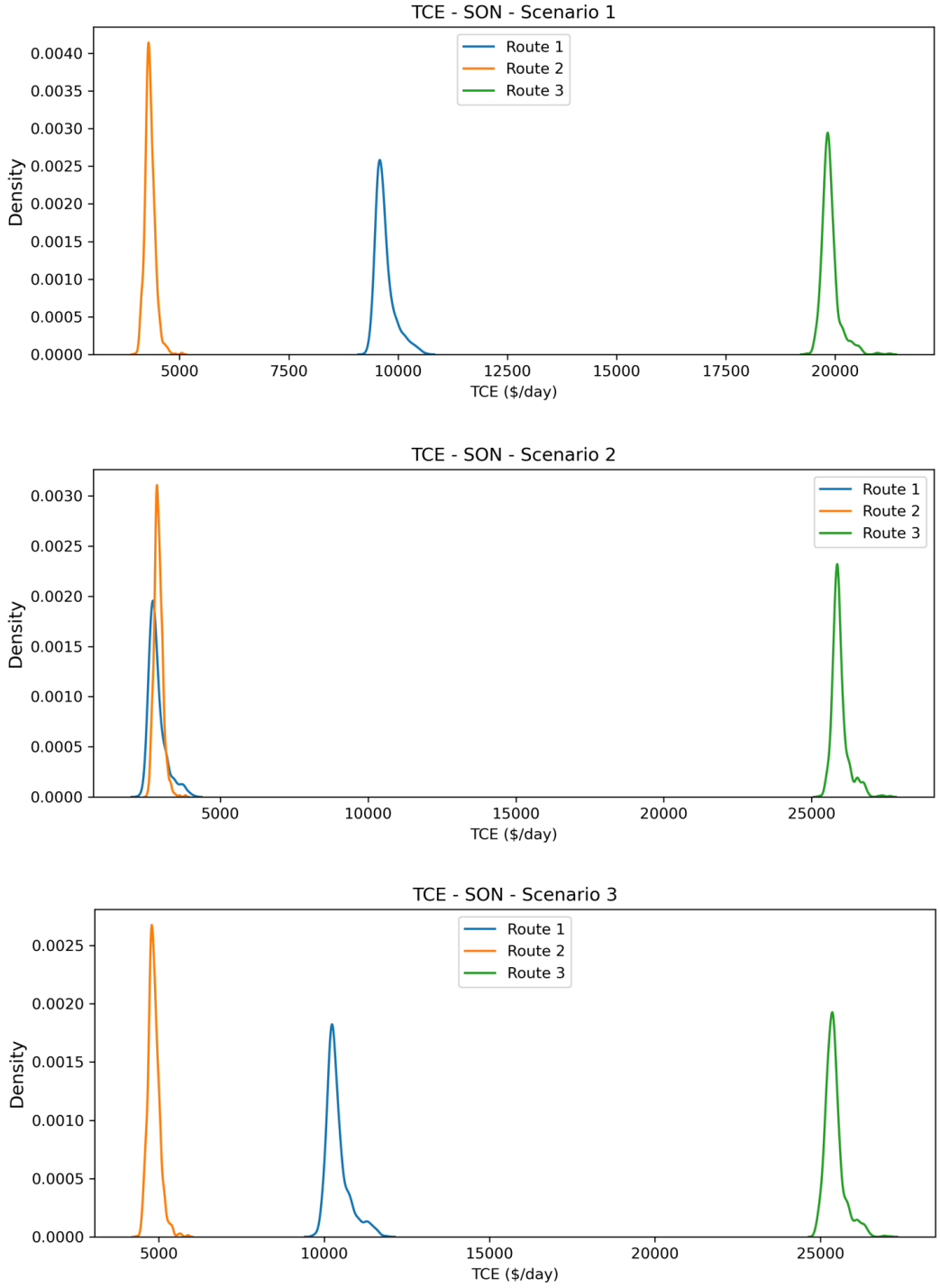

Figure 6.23: TCE distributions for the months September, October, and November, for all three scenarios

The cumulative plots in Figure 6.24 show that route 3 is the most profitable choice in the period of SON, with a placement furthest to the right of the x-axis for every scenario. Route 1, on the other hand, has a high probability of earning less than 10,000$ per day.

Scenario 2 shows that route 2 has a higher probability of earning more compared to route 1, seeing as the distribution for the route to Pipavav is placed more to the right. This shows that route 1 has a wider distribution, with more chance of earning less, however, there is still a possibility of earning more than route 2, though this chance is slim. This result could be due to the hurricane season in the North Atlantic Ocean as well as extratropical storms starting to occur later in this period. The third scenario of a high bunker price shows that there is now a high probability of a TCE higher than 10,000$ when choosing route 1, as well as a high probability of gaining a TCE of more than 25,000$ when choosing the third route. To conclude, the route from the Cape of Good Hope to Richards Bay to Mundra is the preferred route for all scenarios in this period.

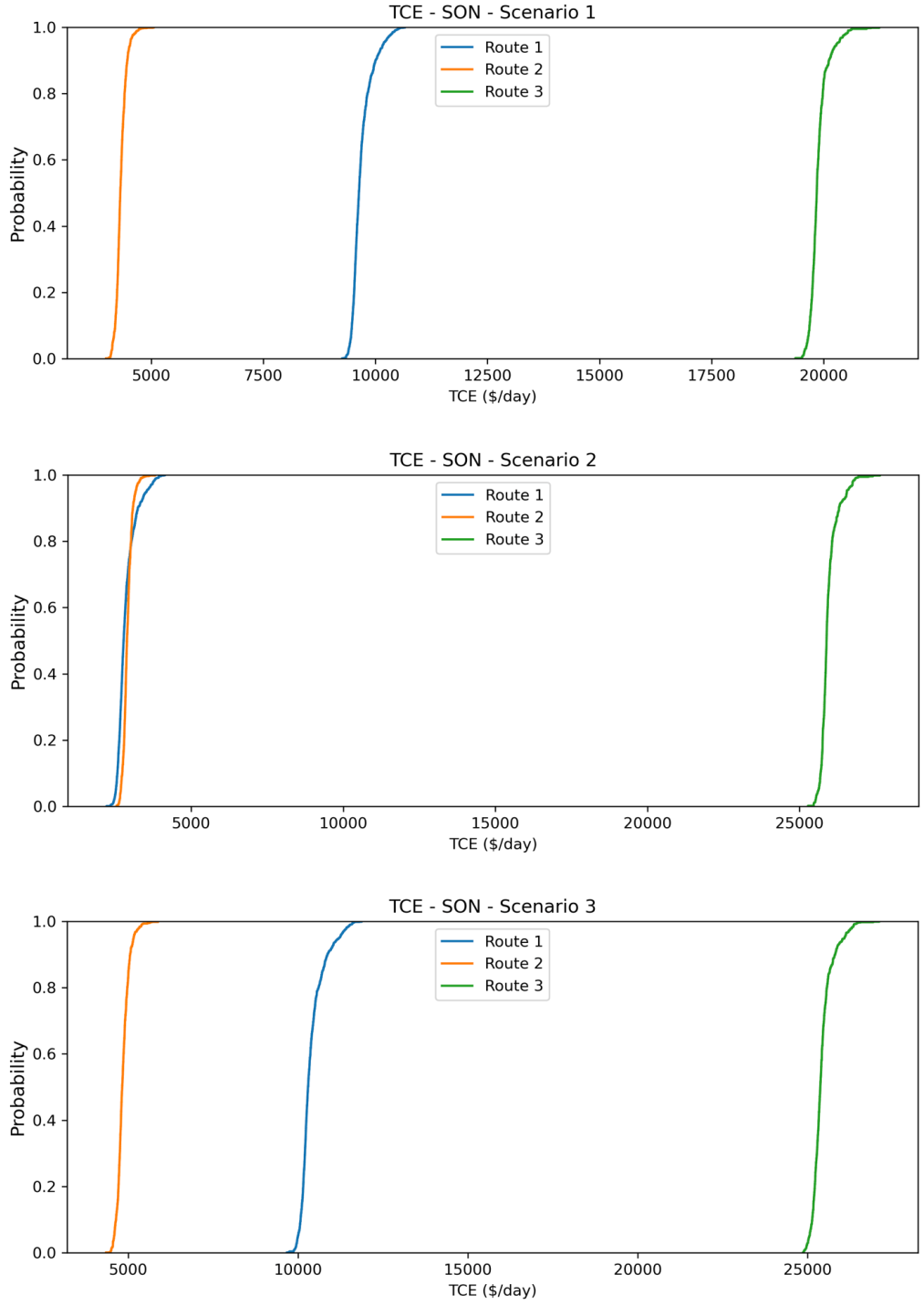

Figure 6.24: Cumulative TCE distributions for the months September, October, and November, for all three scenarios

7 Final Remarks

7.1 Conclusion

Our thesis presents three contributions to the field of shipping, where we generate TCE and an assessment of climate risk. The first contribution is a method for generating distributions of TCEs using climate information as input, providing a more comprehensive way to assess risk than the deterministic approach using a fixed weather margin. The second contribution is a comparison of different routes for a Supramax vessel trading to key ports based on climate seasonality. Finally, the third and last contribution is a business-oriented analysis of the case of a vessel open for cargo at the Cape of Good Hope.

To understand how weather conditions, such as strong winds and waves, impact fuel consumption and TCE for vessels at sea, we retrieved wind, waves, and swell data from the Copernicus Marine Service (2022). In addition, to understand the seasonal variations in fuel consumption for the different routes, we used machine learning to predict the best-fitting model, which was the Random Forest.

Moreover, we made distributions to compare the fuel consumption of different routes for four periods of the year. Furthermore, the distributions show that the routes with the lowest fuel consumption per day are the ones encountering the lowest wave height and wind speeds, as these weather conditions contribute to vessel resistance and therefore increase fuel consumption.

As a result, this research analyzes the best route options for a shipowner based on the Time Charter Equivalent distributions. The distributions are further used to compare the likelihood of higher TCE. The optimal route is the one going from the Cape of Good Hope to Richards Bay to Mundra due to the lowest fuel consumption and the overall best weather conditions. The results also show that the weather significantly affects fuel consumption and TCE. Hence, taking these factors into account can help shipowners make more profitable decisions.

Based on the findings of this research, we recommend using the method proposed in this thesis for generating distributions of TCEs where climate information is utilized as input to assess better weather-related risks and their effects on fuel consumption and

TCE. Furthermore, it should be considered to use machine learning models, such as the Random Forest, to predict fuel consumption and optimize route planning based on weather conditions. Moreover, seasonal weather variations and their effects on fuel consumption in the decision-making process should be evaluated. Lastly, we recommend using TCE distributions to compare the likelihood of increasing profits for different routes and choose the one with the lowest fuel consumption and the best weather conditions.

By following these recommendations, shipowners can improve their ability to forecast and manage weather-related risks and make more profitable decisions.

7.2 Limitations

After interpolating and connecting the weather data to the routes, the compiled data had missing rows for the last part of December, every two years. Instead of having data for each day, these voyages ended on January 15th, generating an incorrect number of days on the trips. This causes a limitation to the total fuel consumption in December, January, and February. In Appendix C, Figures C.1 to Figure C3, show the graph having a long left tail, indicating an unnaturally low total fuel consumption average per voyage day. By making every voyage last an equal number of days, the result of fuel consumption and TCE would become more accurate.

Another limitation of our thesis is that we have based the three routes on the shortest distance between the ports. These routes might not always be the best option. For instance, there could be shallow waters, and sometimes a vessel needs to choose a longer route to avoid encountering dangerous weather conditions. We have also yet to consider the possibility that the ship needs to spend more days on a voyage due to bad weather, which could increase expenses significantly. For instance, as mentioned in the analysis of the observed weather statistics, waves have been recorded reaching up to 13 to 17 meters, and wind speeds have been measured to equal a tropical storm or hurricane. These are examples of extreme weather events that could change the planned voyage for a vessel.

7.3 Further Research

For further research, it would be interesting to use less fixed variables as this might debilitate the generalizability of the findings, as the result might not be applicable for other vessels, different cargo weights, or different speeds over ground. Also, in regards to the best route, based on our findings, it might be different if other aspects were evaluated rather than solely basing the entire analysis on costs. This is because it may exclude important factors, such as safety and environmental impacts, and such assessments could further improve the validity of the conclusion.

Moreover, the limitations described above, highlight important considerations for further research that could positively affect the accuracy and robustness of the findings. The missing data for certain routes during DJF every two years could introduce a bias in the results, as it may not accurately reflect the true fuel- and TCE distributions. Additionally, the assumption that the shortest distance between ports is always the best route may not always hold true, as there may be other factors, such as shallow waters and dangerous weather conditions, that could impact the optimal route. Finally, the possibility that extreme weather events could extend the length of a voyage and increase expenses has not been taken into account in the analysis, which could affect the conclusions.

References

Alizadeh, A. and Nomikos, N. (2009). *Shipping Derivatives and Risk Management*. Palgrave Macmillan. doi: 10.1057/9780230235809.

Almklov, D. V. (2022). Trans-arctic re-routing of container vessels using the mariteam model: A comparative analysis of short- and long-term climate change impacts. Master's thesis, NTNU.

Amanatides, J. and Woo, A. (1987). A fast voxel traversal algorithm for ray tracing. *Proceedings of EuroGraphics*, 87. doi: 10.2312/EGTP.19871000.

Armstrong, V. (2013). Vessel optimisation for low carbon shipping. *Ocean Engineering*, 73:195–207. doi: 10.1016/j.oceaneng.2013.06.018.

Ballou, P., Chen, H., and Horner, J. D. (2008). Advanced methods of optimizing ship operations to reduce emissions detrimental to climate change. In *OCEANS 2008*, pages 1–12. doi: 10.1109/OCEANS.2008.5151815.

Barton, R. and Schruben, L. (2001). Resampling methods for input modeling. In *Winter Simulation Conference Proceedings*, volume 1, pages 372–378. doi: 10.1109/WSC.2001.977303.

Bengtsson, L., Hodges, K., and Keenlyside, N. (2009). Will extratropical storms intensify in a warmer climate? *Journal of Climate*, 22. doi: 10.1175/2008JCLI2678.1.

Biau, G. (2010). Analysis of a random forests model. *Journal of Machine Learning Research*, 13:1063–1095. doi: 10.48550/ARXIV.1005.0208.

Brummelen, G. V. (2021). *The Doctrine of Triangles: A History of Modern Trigonometry*. Princeton University Press.

Catto, J. L., Jakob, C., Berry, G. J., and Nicholls, N. (2012). Relating global precipitation to atmospheric fronts. *Geophysical Research Letters*, 39. doi: 10.1029/2012GL051736.

Clarksons Shipping Intelligence Network (2022). https://sin.clarksons.net/. Accessed: 2022-11-16.

Copernicus Marine Service (2019). *Global Ocean Wind L4 Reprocessed 6 hourly Observations*. https://data.marine.copernicus.eu/product/WIND_GLO_WIND_L4_REP_OBSERVATIONS_012_006/description. Accessed: 2022-09-26.

Copernicus Marine Service (2021). *Global Ocean Waves Reanalysis WAVERYS*. https://data.marine.copernicus.eu/product/GLOBAL_MULTIYEAR_WAV_001_032/description. Accessed: 2022-09-22.

Copernicus Marine Service (2022). *Copernicus Marine Data Store*. https://data.marine.copernicus.eu/products. Accessed: 2022-09-01.

Cosenza, B. (2008). A Survey on Exploiting Grids for Ray Tracing. In Scarano, V., Chiara, R. D., and Erra, U., editors, *Eurographics Italian Chapter Conference*. The Eurographics Association. doi: 10.2312/LocalChapterEvents/ItalChap/ItalianChapConf2008/089-096.

Cutler, A., Cutler, D. R., and Stevens, J. R. (2012). *Random Forests*, pages 157–175. Springer US, Boston, MA. doi: 10.1007/978-1-4419-9326-7$_5$.

Dataloy (2022). *Dataloy Distance Table*. https://ddt.dataloy.com/#/?speed=12.5&start=1671469020534. Accessed: 2022-09-21.

Dtn (2021). *How to Reduce Fuel Consumption with Weather Routing*. https://www.dtn.com/wp-content/uploads/2021/03/reduce-fuel-consumption-with-weather-routing.pdf. Accessed: 2022-10-05.

Elsner, J., Elsner, T., and Kara, A. (1999). *Hurricanes of the North Atlantic: Climate and Society*. Oxford University Press.

Emanuel, K. (2003). Tropical cyclones. *Annual Review of Earth and Planetary Sciences*, 31(1):75–104. doi: https://doi.org/10.1146/annurev.earth.31.100901.141259.

Frame, T. H. A., Harrison, G., Hewson, T., and Roberts, N. M. (2017). Meteorological risk: extra-tropical cyclones, tropical cyclones and convective storms.

Gade, K. (2010). A non-singular horizontal position representation. *Journal of Navigation*, 63:395 – 417. doi: 10.1017/S0373463309990415.

Gholamy, A., Kreinovich, V., and Kosheleva, O. (2018). Why 70/30 or 80/20 relation between training and testing sets: A pedagogical explanation.

Gozzo, L. F., da Rocha, R. P., Reboita, M. S., and Sugahara, S. (2014). Subtropical cyclones over the southwestern south atlantic: Climatological aspects and case study. *Journal of Climate*, 27(22):8543 – 8562. doi: 10.1175/JCLI-D-14-00149.1.

Güngör, A. and Barlas, B. (2022). Decision-making under risk: A ship sale and purchase problem by utilizing cumulative prospect theory. *Journal of ETA Maritime Science*, 10:16–28. doi: 10.4274/jems.2021.01488.

Hartanto, S., Furqan, M., Siahaan, A. P. U., and Fitriani, W. (2017). Haversine method in looking for the nearest masjid. *International Journal of Engineering Research*, 3:187–195. doi: 10.23883/IJRTER.2017.3402.PD61H.

Hayes, A. (2021). *Time Charter Equivalent (TCE)*. https://www.investopedia.com/terms/t/time-charter-equivalent-tce.asp. Accessed: 2022-10-10.

Ikasari, D., Widiastuti, and Andika, R. (2021). Determine the shortest path problem using haversine algorithm, a case study of sma zoning in depok. In *2021 3rd International Congress on Human-Computer Interaction, Optimization and Robotic Applications (HORA)*, pages 1–6. doi: 10.1109/HORA52670.2021.9461185.

James, G., Witten, D., Hastie, T., and Tibshirani, R. (2021). *An introduction to statistical learning*, volume 112. 2nd edition.

Joblib (2021). *Joblib: running Python functions as pipeline jobs*. https://joblib.readthedocs.io/en/latest/. Accessed: 2022-11-18.

Johansson, A. and Bolin, K. (2019). Understanding loudness variations for aircraft landing procedures at arlanda (ulla). In *Proceedings of the 10th Aerospace Technology Congress*, pages 93–98. doi: 10.3384/ecp19162010.

Kavussanos, M., Tsouknidis, D., and Visvikis, I. (2021). *Freight Derivatives and Risk Management in Shipping*. Routledge, 2nd edition. doi: 10.4324/9780429343681.

Korn, G. A. and Korn, T. M. (2000). *Mathematical Handbook for Scientists and Engineers - Definitions, Theorems, and Formulas for Reference and Review*. Dover Publications, 2nd edition.

Kosmas, O. and Vlachos, D. (2012). Simulated annealing for optimal ship routing. *Computers Operations Research*, 39(3):576–581. doi: 10.1016/j.cor.2011.05.010.

Kossin, J. (2008). Is the north atlantic hurricane season getting longer? *Geophysical Research Letters*, 35:119–129. doi: 10.1029/2008GL036012.

Krishna, M. K. (2009). Intensifying tropical cyclones over the north indian ocean during summer monsoon—global warming. *Global and Planetary Change*, 65(1):12–16. doi: 10.1016/j.gloplacha.2008.10.007.

Latif, M., Dommenget, D., Dima, M., and Grötzner, A. (1999). The role of indian ocean sea surface temperature in forcing east african rainfall anomalies during december–january 1997/98. *Journal of Climate*, 12(12):3497 – 3504. doi: 10.1175/1520-0442(1999)012<3497:TROIOS>2.0.CO;2.

Lee, D. Y., Peterson, M. R., and Lin, W. (2019). The southern annular mode and southern ocean surface westerly winds in e3sm. *Earth and Space Science*, 6(12):2624–2643. doi: 10.1029/2019EA000663.

Lindstad, H., Asbjørnslett, B. E., and Jullumstrø, E. (2013). Assessment of profit, cost and emissions by varying speed as a function of sea conditions and freight market. *Transportation Research Part D: Transport and Environment*, 19:5–12. doi: 10.1016/j.trd.2012.11.001.

Magnussen, A. K. (2017). Rational calculation of sea margin. Master's thesis, Norwegian University of Science and Technology.

Marklund, J. and Laguna, M. (2018). *Business Process Modeling, Simulation and Design 3rd Edition*. Taylor Francis, United Kingdom, 3rd edition.

Menon, A. (2021). *What Are Supramax Cargo Vessels?* https://www.marineinsight.com/types-of-ships/what-are-supramax-cargo-vessels/. Accessed: 2022-12-09.

Nilsson, J. and Nilsson, M. (2021). Estimating weather margin seasonality in shipping using machine learning. Master's thesis, Norwegian School of Economics.

Norlund, E. K. and Gribkovskaia, I. (2017). *Environmental performance of speed optimization strategies in offshore supply vessel planning under weather uncertainty. Transportation Research Part D: Transport and Environment*, 57:10–22. doi: 10.1016/j.trd.2017.08.002).

Panayides, P. M. (2018). *Principles of Chartering: Third Edition*. CreateSpace Independent Publishing Platform, 3rd edition.

Perlewitz, P. (1936). The wind according to the "beaufort" scale and its velocity. *International Hydrographic Review*.

Phillips, H., Tandon, A., Furue, R., Hood, R., Ummenhofer, C., Benthuysen, J., Menezes, V., Hu, S., Webber, B., Sanchez-Franks, A., Cherian, D., Shroyer, E., Feng, M., Wijeskera,

H., Chatterjee, A., Yu, L., Hermes, J., Murtugudde, R., Tozuka, T., and Wiggert, J. (2021). Progress in understanding of indian ocean circulation, variability, air-sea exchange and impacts on biogeochemistry. 17:1–109. doi: 10.5194/os-2021-1.

Plomaritou, E. and Papadopoulos, A. (2017). *Shipbroking and Chartering Practice*. Lloyd's Practical Shipping Guides. Taylor & Francis, 8th edition.

Pulagam, S. (2020). *Feature Scaling — Effectively Choose Input Variables Based on Distributions*. https://towardsdatascience.com/feature-scaling-effectively-choose-input-variables-based-on-distributions-3032207c921f. Accessed: 2022-12-18.

Ramos, M. S., Farina, L., Faria, S. H., and Li, C. (2021). Relationships between large-scale climate modes and the south atlantic ocean wave climate. *Progress in Oceanography*, 197:102660. doi: 10.1016/j.pocean.2021.102660.

Rehmatulla, N. and Smith, T. (2015). Barriers to energy efficiency in shipping: A triangulated approach to investigate the principal agent problem. *Energy Policy*, 84:44–57. doi: 10.1016/j.enpol.2015.04.019.

Roh, M.-I. (2013). Determination of an economical shipping route considering the effects of sea state for lower fuel consumption. *International Journal of Naval Architecture and Ocean Engineering*, 5(2):246–262. doi: 10.3744/JNAOE.2013.5.2.246.

Ronen, D. (2011). The effect of oil price on containership speed and fleet size. *JORS*, 62:211–216. doi: 10.1057/jors.2009.169.

Roux, F. (2022). *Monsoons*. https://www.encyclopedie-environnement.org/en/air-en/monsoons/. Accessed: 2022-11-23.

Semedo, A., Sušelj, K., and Rutgersson, A. (2008). Variability of wind sea and swell waves in the north atlantic based on era-40 re-analysis. In *8th European Wave and Tidal Energy Conference*.

Shanker, A. and Kelton, W. (1991). Empirical input distributions: an alternative to standard input distributions in simulation modeling. In *1991 Winter Simulation Conference Proceedings.*, pages 978–985. doi: 10.1109/WSC.1991.185713.

Shepherd, M. (2017). *Why Atlantic Hurricanes Don't Form In Winter And Spring (Or Do They?)*. https://www.forbes.com/sites/marshallshepherd/2017/11/05/why-atlantic-hurricanes-dont-form-in-winter-and-spring-or-do-they/?sh=700b7b5a28ba&fbclid=IwAR1NpRDPGsNn6HspbF9r0yYJBY-HUx1gCFqocayqf7J098mrECn_vn8qJLs. Accessed: 2022-12-18.

Sienkiewicz, J., Service, N. N. W., Center, O. P., Cuff, T. J., Service, N. N. W., of Observations, O., Chair, W. S. C.-M. M., Services, O., and (JCB), W.-I. J. C. B. (2020). *Extreme Maritime Weather: Improving Safety of Life at Sea*. https://public.wmo.int/en/resources/bulletin/Products_and_services/Extereme_maritime_weather. Accessed: 2022-12-07.

Signal Ocean Group (2022). *The Signal Ocean Platform*. https://www.thesignalgroup.com/signal-ocean-platform/apis. Accessed: 2022-11-16.

Singh, S. and Haider, M. T. U. (2022). Pre-processing of datasets with best feature selection

and outlier removal techniques for a fair and robust model of software defect prediction, note = doi: https://doi.org/10.21203/rs.3.rs-1624790/v1. pages 520–525.

Softwaresim (2022). *Types of simulation models – choosing the right approach for a simulation project.* https://softwaresim.com/blog/types-of-simulation-models-choosing-the-right-approach-for-your-simulation-project/?fbclid=IwAR1gJjdY7ro4uFbccR7uG6z5k3T982b0KhFI5UzPHHig1Jlv3DxNnSV5zG4. Accessed: 2022-11-04.

Stratiotis, E. (2018). *Fuel Costs in Ocean Shipping.* https://www.morethanshipping.com/fuel-costs-ocean-shipping/. Accessed: 2022-12-15.

Szelangiewicz, T. and Żelazny, K. (2016). Ship service speeds and sea margins. *Scientific Journals Zeszyty Naukowe of the Maritime University of Szczecin*, 120(48):43–50.

Taskar, B. and Andersen, P. (2020). Benefit of speed reduction for ships in different weather conditions. *Transportation Research Part D: Transport and Environment*, 85:102337.

Troyanskaya, O., Cantor, M., Sherlock, G., Brown, P., Hastie, T., Tibshirani, R., Botstein, D., and Altman, R. B. (2001). Missing value estimation methods for DNA microarrays . *Bioinformatics*, 17(6):520–525. doi : 10.1093/bioinformatics/17.6.520.

Veneti, A., Makrygiorgos, A., Konstantopoulos, C., Pantziou, G., and Vetsikas, I. A. (2017). Minimizing the fuel consumption and the risk in maritime transportation: A bi-objective weather routing approach. *Computers Operations Research*, 88:220–236. doi: 10.1016/j.cor.2017.07.010.

Zehnder, J. A. (2022). *Location and patterns of tropical cyclones.* https://www.britannica.com/science/tropical-cyclone/Tracking-and-forecasting. Accessed: 2022-11-26.

Zhang, Z. and Li, X. (2017). Global ship accidents and ocean swell-related sea states. *Natural Hazards and Earth System Sciences*, 17:2041–2051. doi: 10.5194/nhess-17-2041-2017.

Zis, T. P., Psaraftis, H. N., and Ding, L. (2020). Ship weather routing: A taxonomy and survey. *Ocean Engineering*, 213:107697. doi: https://doi.org/10.1016/j.oceaneng.2020.107697.

Zurheide, S. and Fischer, K. (2014). Revenue management methods for the liner shipping industry. *Flexible Services and Manufacturing Journal*, 27. doi: 10.1007/s10696-014-9192-0.

Appendices

A Numbers for TCE Calculation Input

Table A.1: Key information about the routes

From port	To port	Laden/ballast	Fuel type	Distance (in NM)[5]	Days (12.5 knots)
Good Hope	Houston (out of ECA)	Ballast	HSFO	7312	24.37
Good Hope	Houston (in of ECA)	Ballast	ULSFO	194	0.65
Houston	Rotterdam (in USA ECA)	Laden	ULSFO	194	0.65
Houston	Rotterdam (out USA ECA)	Laden	HSFO	4384	14.61
Houston	Rotterdam (in Europe ECA)	Laden	ULSFO	536	1.79
Good Hope	Samarinda	Ballast	HSFO	5691	18.97
Samarinda	Pipavav	Laden	HSFO	3694	12.31
Good Hope	Richards Bay	Ballast	HSFO	851	2.84
Richards Bay	Mundra	Laden	HSFO	3808	12.69

Table A.2: Information about port costs

Port	Activity	Port costs in $ [6]
Houston	Loading	93 471
Rotterdam	Discharging	61 807
Samarinda	Loading	13 309
Pipavav	Discharging	56 289
Richards Bay	Loading	23 508
Mundra	Discharging	66 658

[5]Distances retrieved from Dataloy (2022)

[6]Overview of port costs obtained from Signal Ocean Group (2022)

B Descriptive Statistics

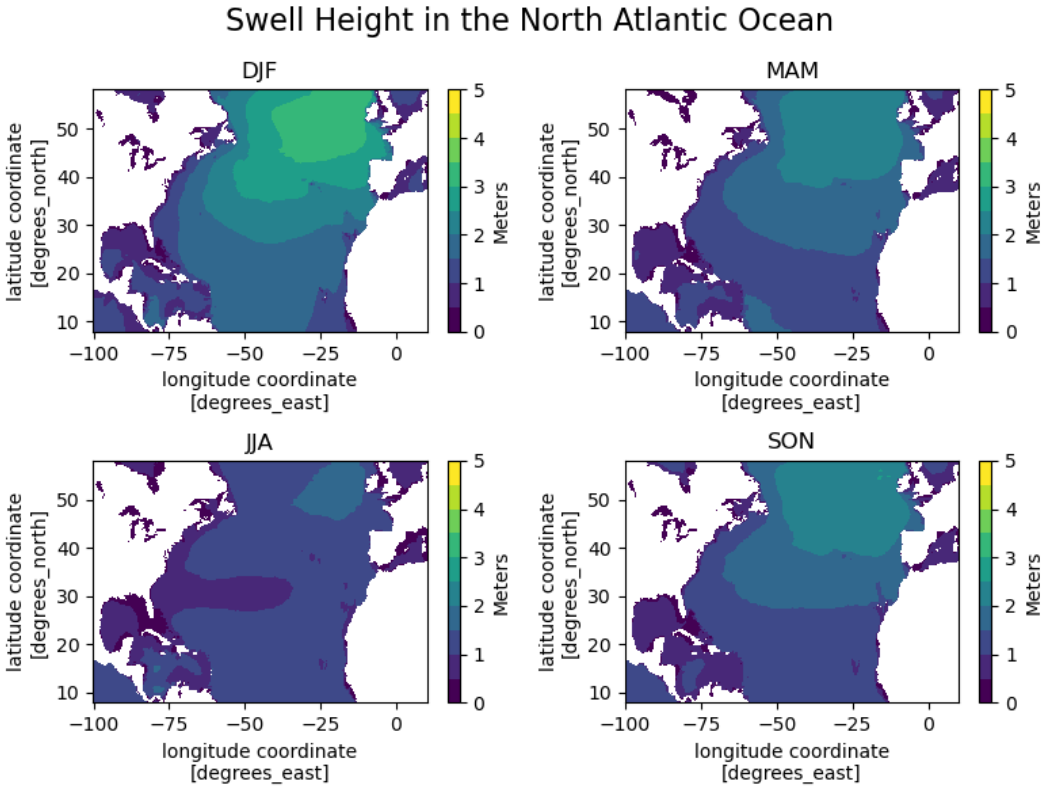

Figure B.1: Mean swell height in the North Atlantic Ocean

Table B.1: Summary statistics of the North Atlantic Ocean - Swell height

Period	Mean	Standard Deviation	Max	Min	95% Quantile
DJF	1.91	1.18	13.73	0.00	4.24
MAM	1.52	0.89	10.65	0.00	3.25
JJA	1.10	0.54	11.61	0.00	2.03
SON	1.48	0.91	11.75	0.00	3.28

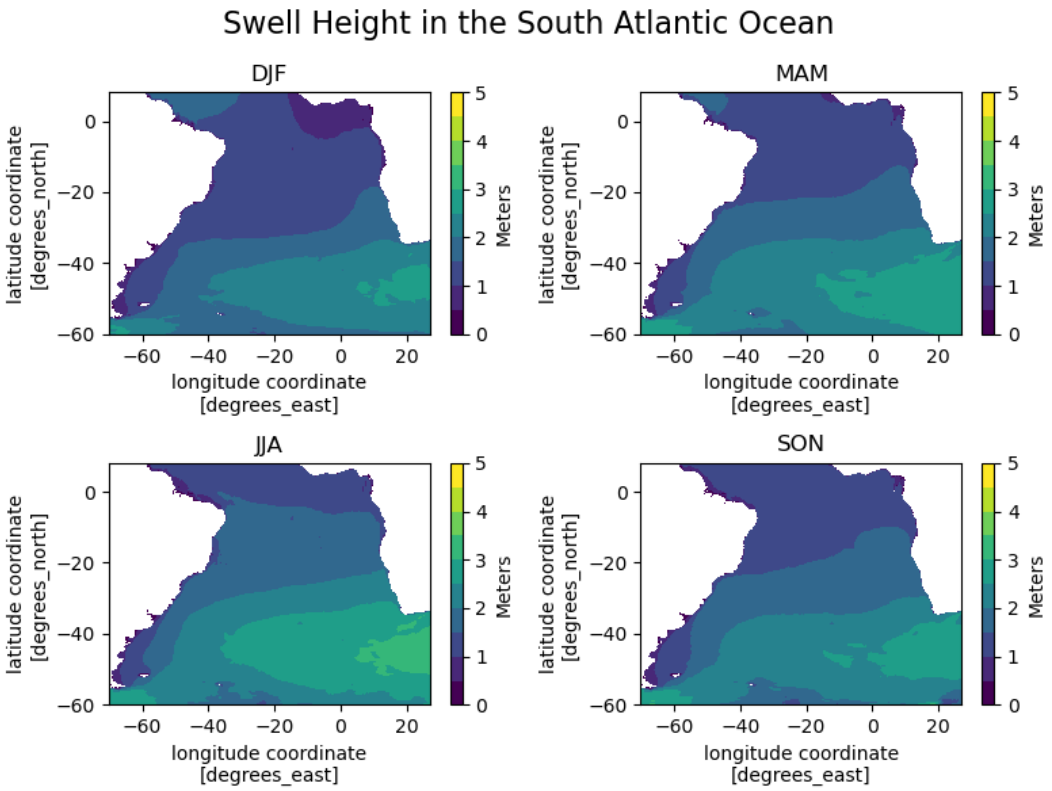

Figure B.2: Mean swell height in the South Atlantic Ocean

Table B.2: Summary statistics of the South Atlantic Ocean - Swell height

Period	Mean	Standard Deviation	Max	Min	95% Quantile
DJF	1.63	0.85	10.96	0.00	3.31
MAM	1.85	0.95	11.47	0.00	3.73
JJA	2.06	1.05	11.74	0.00	4.15
SON	1.83	0.92	11.83	0.00	3.66

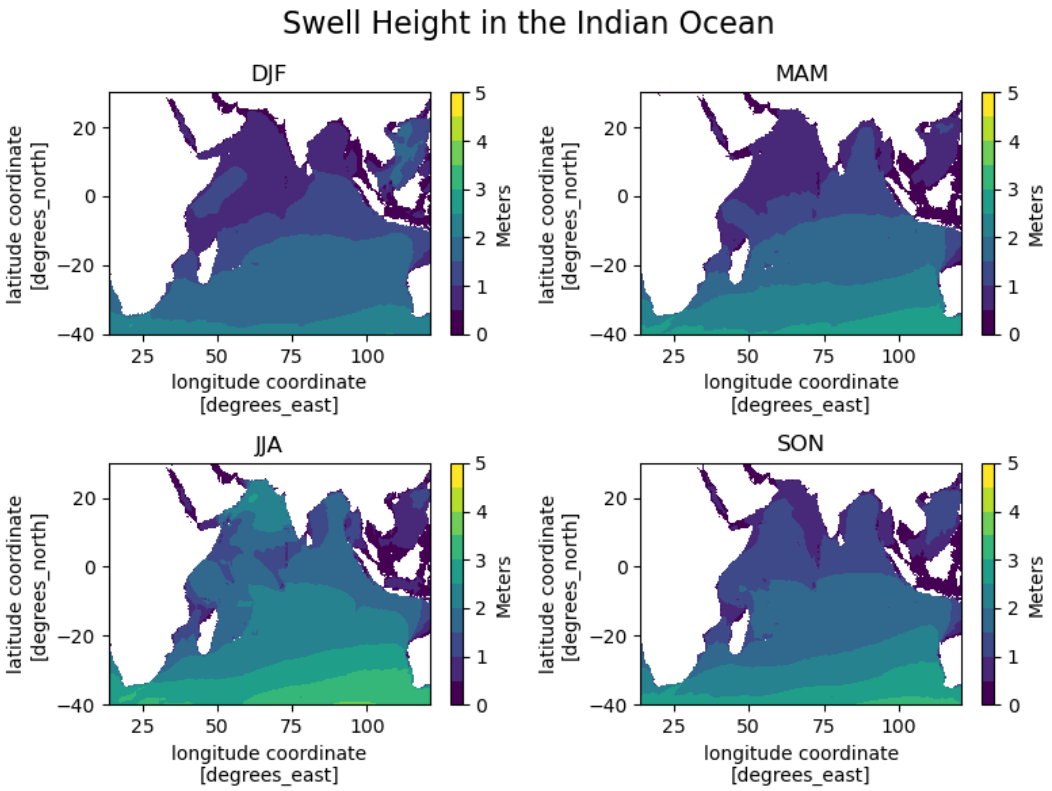

Figure B.3: Mean swell height in the Indian Ocean

Table B.3: Summary statistics of the Indian Ocean - Swell height

Period	Mean	Standard Deviation	Max	Min	95% Quantile
DJF	1.36	0.74	10.70	0.00	2.73
MAM	1.53	0.93	10.67	0.00	3.27
JJA	1.96	1.06	11.83	0.00	3.96
SON	1.54	0.88	9.61	0.00	3.22

C Fuel Consumption

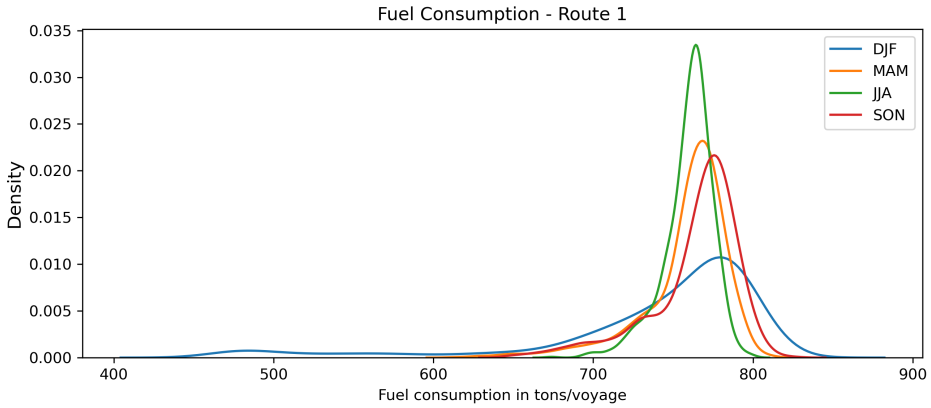

Figure C.1: Total voyage fuel consumption distributions for all periods in Route 1

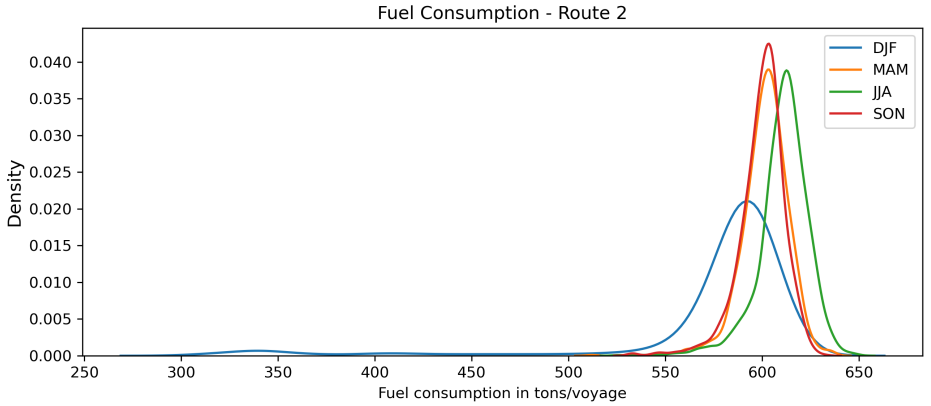

Figure C.2: Total voyage fuel consumption distributions for all periods in Route 2

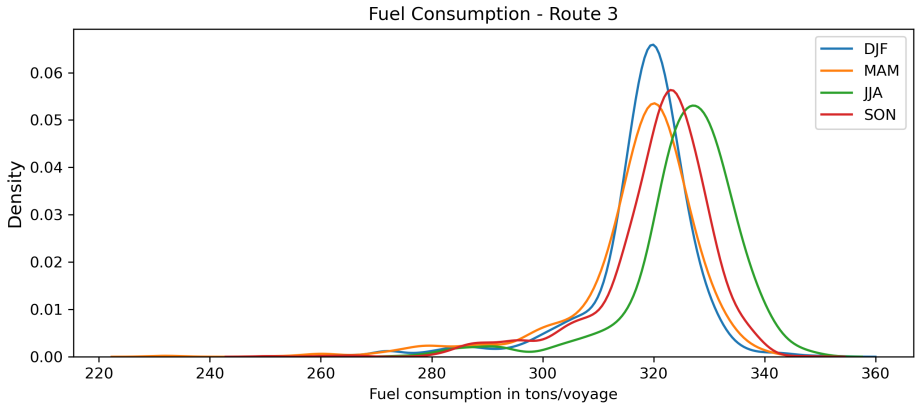

Figure C.3: Total voyage fuel consumption distributions for all periods in Route 3

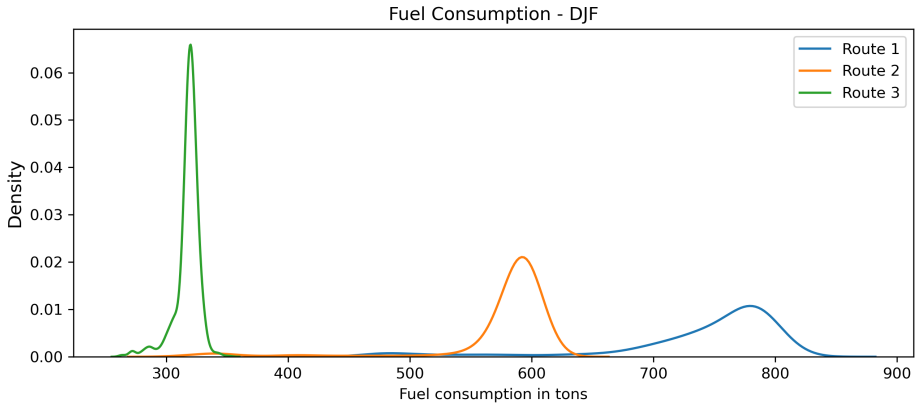

Figure C.4: Total voyage fuel consumption distributions for each route in period DJF

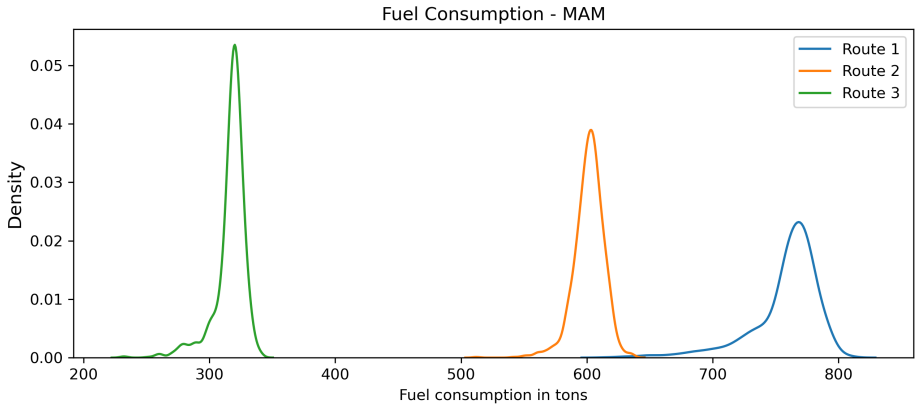

Figure C.5: Total voyage fuel consumption distributions for each route in period MAM

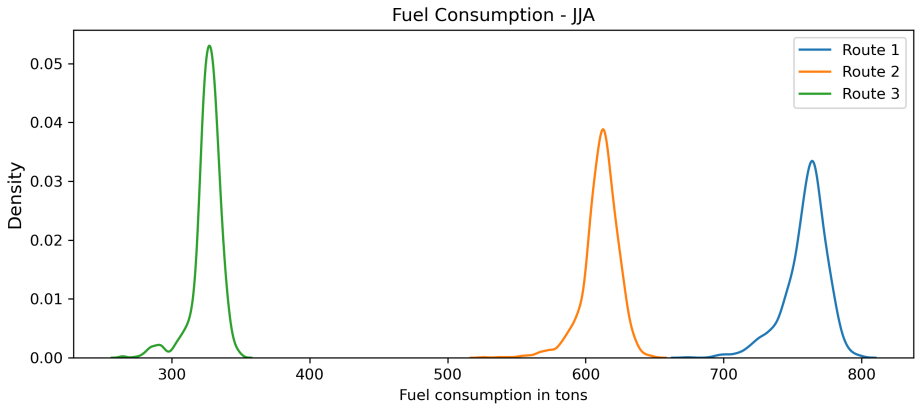

Figure C.6: Total voyage fuel consumption distributions for each route in period JJA

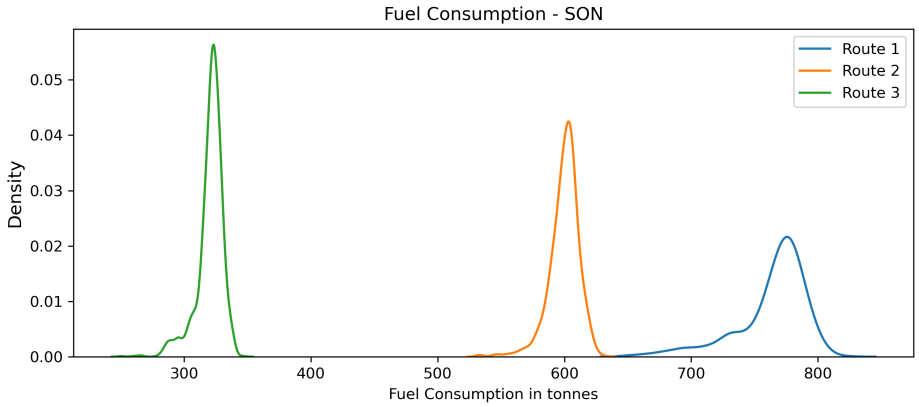

Figure C.7: Total voyage fuel consumption distributions for each route in period SON

D Time Charter Equivalent

Table D.1: Summary statistics of TCE values for scenario 1 for each period

Period	Route	Mean	Standard Deviation	Min	Max
DJF	Route 1	9698.56	241.48	9188.69	10786.50
DJF	Route 2	4575.69	556.05	4126.80	7463.43
DJF	Route 3	19929.50	187.41	19257.80	21005.60
MAM	Route 1	9745.52	220.31	9320.68	10984.60
MAM	Route 2	4315.06	122.75	3931.97	4853.84
MAM	Route 3	19951.30	236.40	19491.00	21613.30
JJA	Route 1	9735.91	125.62	9435.40	10316.70
JJA	Route 2	4214.22	144.97	3808.36	5126.55
JJA	Route 3	19780.20	205.23	19313.7	20978.40
SON	Route 1	9698.56	241.48	9188.69	10786.50
SON	Route 2	4328.47	125.54	4036.09	5062.01
SON	Route 3	19887.40	200.43	19368.00	21053.80

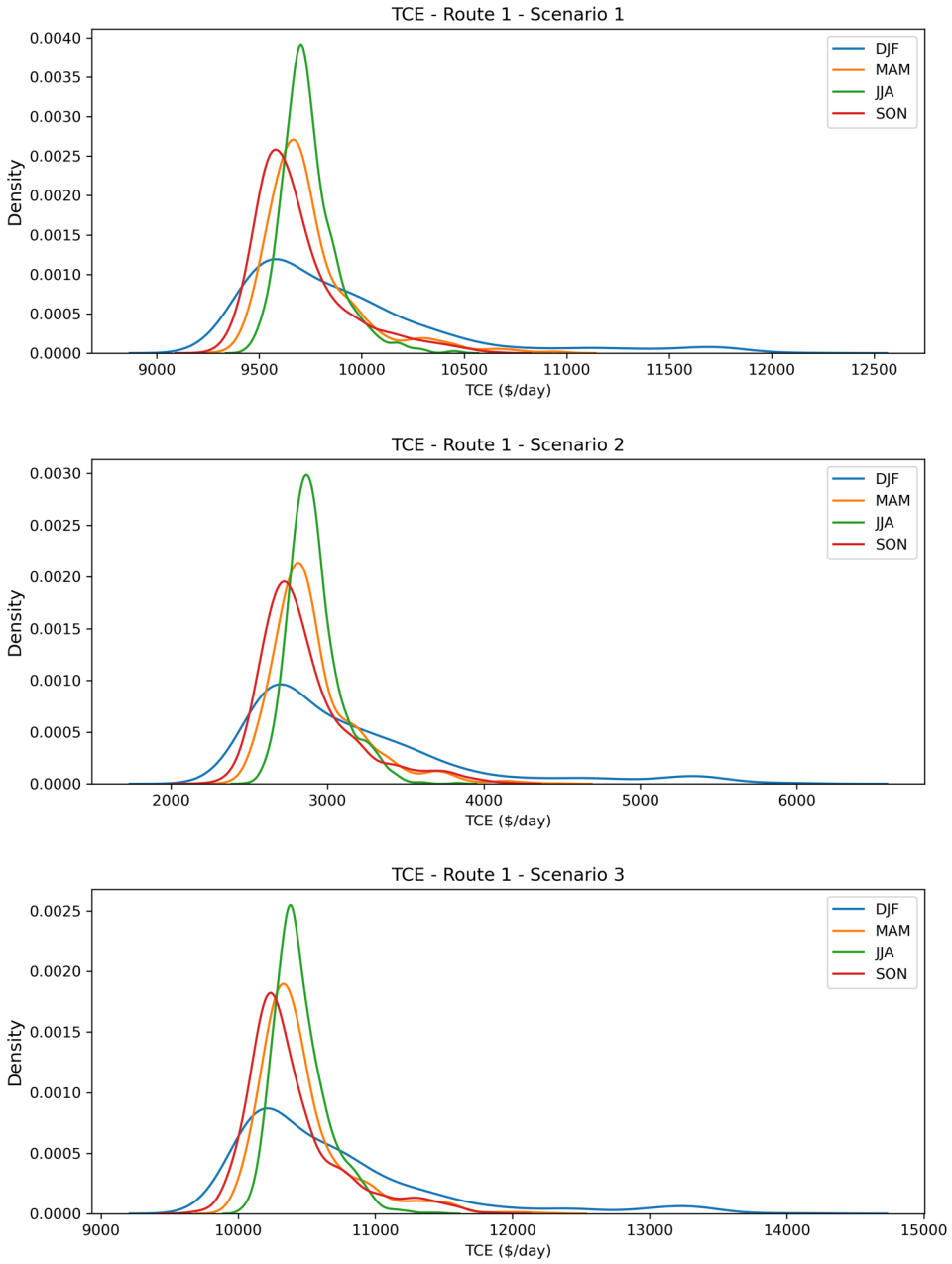

Figure D.1: Time Charter Equivalent distributions for route 1, comparing the four periods for all three scenarios

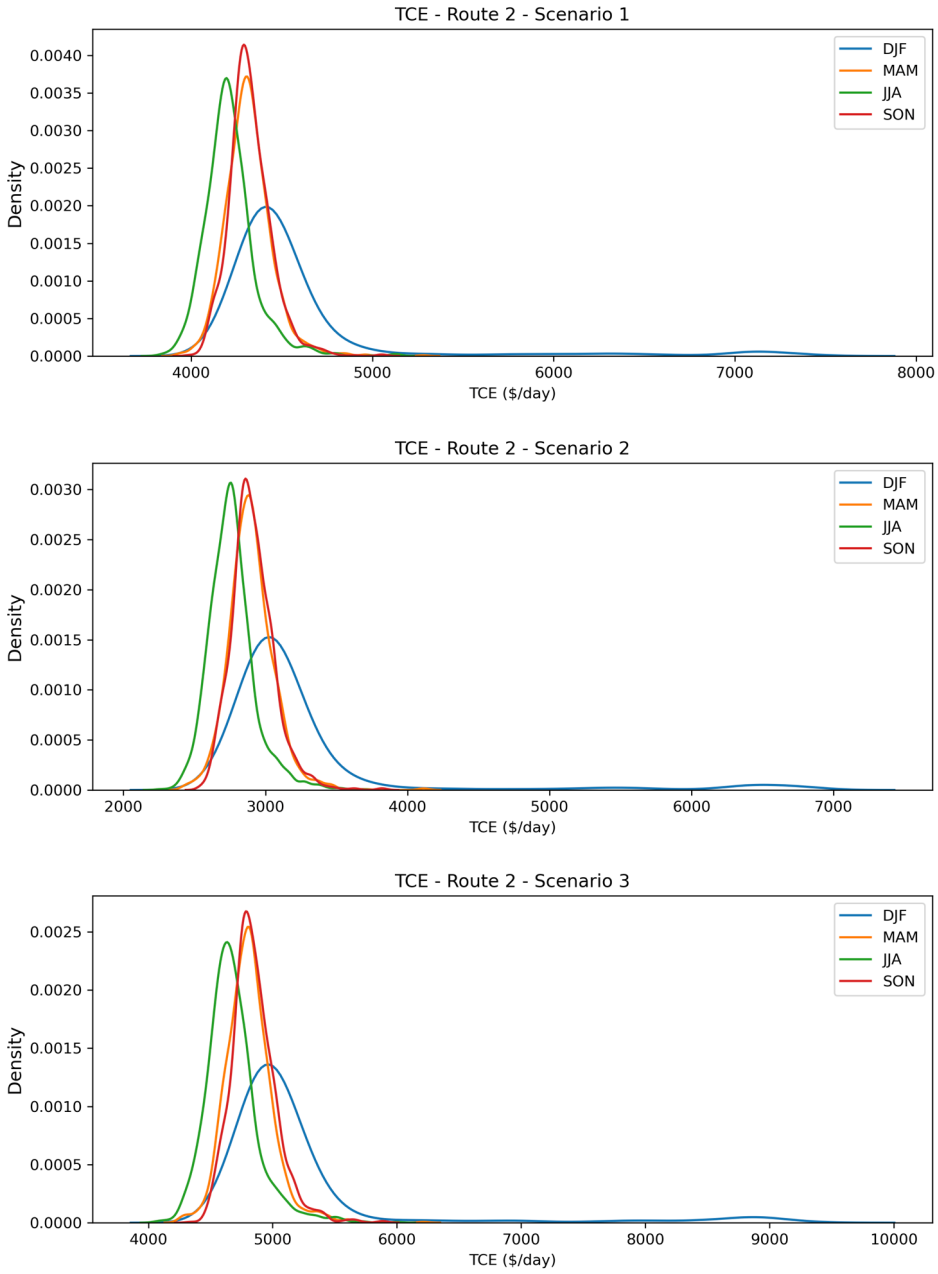

Figure D.2: Time Charter Equivalent distributions for route 2, comparing the four periods for all three scenarios

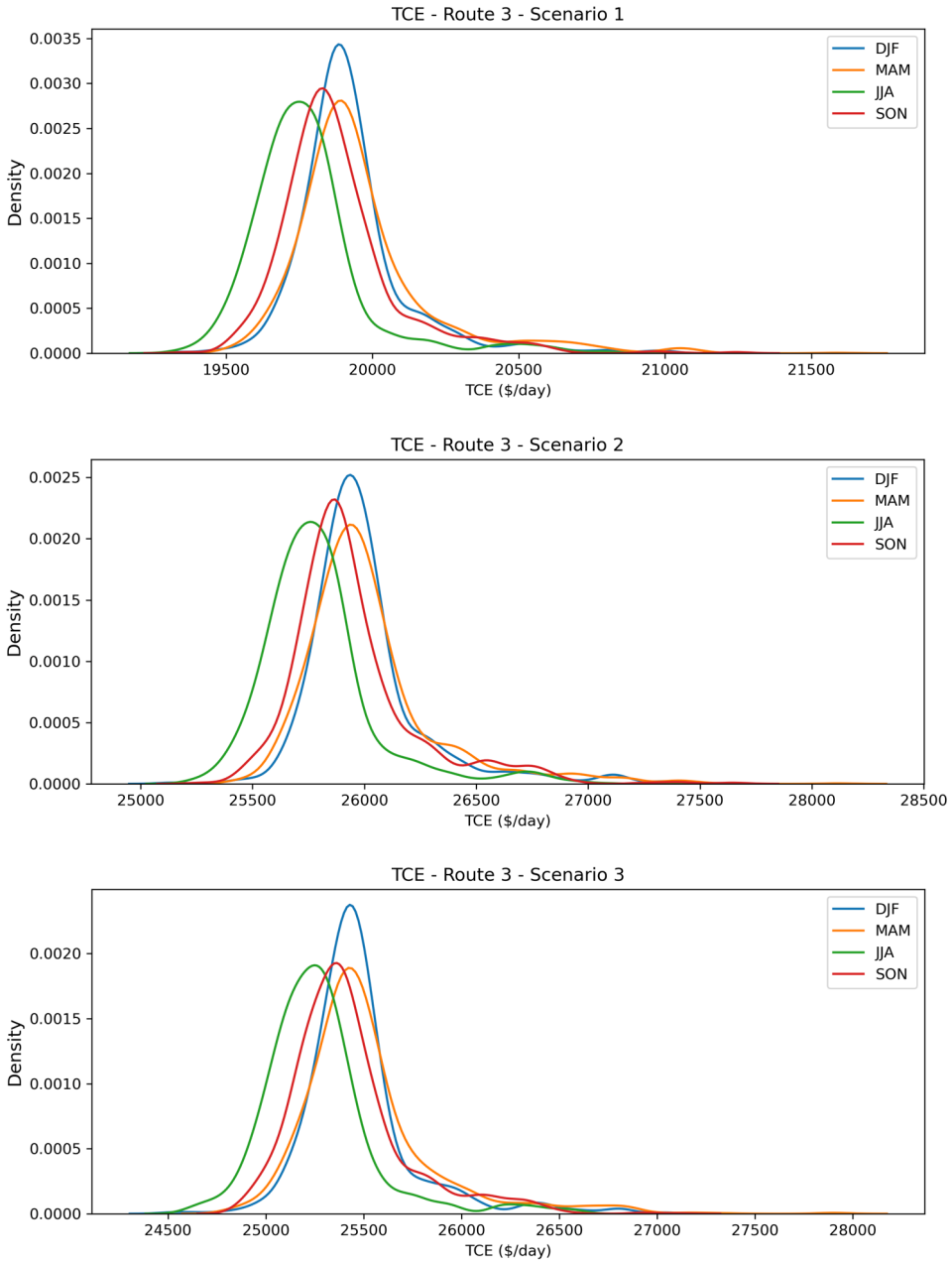

Figure D.3: Time Charter Equivalent distributions for route 3, comparing the four periods for all three scenarios, based on the input value 50,000 tons cargo weight

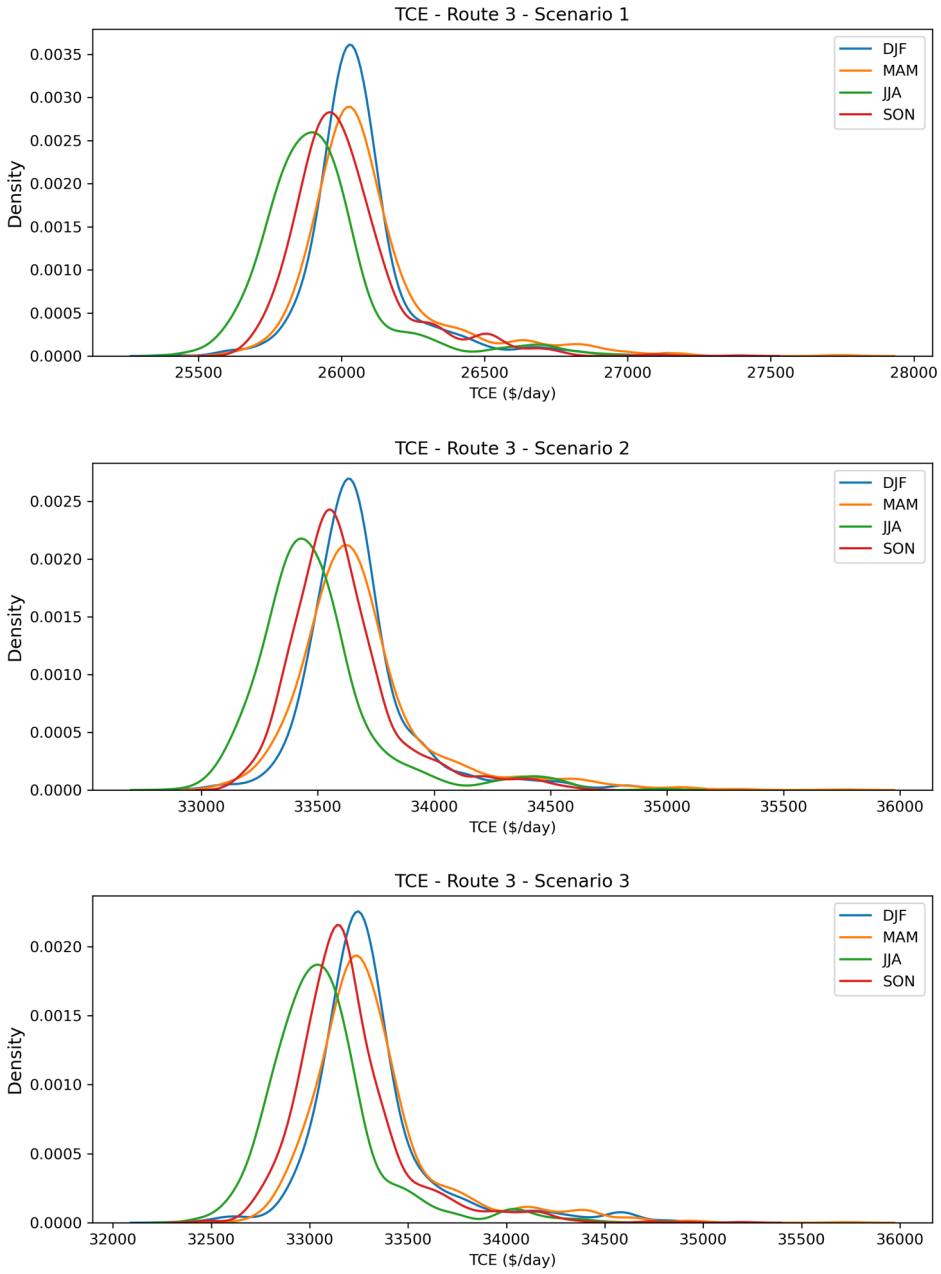

Figure D.4: Time Charter Equivalent distributions for route 3, comparing the four periods for all three scenarios, based on the input value 60,000 tons cargo weight

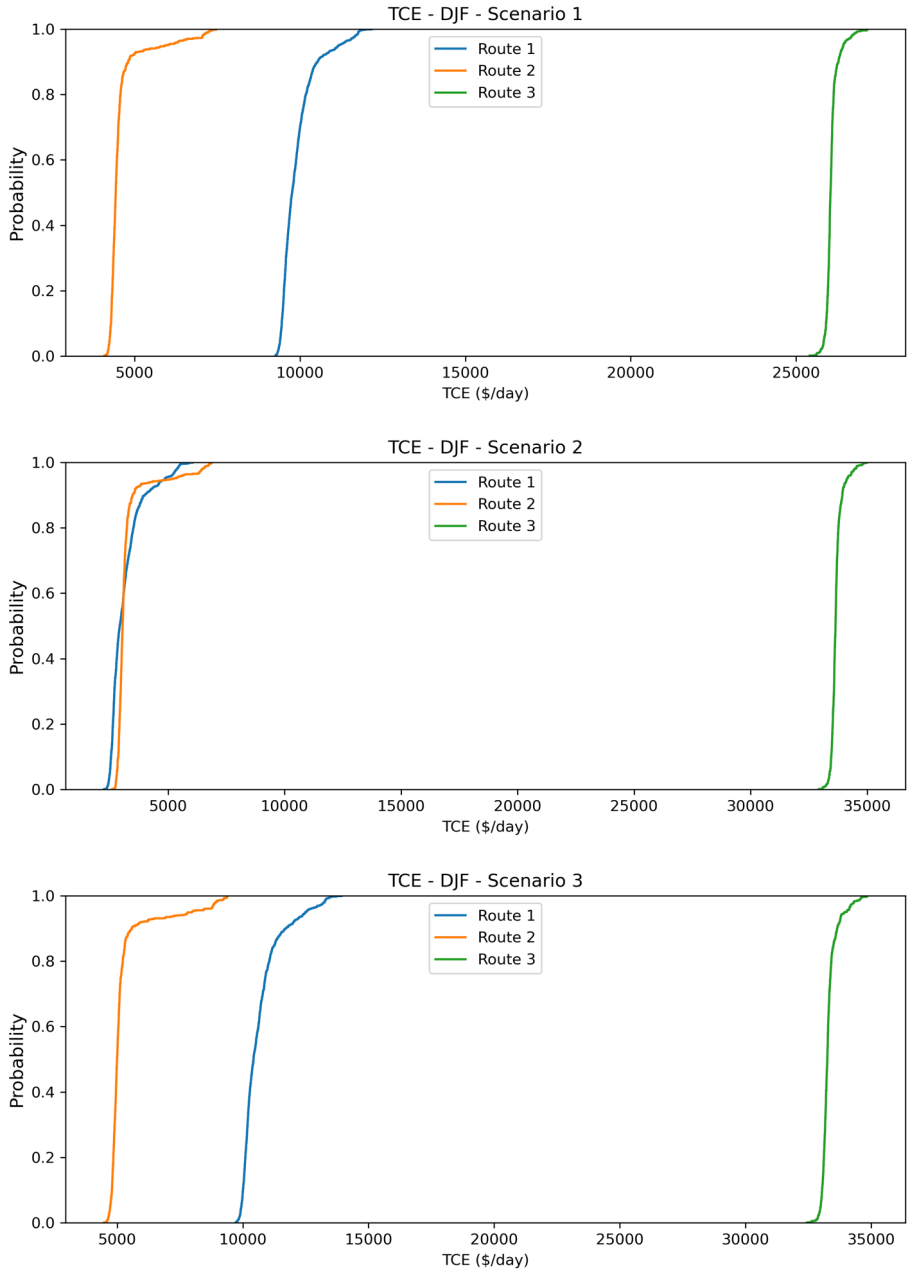

Figure D.5: Cumulative Time Charter Equivalent distributions for the months December, January, and February, for all three scenarios, compared based on the input value 60,000 tons cargo weight for route 3

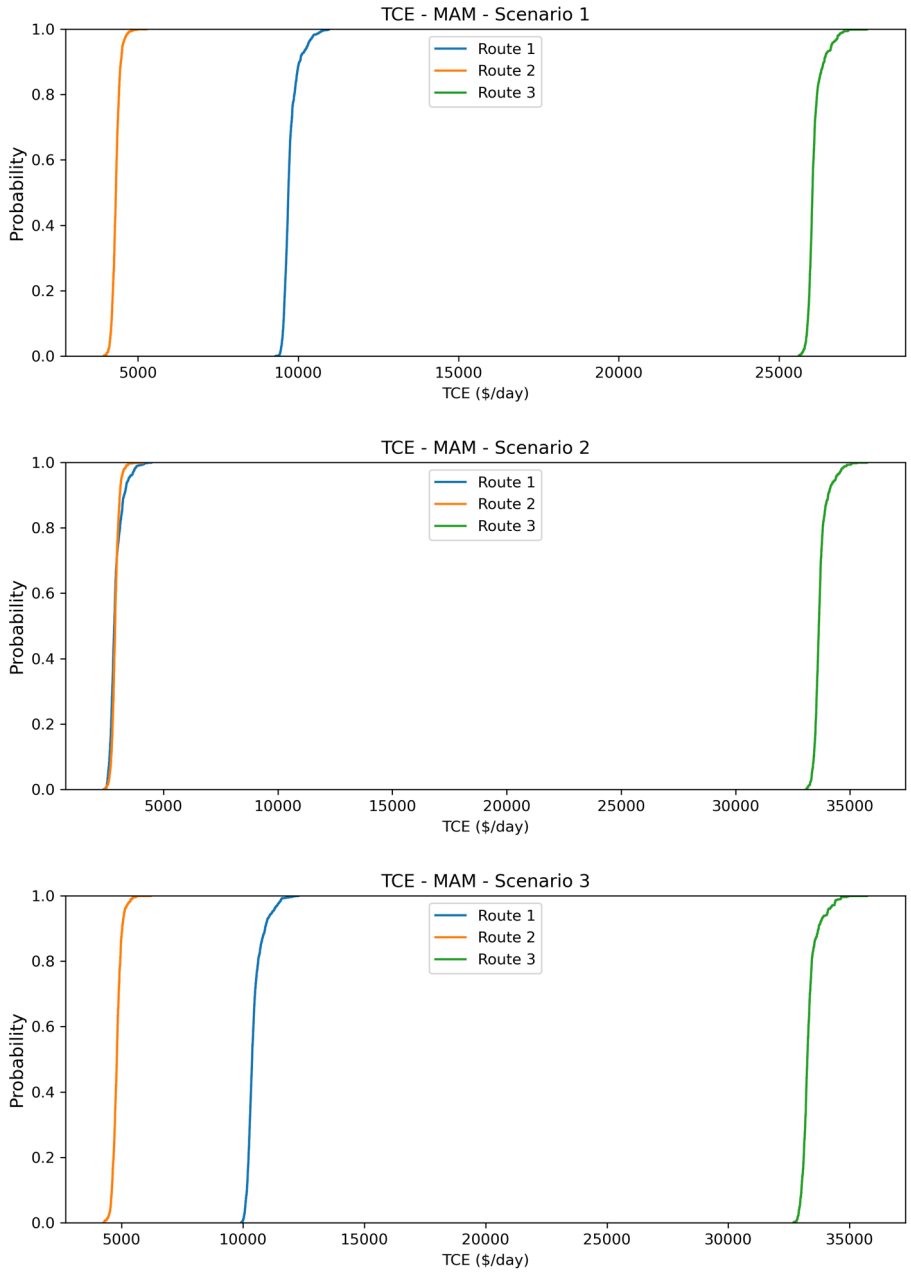

Figure D.6: Cumulative Time Charter Equivalent distributions for the months March, April, and May, for all three scenarios, compared based on the input value 60,000 tons cargo weight for route 3

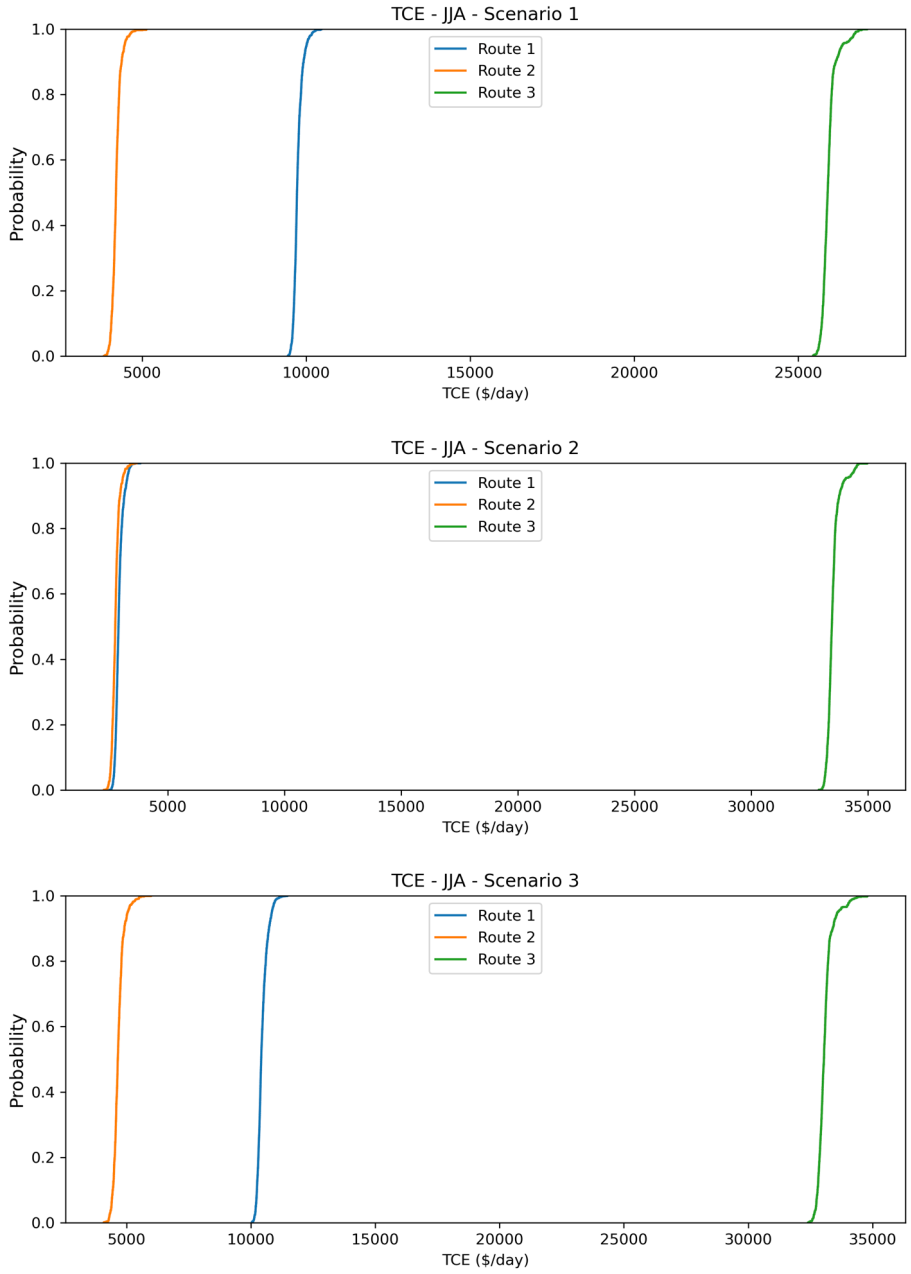

Figure D.7: Cumulative Time Charter Equivalent distributions for the months June, July, and August, for all three scenarios, compared based on the input value 60,000 tons cargo weight for route 3

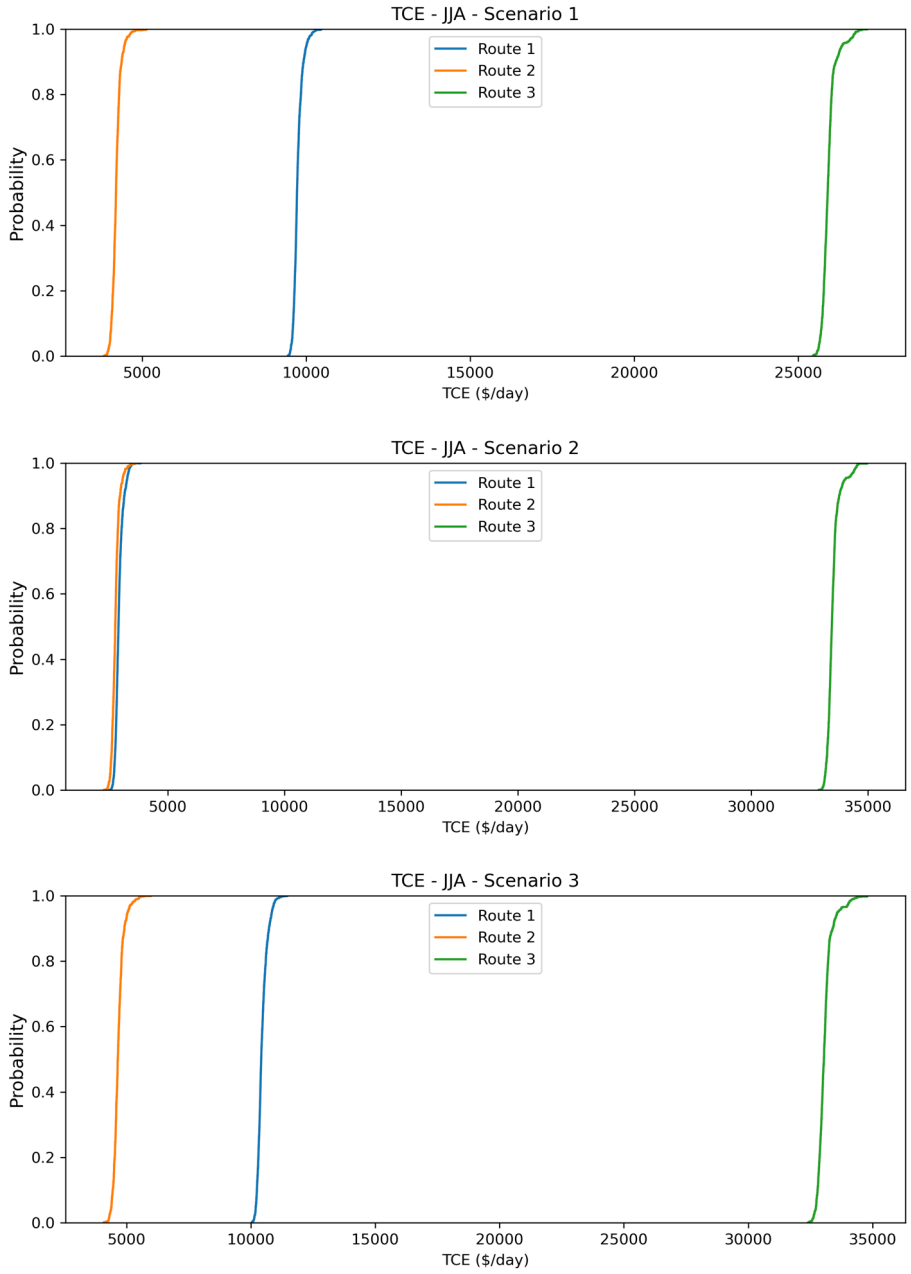

Figure D.8: Cumulative Time Charter Equivalent distributions for the months September, October, and November, for all three scenarios, compared based on the input value 60,000 tons cargo weight for route 3